TÉCNICO LISBOA

Simplified AltBOC Receiver Performance Analysis

Rui Filipe Duarte Nunes

Thesis to obtain the Master of Science Degree in

Aerospace Engineering

Supervisor(s): Prof. António José Castelo Branco Rodrigues
Eng. Tiago Roque Peres

Examination Committee

Chairperson: Prof. João Manuel Lage de Miranda Lemos
Supervisor: Eng. Tiago Roque Peres
Member of the Committee: Prof. José Eduardo C. R. da Cunha Sanguino

May 2016

Acknowledgments

This thesis would not be possible without the constant effort and incentive of helpful people all around me. Being with scientific knowledge, moral support or general advice, this road was thrilled not only by an individual but by many supportive helping hands.

I want to give a special thanks to my DEIMOS supervisor Tiago Peres whose knowledge on the matter and availability were always a positive force and to my IST supervisor António Rodrigues for all the cooperative work.

I also want to express my gratitude to DEIMOS personal staff for their companionship, especially to João Silva and Pedro Freire who always showed interest and made all of this possible.

These working months were hard at times but my family were an invaluable support throughout all the way. Specifically my father whose scientific knowledge and life experience were always positive inputs and helped me push forward at all times, my mother who could always have a kind word to boost the morale and my sister who inspired me to be more and better.

Finally I need to thank all my university and out of school friends, specially my girlfriend who I knew I could always count on.

Resumo

O sinal E5 AltBOC é um sinal de transmissão de informação complexo e exótico usado nos satélites Galileo que permite obter um valor preciso da posição do recetor. Sendo um sinal relativamente novo, há muito terreno inexplorado em relação a este assunto, nomeadamente a arquitetura do recetor que melhor se enquadra neste problema.

Este trabalho tem como objetivo implementar um recetor de E5 AltBOC capaz de desmodular informação de ambas as bandas E5a e E5b em conjunto (Dual Sideband ou DSB) ou em separado (Single Sideband ou SSB) e comparar os seus resultados.

Este trabalho concentra a sua pesquisa nos blocos de seguimento onde a frequência de Doppler e o atraso de código devem ser alinhados entre um sinal gerado localmente e o sinal recebido para funcionar corretamente.

A parte inovadora desta tese é a implementação de um recetor Dual Sideband que usa correladores complexos na sua arquitetura que conseguem processar simultaneamente a informação de ambos os canais de dados e piloto de ambas as bandas E5a e E5b. No capítulo dos resultados deste documento são apresentados os resultados comparativos entre DSB e SSB para várias condições incluindo a variação da relação potência da portadora-ruído.

Palavras-chave: Galileo, Sinal E5, Modulação AltBOC, Receptor, Seguimento

Abstract

The E5 AltBOC signal is a complex and exotic transmission signal used in Galileo satellites to enable the computation of a precise value for the receiver position. Since this signal is relatively new, there is a lot of unexplored terrain regarding this subject namely the receiver architecture that best suits the problem. This work addresses implementation aspects of an E5 AltBOC receiver ready to demodulate data from both bands E5a and E5b together as Dual Sideband (DSB) or separately as Single Sideband (SSB) and compare its results.

This work focus its research on the tracking block where a Doppler frequency and code delay must be aligned between the locally generated replica and the received signal to operate properly.

The innovating part of this thesis is the implementation of a Dual Sideband receiver that uses complex correlators in its architecture that can process simultaneously the information of both E5a and E5b data and pilot channels. In the results chapter of this document, we present the comparative results between DSB and SSB for various conditions including the variation of the carrier power to noise ratio.

Keywords: Galileo, E5 Signal, AltBOC modulation, Receiver, Tracking

Contents

List of Tables

List of Figures

Glossary

ACF Autocorrelation Function.

AGC Automatic Gain Control.

AltBOC Alternate Binary Offset Carrier.

AWGN Additive White Gaussian Noise.

BOC Binary Offset Carrier.

BPSK Binary Phase Shift Keying.

C/A Coarse Acquisition.

C/N$_0$ Carrier Power to Noise Power Spectral Density.

C$_I$/N$_0$ Interference Power to Noise Spectral Density.

CAF Cross-Ambiguity Function.

CASM Coherent Adaptive Sub-Carrier Modulation.

CBOC Composite Binary Offset Carrier.

CDMA Code Division Multiple Access.

CELP Coherent Early-Late Power.

CS Commercial Service.

DLL Delay Locked Loop.

DSB Double Side Band.

E Early.

EGNOS European Geostationary Navigation Overlay System.

EKF Extended Kalman Filter.

F/NAV Freely accessible Navigation Message.

FDMA Frequency Division Multiple Access.

FEC Forward Error Correction.

FFT Fast Fourier Transform.

FIC Full-Band Independent Correlation.

FLL Frequency Locked Loop.

GDOP Geometric Dilution of Precision.

GLONASS Globalnaya Navigatsionnaya Sputnikovaya System.

GNSS Global Navigation Satellite System.

GPS Global Navigation System.

I In Phase.

I/NAV Integrity Navigation Message.

ICD Interface Control Document.

IF Intermediate Frequency.

L Late.

LFSR Linear Feedback Shift Register.

LO Local Oscillator.

LOC Linear Offset Carrier.

LOS Line of Sight.

LS Least Squares.

MBOC Multiplexed Binary Offset Carrier.

NELP Non Coherent Early-Late Power.

OCXO Ovenized Compensated Crystal Oscillator.

OMUX Output Multiplexer.

OS Open Service.

P Prompt, Position.

PLL Phase Locked Loop.

PRN Pseudo Random Noise.

PRS Public Regulated Service.

PSD Power Spectral Density.

PV Position, Velocity.

PVA Position, Velocity and Acceleration.

Q Quadrature.

RFI Radio Frequency Interference.

RHCP Right Hand Circularly Polarized.

RMSE Root Mean Square Error.

RTK Real Time Kinematic.

SBT Side Band Translation.

SIS Signal in Space.

SNR Signal to Noise Ratio.

SoL Safety of Life.

SSC Spectral Separation Coefficient.

TCXO Temperature Compensated Crystal Oscillator.

TMBOC Time Multiplexed Binary Offset Carrier.

UERE User Equivalent Range Error.

WLS Weighted Least Squares.

Chapter 1

Introduction

This chapter is a brief introduction to the work made in scope of by this thesis. Section 1 presents the overall state-of-the-art on the subject. In section 2 we state the main objectives of this thesis. Section 3 summarizes the contents presented in the following chapters.

1.1 State-of-the-art

Galileo is the European Global Navigation Satellite System (GNSS) and provides a highly accurate, guaranteed global positioning service under civilian control [1]. The European GNSS approach began with the European Geostationary Navigation Overlay (EGNOS), which provides civil complements to GPS since mid-2005 in its initial operation. From the very beginning, EGNOS was meant to be the bridge to Europe's own full-fledged GNSS.

Galileo uses 3 different bands; band E5 is the one with the lowest central frequency ($f_c = 1191.795$ MHz) but exhibits the widest bandwidth. The modulation assigned to this band, the AltBOC(15,10), is a complex signal composed of 4 codes multiplexed so as to have a constant envelope. This is the most sophisticated and promising signal that is transmitted by the Galileo system. The main lobes of the signal spans over 50 MHz which makes the AltBOC bandwidth the largest of all GNSS signals. As a consequence, the receiver desiring to receive the complete signal shall have a bandwidth about thirty times larger than the current basic GPS receiver. AltBOC was at first imagined to fulfil a need: be able to generate and multiplex 2 or 4 navigation signal components (each with its own PRN code) or two close frequency bands taking into account the limitations of the onboard output multiplexer (OMUX), and giving it a constant envelope in order to maximize the amplifier efficiency. Processing the whole signal rather than the 2 separate E5a and E5b signals wasn't envisioned at first. The idea of receiving the complete AltBOC arrived later when it was understood that processing this wideband signal would lead to unprecedented tracking accuracy not only in Gaussian channels but also in the presence of multipath. This advantage was later confirmed by measurements performed on the real signal broadcasted by GIOVE-A [2].

For the single carrier approach with baseband multiplexing of 4 different signals in E5-band, candi-

date modulation schemes are Complex-LOC(15,10), Complex-BOC(15,10) and the constant envelope method of AltBOC(15,10) which are explained and compared in [3]. In order to analyze DSB and SSB tracking accuracy of such signals the concept of complex baseband receiver model with a non-coherent DLL is considered therein.

Some of the first architectures proposed to track AltBOC signals were described in the patents [4] and [5]. In general, the receiver designer can choose among 4 options for processing the E5 signal, or any AltBOC signal (for instance, in Beidou systems): (i) process the entire E5 signal as a wideband 8-phase signal; (ii) process both E5a and E5b, but separately; (iii) process only the E5a component, and (iv) process only the E5b signal.

In [6], several aspects of the AltBOC receiver were discussed and it was shown that, due to the large bandwidth of the signals, some problems, namely signal distortion, might appear in the presence of strong ionospheric electron density. The limitations imposed by the ionosphere on the processing of wideband signals were addressed in more depth in [7].

The analysis of the possible architectures allowed by the AltBOC signals is carried out in [8] with a new architecture being proposed and discussed (see also [9]). This effort was further developed in [10] where the candidate discusses new acquisition, tracking and multipath mitigation algorithms.

More recent research analyzes the potential of the combination of Galileo E1 CBOC and E5 AltBOC pseudoranges for surveying and mapping applications. The tracking precision of the E1 and E5 pseudoranges under “open sky” and strong “tree coverage” scenarios result in 0.25 to 2.0 m (E1) and 0.02 to 0.08 m (E5) pseudorange precisions. These values permit the pseudorange solutions to compete with carrier phase solutions for certain types of applications that require precisions around 10 cm. The main advantages of pseudorange positioning are the simplicity and robustness of data processing [11]. One of the promising applications of AltBOC signals is in precise automobile navigation; however, this application will be viable only after a sufficient number of Galileo satellites are deployed, which is expected to happen in the next four-six years [12].

1.2 Objectives

Due to the complexity of the AltBOC signal and its very large bandwidth, the design and implementation of receivers for the Galileo E5 band is a challenging task. The receiving structures depart from the typical solutions adopted in other less sophisticated modulation schemes.

The objectives of this work are multiple: (i) to gain insight into the modulation itself and the different receiving architectures it permits, (ii) to determine analytic expressions that allow developing those architectures, (iii) to implement AltBOC receivers using the Dual Sideband (DSB) and the Single Sideband (SSB) signal processing methods and compare their results.

The robustness of the algorithms under study will be tested by varying the value of the carrier to noise ratio (C/N_0) for different combinations of parameters, such as code discriminator Early(E)-Late(L) spacing, Phase Locked Loop (PLL) and Delay Locked Loop (DLL) noise equivalent bandwidths, etc. The problem of calibrating and optimizing the receiver parameters in order to achieve the best results will be

addressed. Different scenarios which include multipath and narrowband/wideband interference will be also considered.

1.3 Thesis Outline

This document consists of 7 chapters and 4 appendices.
In the first chapter, **Chapter 1 - Introduction**, a brief discussion is made regarding the State-of-the-art of the E5 Galileo receiver context in Section 1, objectives of this work in Section 2 and the thesis contents in Section 3.
The second chapter, **Chapter 2 - GNSS Concept**, presents an introduction to all of the GNSS context. Section 1 presents the basic concept, Section 2 describes summarily the current existing satellite systems, Section 3 presents a brief approach to the GNSS signals, Section 4 briefly explains the existing modulations, Section 5 explains how to solve the navigation equation and finally Section 6 presents the sources of signal perturbation in the transmitter-receiver path.
The third chapter, **Chapter 3 - AltBOC Signal**, lists the characteristics of the Galileo E5 Signal mainly obtained from the official Interface Control Document (ICD) [13]. Section 1 explains the Galileo services and its connection to the E5 signal, Section 2 and Section 3 present the signal equivalent representations, Section 4 introduces the code generation process, Section 5 presents the E5 Signal autocorrelation function and power spectral density and Section 6 displays the expected signal power and signal to noise ratio received at earth surface.
The fourth chapter, **Chapter 4 - GNSS Receivers**, introduces the general receiver concepts and related issues. Section 1 presents general architecture and blocks used in a receiver, Section 2 explains the acquisition process, Section 3 explains the signal tracking concept and process, Section 4 analyzes the DLL and PLL loops performance and Section 5 discusses the problem of signal multipath.
The fifth chapter, **Chapter 5 - Receiver architectures for AltBOC Signals**, continues the addressed topics introduced in chapter 4 but specified for the E5 signal. Section 1 introduces the chapter, Section 2 explains the process behind signal filtering, Section 3 and Section 4 present two distinct architecture theoretical approaches for Single Side Band and Double Side Band processing structures, respectively.
The sixth chapter, **Chapter 6 - Implementation and Results**, describes the simulation and testing phase while reporting the obtained results for the carrier to noise variation performance for several parameters and both DSB and SSB. Section 1 explains the Monte Carlo simulation methods used. Section 2 explains the used parameters and typical obtained results. Section 3 presents the results for different values of carrier to noise ratio (C/N_0), Early-Late spacing and time of integration. Finally Section 4, presents the results obtained by adding a signal interference to the received signal.
The seventh chapter, **Chapter 7 - Final remarks**, ends this document by listing the final remarks in Section 1 and by enumerating possible future work regarding this subject in Section 2.
Appendix A presents the autocorrelation functions of GNSS signals where the E5 signal ACF is present, **Appendix B** presents the series expansion of the AltBOC(15,10) subcarriers used in the AltBOC modulation, **Appendix C** gives a more detailed explanation of the sampling frequency problem and **Appendix**

D shows the theoretical approach to the used second-order PLL loop filter.

Chapter 2

GNSS Concept

This chapter presents the study and work related to the Global Navigation Satellite Systems (hence GNSS). In section 1, a general approach is made towards the concept and objectives GNSS. Section 2 presents the active worldwide GNSS systems. Section 3 introduces the GNSS signal structure and components as well as the modulations used in Section 4. Section 5 presents the resolution of the navigation equation method and section 6 presents the main factors responsible for signal degradation.

2.1 Basic Concept

The idea behind GNSS systems is to find the position of a point relative to the position of well-known reference points. To achieve that, we use mathematical, geometry and physics tools to ensure that the estimated point position has the lowest possible error relative to the real position.
In order to calculate the position value of any device at the surface of the earth, the receiver has to receive signals coming from different reference points (in our case, satellites). Each delayed signal can be transformed into a distance in order to triangulate the point positioning. Figure 2.1 shows the graphic process behind the trilateration of any point (”location”) in reference with moving points (”satellites”). By trilateration we mean the estimation of a position based on measurements of distances [14].

It should be noted that, as we know, neither earth nor the satellites are fixed points since everything is in perpetual movement. Even if we consider the earth surface as a fixed point, the satellites need to move in order to maintain a constant altitude orbit. All the movement in the problem should be considered relative.
Even though this image seems to represent a 2-D problem, one should always imagine a 3-D situation where each satellite radius circle is in fact a sphere. In theory, the interaction between the receiver with one satellite would give an infinite number of possible position solutions, two satellites would result in a circle and three satellites would give one exact point with three coordinates (x,y,z) near the earth surface. However, when we consider a real system, 3 satellites are not enough to calculate the exact position since there is a number of factors that induce error to the computation. In fact, the receiver clock is not synchronized with the satellites clocks and has to be estimated as a fourth coordinate. Therefore,

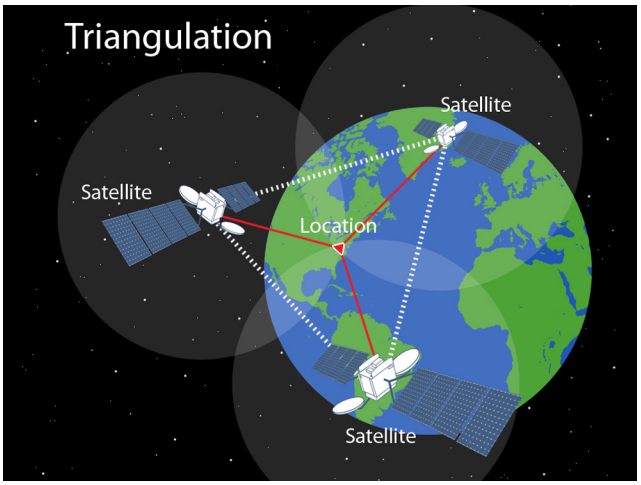

Figure 2.1: GNSS trilateration [15]

a minimum of 4 satellites is required to solve the navigation equation.
Due to all possible errors, the final solution of the navigation equation is affected by an error that lies inside an ellipsoid where somewhere should be the real position of the located point. The size of this ellipsoid of error can be regarded as an accuracy value of the real position since a large ellipsoid implies a large position error associated while a small ellipsoid indicates a reduced set of possible position values.

2.2 Active Navigation Systems

As stated in the previous section, earth orbiting satellites play an important role in the navigation process. As of 2016, there are four major satellite constellation active systems: American GPS, European Galileo, Chinese Beidou and Russian GLONASS. These systems are independent but the receiver can operate with them together to achieve better positioning results.
Usually these systems are formed by three segments:

- Space Segment: consists of the satellite constellation that ensures the transmission of one-way signals towards the earth surface containing information about satellite position and time;
- Control Segment: composed by a network of ground station facilities that control, monitor and analyze data from the active satellites;
- User Segment: involves all signal receiving devices that receive the satellite transmitted data to calculate the user's three dimensional position and time.

GPS

GPS is the American navigation system and the first global system to exist. At first, the system was to be used in military applications only to be fully civilian operational in years after its creation. GPS satellites orbit at an altitude of approximately 20,200 km (Medium Earth Orbit) and 55 degrees inclination [16].

As of 2016 the GPS system has 31 operational satellites (12 legacy and 19 modernized) that transmit signals in three different bands (L1,L2 and L5).

GALILEO

The Galileo is Europe's own global navigation system made specifically for civilian purposes. Galileo initial services will be made available by the end of 2016 and system completion is predicted to 2020 [17].
Galileo satellites orbit at an altitude of approximately 23,222 km (Medium Earth Orbit) and as of December 2015 the constellation is composed by 10 operational satellites and 2 additional in Early Orbit Phase. Galileo satellites will transmit signals in E1, E5 and E6 bands that will be globally accessible to any capable receiving device.
Galileo's ground segment is mainly composed by a Ground Mission Segment (GMS) in Fucino, Italy and a Ground Control Segment (GCS) in Oberpfaffenhofen, Germany as well as globally distributed stations used for diverse signal control and maintenance purposes.

BEIDOU

Beidou is the Chinese global navigation system. According to Beidou online resource [18] the constellation system will be composed by five geostationary orbit satellites and thirty non-geostationary orbit satellites in Medium Earth Orbit with 27878 km of altitude and 55 degrees of inclination. As of July 2015, 14 satellites are operational: 5 in geostationary orbit, 5 in geosynchronous orbits with inclination 55 degrees and 4 in medium earth orbits. The Ground Segment includes one Master Control Station, two Upload Stations and 30 Monitor Stations. Beidou satellites transmit signals in bands E1, E2, E5b and E6 (both in phase and quadrature) which overlap some of the European Galileo's signal bands.

GLONASS

GLONASS (translated from the Russian "Globalnaya navigatsionnaya sputnikovaya sistema" as "GLObal NAvigation Satellite System") is the Russian navigation system. Currently it has 23 operational satellites. The satellites are located in middle circular orbit at 19,100 km altitude with a 64.8 degree inclination and a period of 11 hours and 15 minutes. GLONASS satellites transmit two types of signal: open standard-precision signal L1OF/L2OF, and encrypted high-precision signal L1SF/L2SF.

2.3 GNSS Signals

Each of the GNSS satellites transmits a unique set of signals characterized by the satellite and its navigation system. Figure 2.2 summarizes the signal bands used by each constellation system.

The E5 Galileo signal will be discussed in greater detail in chapter 3 since it is the main subject of this thesis. This section will present a brief introduction to GNSS signals in general.

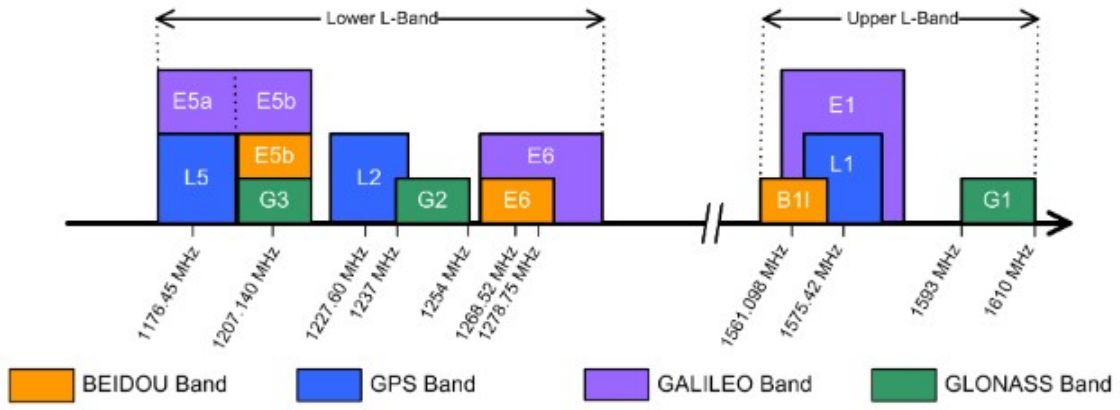

Figure 2.2: GNSS signal bands [19]

In a generic way, GNSS transmitted signals can be represented by

$$\begin{aligned} S_\chi(t) &= \sqrt{2P_{T,\chi}} \cdot \Re[s_\chi(t) \cdot \exp(\jmath\omega_{c,\chi}t)] \\ &= \sqrt{2P_{T,X}}[S_{X_I}(t)\cos(\omega_{c,X}t) - S_{X_Q}(t)\sin(\omega_{c,X}t)] \end{aligned} \tag{2.1}$$

where

$$s_\chi(t) = S_{\chi I}(t) + \jmath S_{\chi Q}(t) \tag{2.2}$$

is the complex baseband signal with unity power

- $P_{T,\chi}$ is the transmitted signal power (W)
- $\omega_{c,\chi}$ represents the carrier frequency (radians/s)
- $\Re$ is the real function operator
- χ is the type of signal

The baseband signals $S_{X_I}(t)$ and $S_{X_Q}(t)$ may combine the following type of signals: (i) spreading code signal $c(t) = \pm 1$ (with chip duration T_C), (ii) navigation data signal (with bit duration $T_B \gg T_C$) and (iii) digital baseband modulation $g(t)$. In some cases signals (i) and (ii) may not be present. The different combinations are sketched in fig. 2.3.

All of these properties are different for the existing signals. We take the Galileo signals for example which use different Binary Offset Carrier (BOC) modulations to modulate the baseband signal and have the carrier frequency indicated in the table 2.1.

This table shows that signals in bands E1 and E6 consist of multiplexing three components: $s_1(t)$, $s_2(t)$ and $s_3(t)$ in order to obtain a complex signal that modulates the inphase and quadrature sinusoidal carriers, according to (2.1). In case these components are binary with $s_1(t) = \pm 1$, $s_2(t) = \pm 1$, $s_3(t) = \pm 1$, the multiplexing schemes (called Coherent Adaptive Sub-Carrier Modulation or CASM) assume the following expression in baseband [1].

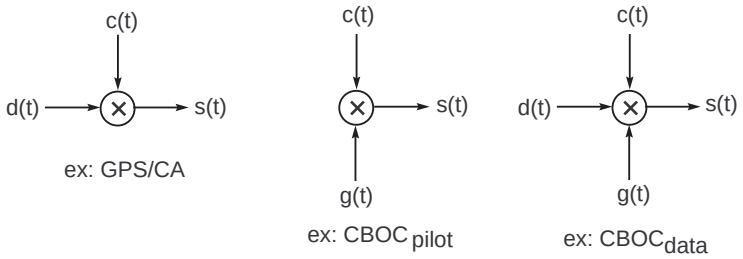

Figure 2.3: Possible combinations of signals $c(t)$ code, $d(t)$ (data) and $g(t)$ baseband modulation in a GNSS baseband signal $s(t)$

Signal	Carrier frequency (MHz)	Receiver Frequency Bandwidth (MHz)	Number of Components
E1	1575.420	24.552	3
E6	1278.750	40.920	3
E5	1191.795	51.150	4
E5a	1176.450	20.460	2
E5b	1207.140	20.460	2

Table 2.1: Carrier frequencies and receiver reference bandwidths for Galileo [13]

$$S_{BB}(t) = s_2(t) + s_3(t) + j(s_1(t) - s_1(t)s_2(t)s_3(t)) \tag{2.3}$$

where the inter-modulation component $s_1(t)s_2(t)s_3(t)$ is added in order to guarantee that the amplitude of the composite signal is kept constant. In fact we have $|S_{BB}(t)|^2 = 4$. The constant amplitude is necessary to operate with high-efficiency Radio Frequency (RF) power amplifiers in the satellites.
The description above is valid for the signals of band E6, but not applicable to band E1 since the components $s_2(t)$ (Data) and $s_3(t)$ (Pilot) are Composite Binary Offset Carrier(CBOC) signals which present 4 levels instead of 2. Thus, a modified interplex scheme has to be employed, as explained in [1].

2.4 Modulation

To transmit information in the form of a signal, the original baseband signal called modulating signal, is transformed into another one due to a process called modulation. In this section we will present the theory behind the three most used modulations in GNSS signals: **Binary Phase Shift Keying** (**BPSK**) (used in GPS L1/C/A signal), **BOC** and **Multiplexed Binary Offset Carrier** (**MBOC**) (used in the E1 signal as the CBOC implementation). Due to its importance in this thesis the AltBOC modulation will be analyzed in detail in chapter 3.

2.4.1 BPSK-R

Binary Phase-Shift Keying uses rectangular symbols (hence called BPSK-R) and is mainly used in the original GPS satellite signal designs. Signals can exhibit different chip rates; therefore this modulation should be represented as BPSK-R(n) where n designates the chip rate multiple of 1.023 MHz or

BPSK(f_c) where f_c designates the chip rate itself. The BPSK-R modulation has a sinc-squared function shaped power spectrum with the first positive null located at the chip rate.

2.4.2 BOC

Binary Offset Carrier (BOC) modulation is a square sub-carrier modulation, where a signal is multiplied by a rectangular sub-carrier $g(t)$ of frequency f_{sc} equal or higher than the chip (CDMA) rate. Following this sub-carrier multiplication, the power spectrum of the signal is divided into two parts separated by $2f_{sc}$; therefore BOC modulation is also known as a split-spectrum modulation.

The main idea behind BOC modulation is to reduce the interference with BPSK-modulated signal, which has a sinc-squared function shaped power spectrum. In fact, BPSK-modulated signals, such as C/A GPS codes, have most of their spectral energy concentrated around the carrier frequency, while BOC-modulated signals (used in Galileo system) have low energy around the carrier frequency and two main spectral lobes further away from the carrier (thus, the name of split-spectrum) as shown in fig. 2.4.

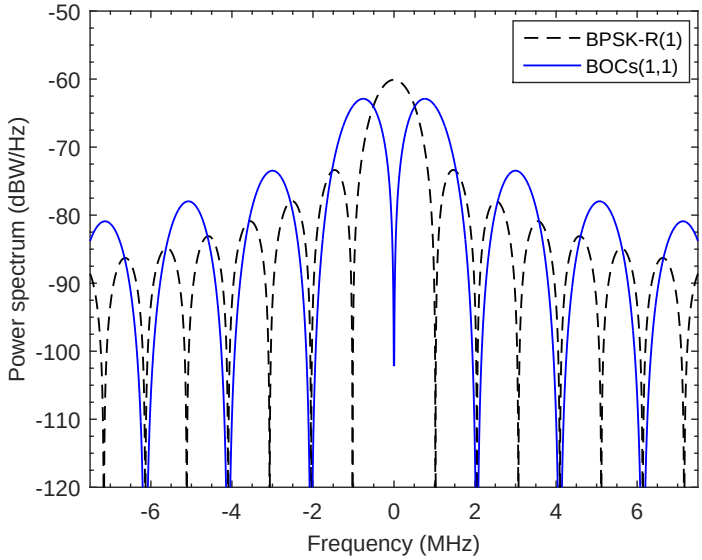

Figure 2.4: BPSK-R(1) and BOCs(1,1) power spectra

BOC modulation has several variants: sine BOC (SinBOC), cosine BOC (CosBOC), Alternative BOC (AltBOC), multiplexed BOC (MBOC), Double BOC (DBOC),etc.

A BOC waveform is typically denoted via BOC(m,n) or BOC(f_{sc},f_c), where f_{sc} is the sub-carrier frequency, f_c is the chip frequency, $m = \frac{f_{sc}}{f_{\text{ref}}}$, $n = \frac{f_c}{f_{\text{ref}}}$, and $f_{\text{ref}} = 1.023$ MChips is the reference chip frequency of the C/A GPS signal.

2.4.3 MBOC

The MBOC(6,1,1/11) implementation adopted by the modernized GPS and Galileo is divided into two main variants:

- CBOC[1][20]: The Composite BOC is the solution adopted by Galileo for the Open Service in E1/L1 band. It is used in an Interplex multiplexing scheme where the sub-carriers BOC(1,1) and BOC(6,1) are added in phase or anti-phase on each channel (data+pilot).

- TMBOC: The Time-Multiplexed BOC is the solution adopted by GPS for L1C band. It is a binary signal where BOC(1,1) and BOC(6,1) are time-multiplexed according to a pre-established pattern that was optimized to improve the correlation properties of the signal when the effect of the PRN code is taken into account.

2.5 GNSS Navigation Equation

Each signal transmitted by a navigation satellite includes, among other things, information concerning the time of transmission, measured by the satellite clock, and parameters (ephemerides) that permit to determine the satellite position (X_i, Y_i, Z_i) in the Earth-centered Earth-fixed (ECEF) referential with a very good accuracy. If the receiver used the same clock as the satellite, and assuming that the satellites clocks are perfectly synchronized, only 3 satellites would suffice to determine the ECEF receiver's coordinates (x_R, y_R, z_R) by solving the set of equations

$$D_i = \sqrt{(X_i - x_R)^2 + (Y_i - y_R)^2 + (Z_i - z_R)^2}, \quad i = 1, 2, 3 \tag{2.4}$$

where D_i is the distance of satellite i to the receiver. That distance is computed by measuring the trip delay of the received signal and multiplying it by the speed of light (c).

Unfortunately, the receiver's clock is affected by an error Δt regarding the satellites clocks, which prevents the exact determination of the receiver's position using the set of equations (2.4). Instead, what is determined from the measured trip delays is a set of pseudoranges

$$\rho_i = \sqrt{(X_i - x_R)^2 + (Y_i - y_R)^2 + (Z_i - z_R)^2} + c\Delta t + \epsilon_i, \quad i = 1, \ldots, N \tag{2.5}$$

where N is the number of satellites in view and ϵ_i are random variables that collect the errors that do not depend on the receiver's clock time offset, such as time errors due the wave propagation through the ionosphere and troposphere and not fully eliminated by measurements or theoretical models, thermal noise effects in the receiver, multipath, interference (jamming), etc. Of all the mentioned errors those introduced by the ionosphere are, in general, the most significant and must be corrected as accurately as possible. The preferred solution consists of using signals from two bands (for instance E1 and E5 in Galileo or L1 and L2 in GPS). Since the time delay provoked by the ionosphere is of the form α/f_c^2, where α is a quantity that depends on the number of free electrons in the path of the signal and f_c is the carrier frequency, by measuring the relative delays of two signals received in different bands permits to determine α, and consequently, the delay induced by the ionosphere. For low cost receivers that operate in a single band this solution is not possible and one has to resort to empirical models of the ionospheric electron density using parameters provided by the navigation data. GPS adopted the Klobuchar model

and Galileo the Nequick model [21]. Obviously, this solution leads to less accurate results than the dual band scheme.

The determination of the exact time of arrival of each satellite signal is crucial to obtain a good accuracy in the receiver's position estimation. This is achieved by aligning (correlating) the spreading code of the incoming signal with the code of a locally-generated replica. The delay-locked loop (DLL) is the circuit used for that purpose. The spreading codes are characterized by very narrow autocorrelation functions which are essentially zero for misalignments exceeding 1 chip interval. The chip duration in the GPS C/A signal is $T_c = 10^{-3}/1023 = 0.978\mu$s being ten times shorter in the Galileo AltBOC(15,10) signal. Assuming an alignment error of 1% of the chip interval, this corresponds to errors of 2.93 m and 0.293 m, respectively, in the pseudorange computation. These results show the advantage of using AltBOC signals instead GPS C/A signals.

Considering that the pseudorange errors ϵ_i in (2.5) are Gaussian, zero-mean, independent, with the same variance σ^2_{uere} (UERE=user equivalent range error) for all the satellites in view, the resulting root mean square error (RMSE) in the receiver's position determination is given by

$$\mathrm{RMSE} = \sigma_{uere} \cdot \mathrm{GDOP} \tag{2.6}$$

where the geometric dilution of precision parameter (GDOP) is determined as

$$\mathrm{GDOP} = \sqrt{\mathrm{tr}(G^T G)^{-1}} \tag{2.7}$$

with G denoting the geometry matrix that depends solely on the geometry of the satellites constellation. In ECEF coordinates the geometry matrix is computed as

$$G = \begin{bmatrix} -\frac{X_1 - x_R}{D_1} & -\frac{Y_1 - y_R}{D_1} & -\frac{Z_1 - x_R}{D_1} & 1 \\ \vdots & \vdots & \vdots & \vdots \\ -\frac{X_N - x_R}{D_N} & -\frac{Y_N - y_R}{D_N} & -\frac{Z_N - x_R}{D_N} & 1 \end{bmatrix} \tag{2.8}$$

The equation of navigation is constituted by the set of equations (2.5) which are solved for the spatial unknowns $(x_R,\, y_R,\, z_R)$ and the time unknown $c\Delta t$. The solution is unambiguous provided that $N \geq 4$ satellites are simultaneously in view. The problem is nonlinear and there are three groups of techniques that can be applied: (i) closed form solutions as the Bancroft's algorithm; (ii) iterative solutions based on linearizations (for instance, the least-squares algorithm); and (iii) Kalman filtering. The application of the extended Kalman filter requires a model for the receiver's dynamics (motion+clock model) but permits to conveniently estimate time, position, velocity and acceleration in the presence of noisy observations.

Equation (2.6) shows that, for a constant value of σ_{uere}, the position estimates improve as the GDOP parameter decreases. In general, selecting a set of satellites widely separated in the sky yields small values of GDOP and is preferable than using a set of nearby satellites. However, in certain cases, like in (urban) canyon scenarios, this is not always possible. Also, the assumption of a common variance σ^2_{uere} for all the satellites is often not verified, especially when operating with satellites having low elevation angles (satellites located near the horizon). In those cases, the path of the transmitted waves through

the ionosphere is very large and the ionospheric delays are more difficult to estimate and eliminate. Therefore, satellites with elevation angles typically below 10 degrees are not used to solve the equation of navigation.

2.6 Sources of Signal Degradation

GNSS signals are received at the earth surface with very small powers. For instance, the GPS C/A signal received power varies from -164 dBW to -156 dBW for satellites at low elevation and zenith, respectively [14]. For a white noise power spectral density of approximately -201 dBW/Hz the resulting signal power to noise power density (C/N_0) ranges from 37 up to 45 dB-Hz. However, in certain scenarios, the received power may be attenuated by several dB or dozens of dB (*shadowing effect*). For example, inside buildings the attenuation may exceed 20 dB which prevents the operation of conventional GNSS receivers.

Other sources of signal degradation are due to the crossing of the atmosphere, namely the propagation through the ionosphere and the troposphere. The degradation (attenuation + delay) depends on the angle of elevation being minimum when the satellite is at the zenith. The delays introduced by the ionosphere are significant but can be eliminated in a large extent by using simultaneously signals transmitted in different bands. Alternatively, empirical models of the ionospheric electron density like the Klobuchar or Nequick models may be utilized, although with lower efficiency. In tropical and polar regions the ionosphere may exhibit rapid density fluctuations (at the rate of 1 Hz or more) which disturbs the reception of GNSS signals by introducing fast (C/N_0) variations (*ionospheric scintillation*). The phase of the signals is also affected which may lead to the loss of lock of the carrier lock loops (PLL/FLL) [22].

Multipath is also an important source of loss of accuracy in navigation systems which consists of receiving several replicas of the same signal with different delays and phases. Since the GNSS receivers measure the trip delay of the incoming signals, the result will be an incorrect determination of those delays.

Besides the disturbances that occur naturally, there are other harmful forms of artificial interference both unintentional or intentional. Sources of unintentional interference are, for example, the spurious emissions of in-band and out-of-band systems, which generate harmonics that collide with the GNSS bandwidths. In case interference is intentional it is called *jamming*. The malicious objective of jamming is to cause the receiver to lose tracking and to prevent signal re-acquisition [23].There is an even more sophisticated way to attack the operation of GNSS receivers which consists in the intentional transmission of a GNSS-like signal, with the purpose of producing a false position within the victim receiver without disrupting the GNSS operation. This type of interference is called spoofing [23].

Chapter 3

E5 Signal

This chapter's main purpose is to thoroughly define and characterize the Galileo E5 signal denoted AltBOC(15,10), which will be used in the receivers developed in this thesis. Recently, China has also shown interest in implementing the E5 AltBOC signal in its Beidou Phase 3 system [24]. Section 1 explains the Galileo services and its connection to the E5 signal. Section 2 defines the transmitted signal while section 3 presents an equivalent signal representation. Section 4 explains the used codes that compose the signal. Section 5 determines the autocorrelation function and power spectral density of the E5 AltBOC signal and finally section 6 gives an insight about the signal power and signal to noise ratio.

3.1 Galileo Services

Galileo provides four basic satellite navigation services to worldwide users [1], [25]:

- Open Service (OS) - Free of charge for all users;
- Safety of Life Service (SoL) - Improves the OS performance through the provision of timely warnings to the user when it fails to meet certain margins of accuracy (integrity). This service is made available for safety-critical applications such as running trains, guiding cars, navigation and aviation;
- Commercial Service (CS) - Access to two additional encrypted and guaranteed signals, delivering a higher data throughput rate and increased accuracy;
- Public Regulated Service (PRS) - Provides position and timing to specific users requiring a high continuity of service, with controlled access.

The Galileo signals are assigned to provide the service categories that are summarized in the table 3.1.

For example, the single-frequency OS is provided by each of the three signals: E1B,C, E5a and E5b. The dual-frequency OS is provided by the signal combinations: E1B,C-E5a and E1B,C-E5b. The table

	OS	SoL	CS	PRS
E5a	X		X	
E5b	X	X	X	
E6A				X
E6B,C			X	
E1A				X
E1B,C	X	X	X	

Table 3.1: Galileo services mapped to signals

shows that the signals of the E5 band are used by the OS, SoL and CS services both in single-frequency and double-frequency reception schemes. The double-frequency schemes permit to minimize the effect of the ionospheric delays on the pseudoranges.

3.2 E5 transmitted signal

The AltBOC signal, more specifically AltBOC(15,10), is defined by the standard BOC(m,n) notation where $m = \frac{f_{sc}}{1.023\times10^6}$ is the sub-carrier frequency multiple value of 1.023 MHz and $n = \frac{f_{co}}{1.023\times10^6}$ is the code chipping rate multiple value of 1.023 MChips/s. This type of notation is used by the BOC modulation family since it has both a code chipping rate and a sub-carrier frequency associated to its constitution. Thus, the AltBOC modulation is characterized by a chipping rate of 10.23 MChips/s and a digital sub-carrier with frequency 15.345 MHz. The GNSS signals that do not use sub-carriers modulation only need one number to completely define its structure (e.g. BPSK(1) corresponds to the standard GPS L1 C/A which has a 1.023 MChips/s code chipping rate, see fig. 2.3).
As shown in the previous chapter, all GNSS transmitted signals modulated with the carrier can be defined using (2.1) which for E5 specifically takes the form:

$$S_{RF}(t) = \sqrt{2P_T} \cdot [s_I(t)\cos(2\pi f_c t) - s_Q(t)\sin(2\pi f_c t)] \tag{3.1}$$

where P_T is the power of $S_{RF}(t)$, $f_c = 1191.795$ MHz is the centre carrier frequency of the E5 signal band and $s(t) = s_I(t) + js_Q(t)$ is the complex baseband signal with unity power. The E5 complex baseband signal has four spreading codes (AI,AQ,BI,BQ) that are modulated onto in-phase and quadrature-phase components of orthogonal complex sub-carriers as shown in [13]:

$$\begin{aligned} s_{E5}(t) &= \frac{1}{2\sqrt{2}}[e_{E5a-I}(t) + je_{E5a-Q}(t)][sc_{E5-S}(t) - jsc_{E5-S}(t - T_s/4)] \\ &+ \frac{1}{2\sqrt{2}}[e_{E5b-I}(t) + je_{E5b-Q}(t)][sc_{E5-S}(t) + jsc_{E5-S}(t - T_s/4)] \\ &+ \frac{1}{2\sqrt{2}}[\overline{e}_{E5a-I}(t) + j\overline{e}_{E5a-Q}(t)][sc_{E5-P}(t) - jsc_{E5-P}(t - T_s/4)] \\ &+ \frac{1}{2\sqrt{2}}[\overline{e}_{E5b-I}(t) + j\overline{e}_{E5b-Q}(t)][sc_{E5-P}(t) + jsc_{E5-P}(t - T_s/4)] \end{aligned} \tag{3.2}$$

Each of the spreading codes is defined as

$$
\begin{aligned}
e_{E5_{a-I}}(t) &= \sum_{i=-\infty}^{\infty} [c_{aI,|i|_{L_{aI}}} \cdot c_{s,aI,|i|_{L_{s,aI}}} \cdot d_{aI,|\frac{i}{D_{aI}}|} \cdot \Pi_{T_c}(t - i \cdot T_c)] \\
e_{E5_{a-Q}}(t) &= \sum_{i=-\infty}^{\infty} [c_{aQ,|i|_{L_{aQ}}} \cdot c_{s,aQ,|i|_{L_{s,aQ}}} \cdot \Pi_{T_c}(t - i \cdot T_c)] \\
e_{E5_{b-I}}(t) &= \sum_{i=-\infty}^{\infty} [c_{bI,|i|_{L_{bI}}} \cdot c_{s,bI,|i|_{L_{s,bI}}} \cdot d_{bI,|\frac{i}{D_{bI}}|} \cdot \Pi_{T_c}(t - i \cdot T_c)] \\
e_{E5_{b-Q}}(t) &= \sum_{i=-\infty}^{\infty} [c_{bQ,|i|_{L_{bQ}}} \cdot c_{s,bQ,|i|_{L_{s,bQ}}} \cdot \Pi_{T_c}(t - i \cdot T_c)]
\end{aligned}
\tag{3.3}
$$

where [a,b] stands for E5a and E5b signals respectively, [I,Q] represents the in-phase and quadrature-phase respectively, 'c' stands for code bit (chip), 'd' stands for data bit and $[L, L_s]$ stand respectively for the primary and secondary code length (repetition period). The rectangle function is defined as:

$$
\Pi_{T_c}(t - t_0) = \begin{cases} 1, & t_0 \leq t < t_0 + T_c \\ 0, & \text{otherwise} \end{cases}
\tag{3.4}
$$

where T_C is the chip duration.

The $E5$ signal components are generated according to:

- e_{5a-I} from the F/NAV navigation data stream D_{E5a-I} modulated with the ranging code C_{E5a-I}
- e_{5a-Q} (pilot component) from the ranging code C_{E5a-Q}
- e_{5b-I} from the I/NAV navigation data stream D_{E5b-I} modulated with the ranging code C_{E5b-I}
- e_{5b-Q} (pilot component) from the ranging code C_{E5b-Q}

The modulation scheme for the E5 signal is shown in fig. 3.1. As we can see, only the in phase components have data bits in their composition, the quadrature components are only used as pilot codes.

The dashed signal components in (3.2) also called 'product' signals are used to make the envelope of the modulated signal constant and are defined as:

$$
\overline{e}_{E5a-I} = e_{E5a-Q} \cdot e_{E5b-I} \cdot e_{E5b-Q} \tag{3.5}
$$

$$
\overline{e}_{E5b-I} = e_{E5b-Q} \cdot e_{E5a-I} \cdot e_{E5a-Q} \tag{3.6}
$$

$$
\overline{e}_{E5a-Q} = e_{E5a-I} \cdot e_{E5b-I} \cdot e_{E5b-Q} \tag{3.7}
$$

$$
\overline{e}_{E5b-Q} = e_{E5b-I} \cdot e_{E5a-I} \cdot e_{E5a-Q} \tag{3.8}
$$

The signals $sc_{E5-S}(t)$ and $sc_{E5-P}(t)$ in equation (3.2) refer to the four-level single and product sub-carriers respectively and are represented by:

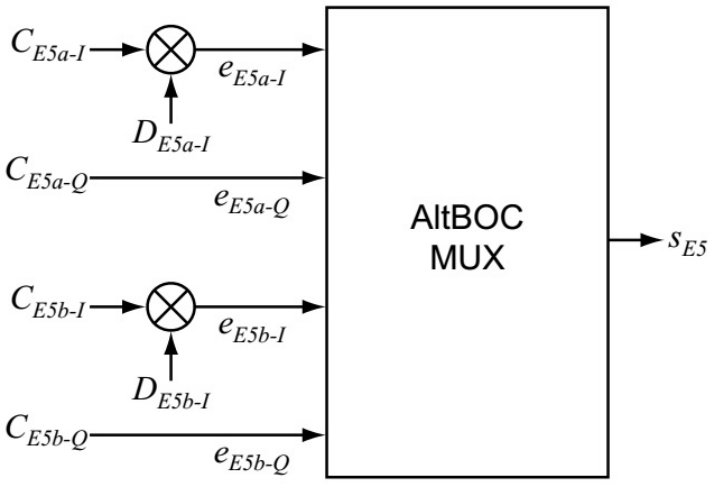

Figure 3.1: Modulation scheme for the E5 signal [13]

$$\begin{aligned} sc_{E5-S}(t) &= \sum_{i=-\infty}^{+\infty} AS_{|i|_8} \Pi_{T_{s,E5}/8}(t - iT_{s,E5}/8) \\ sc_{E5-P} &= \sum_{i=-\infty}^{+\infty} AP_{|i|_8} \Pi_{T_{s,E5}/8}(t - iT_{s,E5}/8) \end{aligned} \tag{3.9}$$

Each sub-carrier has a frequency $f_{sc} = 15.345$ MHz (15 x 1.023 MHz) and the AS_i and AP_i coefficients are given in table 3.2.

i	0	1	2	3	4	5	6	7
2 *ASi*	$\sqrt{2}+1$	1	-1	$-\sqrt{2}-1$	$-\sqrt{2}-1$	-1	1	$\sqrt{2}+1$
2 *APi*	$-\sqrt{2}+1$	1	-1	$\sqrt{2}-1$	$\sqrt{2}-1$	-1	1	$-\sqrt{2}+1$

Table 3.2: AltBOC sub-carrier coefficients [13]

Expression (3.9) with coefficients given by table 3.2 results in subdivided leveled sinusoidal kind of wave shown in figure 3.2.

The complex Fourier series for sub-carrier $sc_{e5-S}(t)$ is:

$$sc_{E5-S}(t) = \sum_{i=-\infty}^{+\infty} c_n \exp(j2\pi n f_{sc} t) \tag{3.10}$$

where the Fourier coefficients are given by

$$c_n = \begin{cases} \frac{1}{2}\text{sinc}(\frac{n}{2})[1 + \sqrt{2}\cos(\frac{\pi n}{4})], & n \neq 0 \\ 0, & n = 0 \end{cases} \tag{3.11}$$

where $\text{sinc}(\text{x}) = \sin(\pi \text{x})/(\pi \text{x})$.

The coefficients with positive index are equal to $c_1 = \frac{2}{\pi}$, $c_2 = ... = c_6 = 0$, and $c_7 = \frac{-2}{7\pi}$. Thus, the

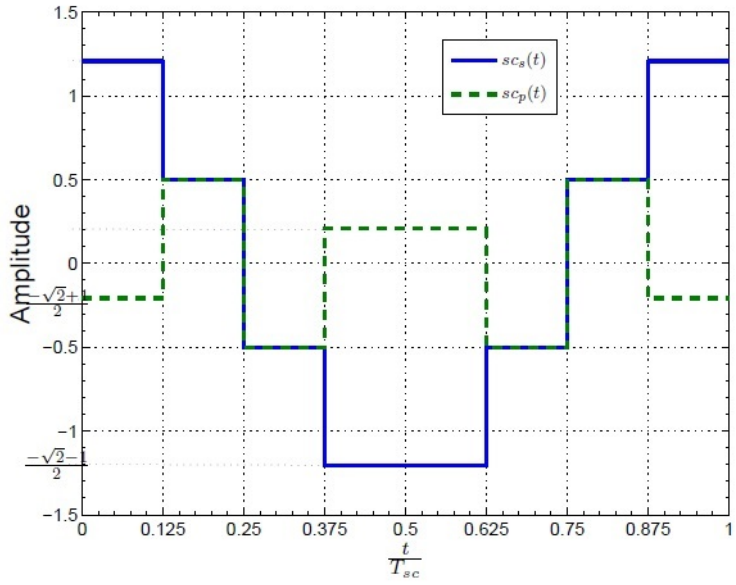

Figure 3.2: One period of the E5 sub-carriers [13]

sub-carrier is well approximated by

$$sc_{E5-S}(t) \approx \frac{4}{\pi}\cos(2\pi f_{sc}t) \tag{3.12}$$

provided that we apply ideal lowpass filtering with cutoff frequency smaller than $7f_{sc} = 107.415$ MHz.

3.3 E5 equivalent representation

Expression (3.2) in the previous section can also be described as an 8-PSK signal defined by expression (3.13) and figure 3.3 which can give a better insight of the values that the signal can take:

$$s_{E5}(t) = \exp\left[j\frac{\pi}{4}k(t)\right] \quad \text{with} \quad k(t) \in [1,2,3,4,5,6,7,8] \tag{3.13}$$

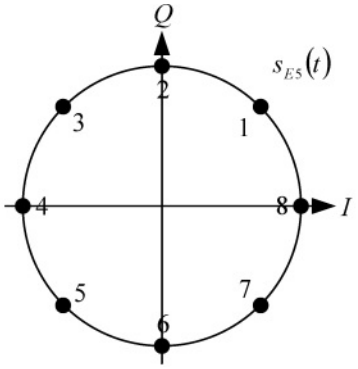

Figure 3.3: 8-PSK constellation [13]

So we can assume that the value of $s_{E5}(t)$ depends on the "position" of $k(t)$ which varies according to different values of the codes $[aI, bI, aQ, bQ]$ and sub-carrier sub-periods as shown in table 3.3.

		Input Quadruples															
eE5a-I		-1	-1	-1	-1	-1	-1	-1	-1	1	1	1	1	1	1	1	1
eE5b-I		-1	-1	-1	-1	1	1	1	1	-1	-1	-1	-1	1	1	1	1
eE5a-Q		-1	-1	1	1	-1	-1	1	1	-1	-1	1	1	-1	-1	1	1
eE5b-Q		-1	1	-1	1	-1	1	-1	1	-1	1	-1	1	-1	1	-1	1
$t' = t$ modulo $T_{s,E5}$		k according to $s_{E5}(t)=exp(jk\pi/4)$															
i_{Ts}	t'																
0	[0,$T_{s,E5}$/8[	5	4	4	3	6	3	1	2	6	5	7	2	7	8	8	1
1	[$T_{s,E5}$/8, 2 $T_{s,E5}$/8[	5	4	8	3	2	3	1	2	6	5	7	6	7	4	8	1
2	[2 $T_{s,E5}$/8, 3 $T_{s,E5}$/8[	1	4	8	7	2	3	1	2	6	5	7	6	3	4	8	5
3	[3 $T_{s,E5}$/8, 4 $T_{s,E5}$/8[	1	8	8	7	2	3	1	6	2	5	7	6	3	4	4	5
4	[4 $T_{s,E5}$/8, 5 $T_{s,E5}$/8[	1	8	8	7	2	7	5	6	2	1	3	6	3	4	4	5
5	[5 $T_{s,E5}$/8, 6 $T_{s,E5}$/8[	1	8	4	7	6	7	5	6	2	1	3	2	3	8	4	5
6	[6 $T_{s,E5}$/8, 7 $T_{s,E5}$/8[	5	8	4	3	6	7	5	6	2	1	3	2	7	8	4	1
7	[7 $T_{s,E5}$/8, $T_{s,E5}$[	5	4	4	3	6	7	5	2	6	1	3	2	7	8	8	1

Table 3.3: Look-up table for AltBOC phase states [13]

As one can see, with a fixed set of codes, the values of the AltBOC signal change between two complex values only, spaced by an argument of π to produce a minimal error situation, contributing to a more solid signal.

3.4 Ranging E5 Codes

The satellite ranging codes are what identifies and define each satellite E5 transmitted signal. These codes are obtained by summing the primary and secondary codes as explained in this section.
The period and length of the E5 signal codes are shown in table 3.4.

Signal Component	Tiered Code Period (ms)	Code Length (chips)	
		Primary	Secondary
E5a-I	20	10230	20
E5a-Q	100	10230	100
E5b-I	4	10230	4
E5b-Q	100	10230	100

Table 3.4: Code lengths and period [13]

Each chip of the secondary code will be summed to a cycle of the primary code (10230 chips) so the period of the tiered code will be the same as the period of the secondary code depicted in figure 3.4.
The addition of the secondary code permits to increase significantly the period of the resulting (tiered) code from 1 ms (period of the primary code) to an extended period of 4 to 100 ms, thus minimizing the

ambiguity in the positioning determination (1 ms corresponds to an ambiguity of 300 km and 100 ms corresponds to 30 thousand km).

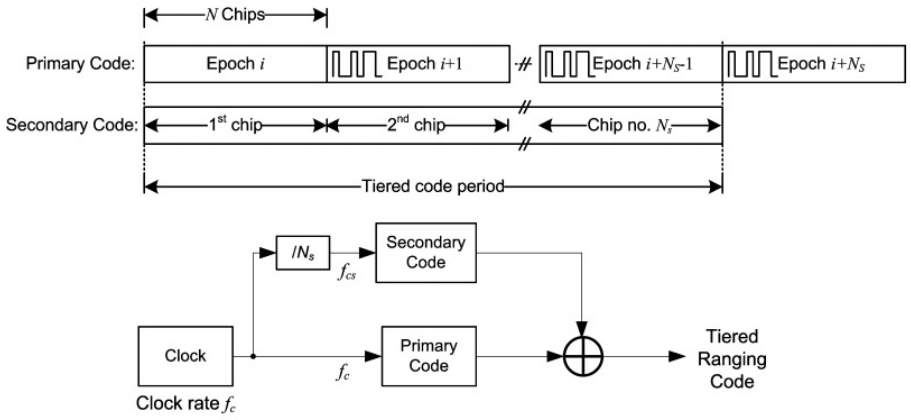

Figure 3.4: Tiered code generation [13]

3.4.1 Primary Codes

Primary codes can be obtained by memory saved sequences or generated register-based sequences. The primary code generation method is equal to all satellites, the only difference being the initial sequence of values given to the process. The method and initial sequence listing are accessible in the official Interface Control Document (ICD) [13].

Figure 3.5 shows the diagram that represents the register-based primary code generation based on Linear Feedback Shift Register (LFSR).

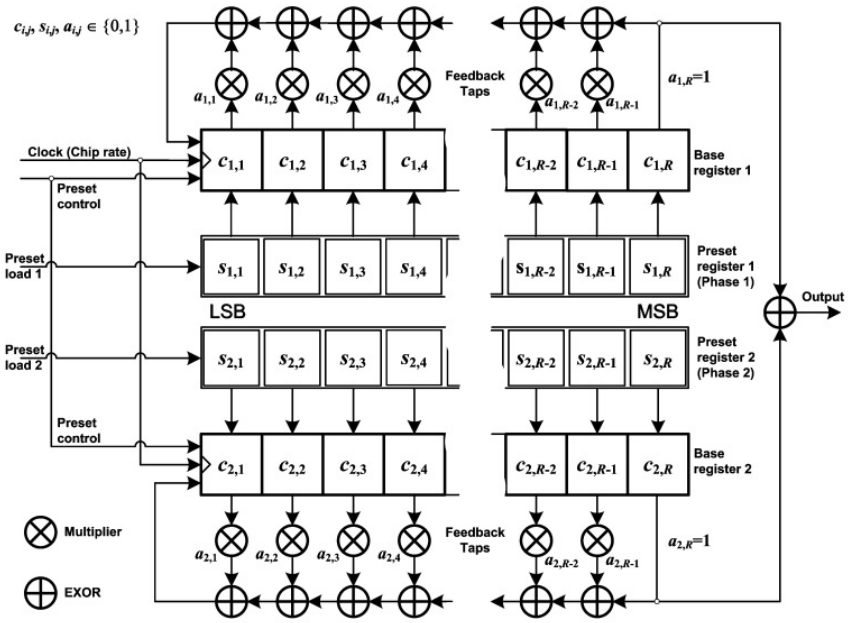

Figure 3.5: LFSR based code generator for truncated and combined M-sequences [13]

The process consists of two main independent 'c' sequences that are summed bit by bit to generate

the desired code output. In the figure, the 's' blocks represent the initial sequence called the 'preset load', the 'c' blocks represents the actual generated working sequence and 'a' represent the array of feedback positions. Each satellite has two initial sequence array different from all others that are supplied to the two initial 'c' sequences. The register positions that are fed back are given by the constant 'a' block array shown in table 3.5.

Component	Shift Register Length (polynomial order)	Feedback Taps (octal)	
		Register 1	Register 2
E5a-I	14	40503	50661
E5a-Q	14	40503	50661
E5b-I	14	64021	51445
E5b-Q	14	64021	43143

Table 3.5: E5 primary codes specifications [13]

The feedback taps have octal values and need to be transformed into a binary array. An example is given in figure 3.6 to illustrate how the feedback taps are used.

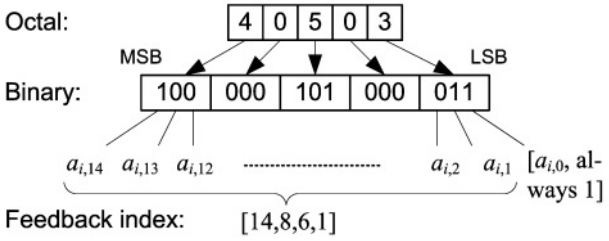

Figure 3.6: Example of E5a-I feedback tap [13]

As one can see, after the transformation to a binary array, the resulting '1' bits give the positions that are fed back to the main 'c' array sequence. These feedback positions are constant throughout the process until the code completes the cycle length (10230).

3.4.2 Secondary Codes

The secondary codes may not be generated as register based sequences and are fixed hexadecimal sequences. Table 3.6 contains the secondary code assignment for the AltBOC signal. The sequence values and satellite correspondence are listed in the official ICD document for the $E5_{a-Q}$ and $E5_{b-Q}$ components.

3.5 Autocorrelation Function and Power Spectral Density

The Autocorrelation Function (hence ACF) and Power Spectral Density (hence PSD) of a signal are important characteristics that give useful information and powerful tools to digitally manipulate and analyze the nature of the signal.

Component	Secondary Code Assignment
E5a-I	$CS20_1$
E5a-Q	$CS100_{1\text{-}50}$
E5b-I	$CS4_1$
E5b-Q	$CS100_{51\text{-}100}$

Table 3.6: Secondary code assignment [13]

3.5.1 Autocorrelation Function

The ACF is a property that enables the comparison between a signal and its delayed version and to calculate that delay. This property is really useful in the GNSS domain since it can align the received signal with a locally generated replica and derive the delay caused by the distance between transmitter-receiver using a Delay Locked Loop (hence DLL). As derived in [26] the autocorrelation function for the E5 AltBOC signal can be analytically calculated as:

$$\begin{aligned} R_{AltBOC(15,10)}(\tau) =& 8\Lambda_{T_c/6}(\tau) - \frac{16}{3}\Lambda_{T_c/6}\left(|\tau| - \frac{T_c}{3}\right) + \frac{8}{3}\Lambda_{T_c/6}\left(|\tau| - \frac{2T_c}{3}\right) \\ & - \frac{1}{3}\Lambda_{T_c/12}\left(|\tau| - \frac{T_c}{12}\right) - \frac{1}{3}\Lambda_{T_c/12}\left(|\tau| - \frac{3T_c}{12}\right) \\ & + \frac{1}{3}\Lambda_{T_c/12}\left(|\tau| - \frac{5T_c}{12}\right) + \frac{1}{3}\Lambda_{T_c/12}\left(|\tau| - \frac{7T_c}{12}\right) \\ & - \frac{1}{3}\Lambda_{T_c/12}\left(|\tau| - \frac{9T_c}{12}\right) - \frac{1}{3}\Lambda_{T_c/12}\left(|\tau| - \frac{11T_c}{12}\right) \end{aligned} \tag{3.14}$$

where T_c is the chip duration ($\frac{1}{10*1.023*10^6}$), τ is the delay and Λ is the triangle function defined as

$$\Lambda_L(t) = \begin{cases} 1 - \frac{|t|}{L}, & |t| < L \\ 0, & \text{otherwise} \end{cases} \tag{3.15}$$

therefore

$$\Lambda_L(|t| - t_0) = \Lambda_L(t - t_0) + \Lambda_L(t + t_0) \tag{3.16}$$

Expression (3.14) assumes that the power of the AltBOC signal is $R_{AltBOC(15,10)}(0) = 8$. Fig. 3.7 exhibits the normalized auto-correlation function corresponding to (3.14).

Ideally an ACF should resemble a triangle with the peak centered at zero if the signal had ideal correlation properties but as one can see, the AltBOC ACF shows four additional peaks (two positive and two negative) meaning that depending on the autocorrelation value discriminators, the alignment can result in wrong values of time delay if a non-coherent early-late code discriminator is applied. This effect is known as false code-lock.

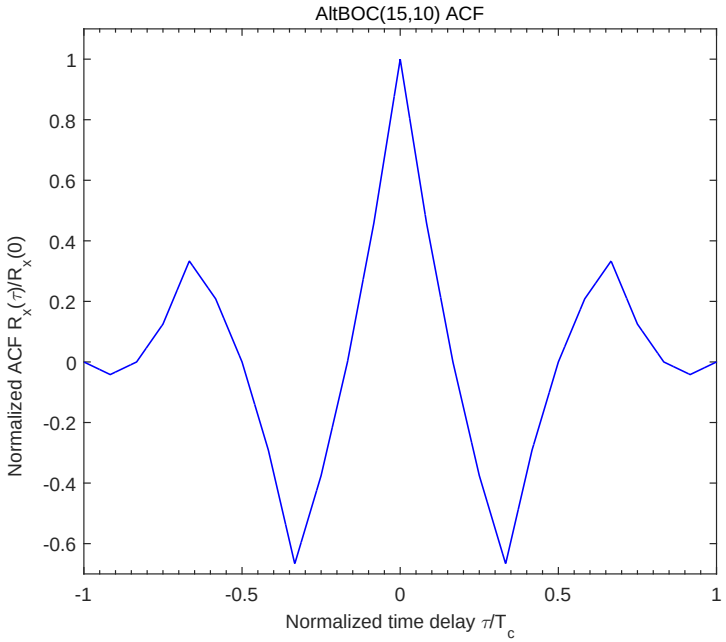

Figure 3.7: Normalized AltBOC(15,10) autocorrelation function

3.5.2 Power Spectral Density

The PSD property characterizes the signal power in the frequency domain. It shows where the signal can be found and narrows the search and bandwidth needed to fully acquire the signal. As shown in [26] the AltBOC PSD can be obtained as the Fourier transform of the ACF expression given by (3.14) resulting in:

$$G_{AltBOC(15,10)}(f) = \frac{T_c \cos^2(\pi f T_c)}{9\cos(\frac{\pi f T_c}{3})}\left[\frac{4\,\mathrm{sinc}^2(\frac{fT_c}{6})}{\cos(\frac{\pi f T_c}{3})} - \mathrm{sinc}^2\left(\frac{fT_c}{12}\right)\cos\left(\frac{\pi f T_c}{6}\right)\right] \tag{3.17}$$

The resulting graph for the normalized PSD (unity power signal) is shown in figure 3.8.

A wideband receiver front-end has a typical bandwidth value of 51.15 MHz [13]. This means that the filter can acquire the two side lobes which we call sub-bands A and B. The receiver can fully take advantage of the properties of the signal by manipulating both bands separately or combined. This is the widest bandwidth of any satellite navigation signal currently defined, having the narrowest correlation function peak [24].

3.6 Received Signal Power and SNR

The minimum received power on ground is measured at the output of an ideally matched RHCP 0 dBi polarized user receiving antenna when the satellite elevation angle is higher than 10 degrees. The values for sub-bands E5a and E5b are indicated in table 3.7.

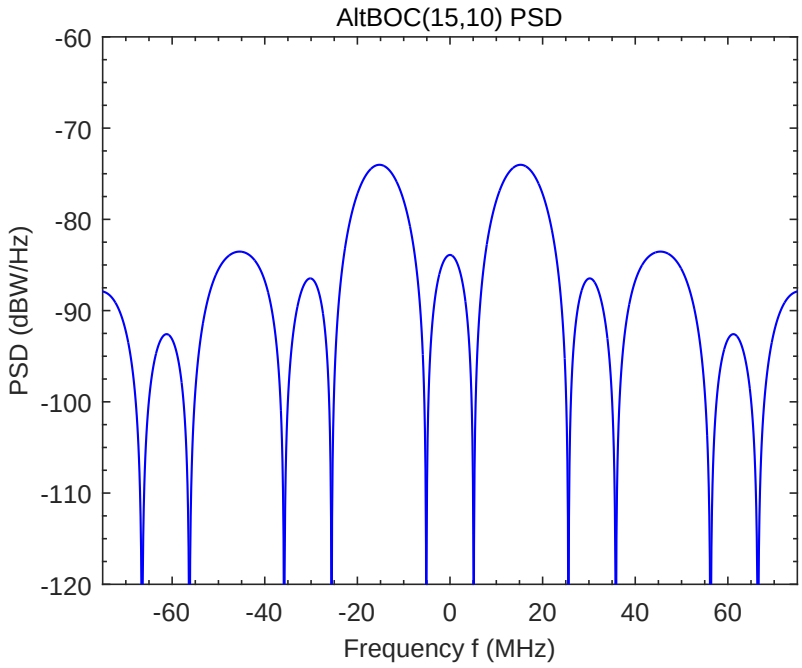

Figure 3.8: Normalized power spectral density of AltBOC(15,10)

Signal	Signal Component	Total Received Minimum Power (dBW)
E5	E5a (total I+Q) (50/50% I/Q power sharing)	-155
	E5b (total I+Q) (50/50% I/Q power sharing)	-155

Table 3.7: Received minimum power levels on ground [13]

Assuming a typical noise density of $N_0 = -201$ dBW/Hz for the thermal noise at the receiver front-end [14], the minimum carrier-to-noise density ratio for a full-band receiver is $C/N_0 = -155 + 10\log_{10}(2) + 201 = 49$ dB-Hz and $C/N_0 = 46$ dB-Hz for a single-band receiver.

Chapter 4

GNSS Receivers

This chapter will give some basic insights about the general structure and functioning process of a GNSS receiver. Section 1 presents a general receiver structure. Section 2 presents the concept behind the signal acquisition process. Section 3 introduces the basics of signal tracking. Section 4 describes the analysis of noise performance of the discriminators and Section 5 presents the problem of Multipath interference.

GNSS receivers are responsible for processing the desired band Signals In Space (SIS) coming from the GNSS satellites. User receivers search for the presence of these radio signals that travel through space, and try to synchronize with them. This way, a GNSS receiver can be seen as a radionavigation user device that aims at tracking the GNSS signals, in order to correctly demodulate and extract the measurements and navigation information - one example is to decode the transmitted navigation message and calculate the user's position.
GNSS receivers have three main objectives:

- Acquisition of the desired space signal
- Tracking of the previously acquired signal
- Data and information demodulation.

4.1 GNSS Receiver Architecture

The generic GNSS Receiver representation is sketched in figure 4.1.

Though we can generalize the receiver's architecture, each receiver has certain specifications to ensure its normal functioning (e.g. a receiver designed for road applications may have less stringent power requirements than a receiver designed for outdoor environments).

In the subsequent sections, we will describe briefly each block of the diagram, giving a special emphasis to the baseband processing block since it is the main subject of our study.

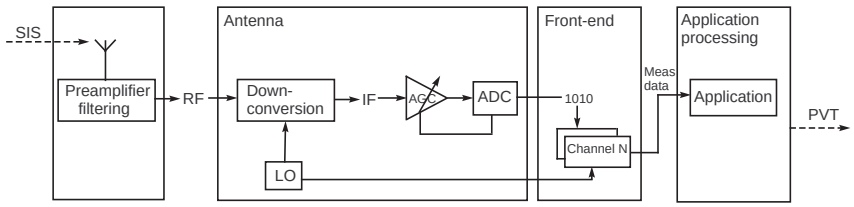

Figure 4.1: Block diagram of a typical GNSS receiver, illustrating the different parallel processing channels

In the example of fig. 4.1 the Local Oscillator (LO) permits to heterodyne the RF of the incoming signal to a lower Intermediate Frequency (IF) where the signals are sampled at the Analog-to-Digital Converter (ADC). An alternative to this architecture, which is gaining popularity, consists of heterodyning the signals to zero IF. These are called homodyne front ends. The advantage is that the required sampling rate is minimal [24]. The implemented receivers to be described in chapter 5 are of homodyne type.

4.1.1 Antennas

GNSS antennas are Right Hand Circularly Polarized (RHCP) and aim at capturing GNSS signals in the L-band (frequency interval where all GNSS signals can be found), with the associated amplification and filtering. It is the entry point from the space segment to the user segment, as it receives the L-band signals to pre-process and feed as an analog electrical signal to the front end (still as a 1.2 - 1.6 GHz range RF signal).

When designing a GNSS antenna, the main objective is to maximize the antenna gain towards emitting satellites above a given elevation angle, while rejecting multipath signals (usually at lower elevation angles) and interference. The design of the antenna has to cope with the environmental conditions of the target application, while respecting mobility, power and size constraints. Usually GNSS antennas present hemispherical radiation patterns that can reject multipath coming from low elevation angles. The RHCP antennas also help reject the reflected signals as these are Left Hand Circularly Polarized due to the polarization inverting at reflection.

As far as interference is concerned, antenna arrays can be used to modify the radiation pattern so as to reject signals coming from the direction of the interferer. In addition, beam steering techniques are often employed to ”follow” the signal from a given satellite with maximum gain.

Another important parameter is phase stability and repeatability in applications that use carrier phase measurements to provide a navigation solution, e.g. Real Time Kinematic (RTK).

4.1.2 Front End

The front end section receives the RF inputs from the antenna, and performs down-conversion, filtering / amplification, and sampling (digitizing) of the captured signals. Typically in a superheterodyne configuration, the front end converts the analog GNSS signals to digital data streams in an Intermediate

Frequency (IF) spectrum (centered in the MHz range), and finally to a baseband digital signal in-phase (I) and quadrature (Q) components. Additional parameters that affect the front-end are:

- Local Oscillator (LO): should present short-term and long-term stability and low phase noise. To ensure good stability and low phase noise, the receiver oscillators are often driven by a quartz or rubidium oscillator. For improved stability the quartz oscillators may be temperature compensated (TCXO) or ovenized (OCXO) [27].
- Frequency synthesizer: the design of the receiver frequency plan takes into account not only the target GNSS signals and their characteristics, but also sampling frequencies and intermediate frequencies that maximize overall performance (e.g. rejecting down-conversion harmonics, out of band interference and minimizing phase noise impact).

4.1.3 Baseband Processing

The baseband processing block is responsible for processing the down-converted and digitized GNSS signal in order to provide the code pseudo-ranges, carrier phase measurements and navigation data. Additional information, such as Doppler frequency, Carrier-to-Noise ratio, or lock indicators, can also be provided.
In most GNSS receivers' architectures, the baseband processing relies on independent channels that track each satellite signal autonomously. Then, the information from each channel is integrated to derive a navigation solution.
Figure 4.2 gives a visual insight of the baseband processing block:

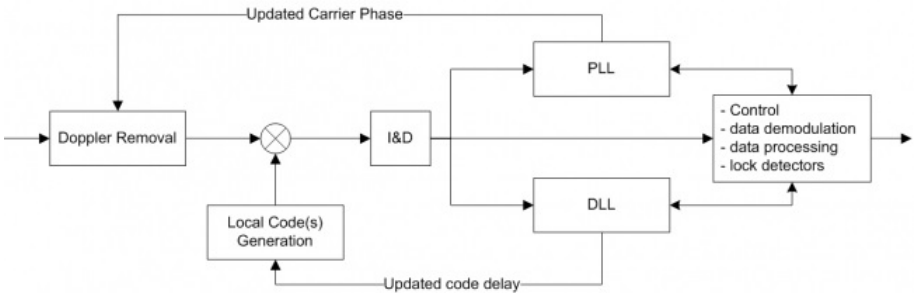

Figure 4.2: Generic diagram of a single channel in the baseband processing block [25]

The basic principle of GNSS baseband processing relies on the correlation process. The underlying idea is that GNSS signals convey ranging codes that are built in a way that:

- When the code is correlated with an aligned replica of itself, the correlation output is maximum: high auto-correlation properties.
- When the code is correlated with a non-aligned replica of itself, the correlation output is low. The correlation drops to zero typically with delays larger than one chip, which corresponds to a pseudorange error of about 293.26 m for the GPS C/A signals and 29.33 m for the AltBOC signals. Note, however, that the correlation function of the primary code is periodic with period equal to 1 ms, which corresponds to an ambiguity range of 300 km.

- When the code is correlated with another code of the same family, the correlation output is low: low cross-correlation properties.

The receiver first assigns each channel a Pseudo Random Noise (PRN) code: for GNSS based on Code Division Multiple Access (CDMA) (such as GPS and Galileo), each satellite transmits a dedicated PRN code, whereas for GNSS based on Frequency Division Multiple Access (FDMA) (such as GLONASS), the PRN code is the same for all satellites.
At channel level, the incoming signal is correlated with the local replica of this PRN code and a local carrier replica (to remove the residual carrier Doppler). These local replicas are generated in such a way that its code delay and phase characteristics vary, representing a two-dimensional search over code and (Doppler) frequency. Whenever the local replica parameters (code and frequency) match those of the incoming signal, the correlation output will reach a maximum, and the receiver will consider this pair (code and frequency) as the current estimates for these parameters. This procedure is known as the receiver's acquisition mode.
Real-life systems are very noisy and dynamic: as a consequence, the autocorrelation peak seems to fluctuate at each time instant. This fact justifies the need for tracking loops (accumulators and filters) to continuously "follow" the incoming signal, since an error of 1 ms in the code delay would lead to an error of around 300 km in the pseudorange measurement. The use of tracking loops to estimate the code delay and Doppler frequency leads to the receiver tracking mode.

Basic signal acquisition information can be found in the next section and signal tracking will be described with special emphasis because of its importance on the context of this work.

4.1.4 Application Processing

The last diagram block of fig. 4.1 (application processing) receives data from the N active channels, with $N \geq 4$, in the form of noisy pseudoranges and Doppler frequencies and computes the receiver's position and time (and may also include velocity and acceleration). As referred in chapter II, three different groups of techniques can be used to solve the navigation problem using the set of equations (2.5): closed form solutions, iterative solutions based on linearizations as the least-squares (LS) and weighted (WLS) least-squares algorithms, and Kalman filtering.

Many navigation problems include the following four steps [28]:

1. Start with an a priori estimate of state.

2. Predict the pseudoranges you would get with that state.

3. Take the actual pseudorange mesurements.

4. Update the a priori state, based on the difference between the actual and predicted pseudorange measurements.

In the basic GNSS navigation problem, the state contains four components: x, y and z (coordinates of position), and b (the common clock bias found in the pseudoranges).

Assume the following linear relationship between the a priori pseudorange increments ΔZ and the state increment ΔX

$$\Delta Z = G\,\Delta X + \epsilon \tag{4.1}$$

where G is the geometry matrix and ϵ is a vector of measurement errors. Provided that there are at least 4 independent rows in G one can solve for ΔX using, for example, the standard least-squares (LS) solution

$$\Delta \widehat{X} = (G^T G)^{-1} G^T \Delta Z \tag{4.2}$$

If the measurement errors in vector ϵ do not all have the same variance, and the variances are known, then using the weighted least-squares (WLS) solution can provide smaller errors. However, WLS solutions should be used with care. If the a priori estimates of the variances are incorrect, the weighting can magnify, rather than mitigate, estimation errors [24].

Kalman filtering [29], although being the most complicated of the three groups of solutions, provides the best performance in the presence of noisy measurements and permits also to estimate conveniently velocity and acceleration. The quantities to be estimated, x, y and z components of position, velocity and acceleration, besides the two components of the receiver's clock error, are included in the state vector X_k with dimension equal to 5 in the P (position) model, equal to 8 in the PV (position+velocity) model, and equal to 11 in the PVA (position+velocity+acceleration) model.

The discrete-time dynamics model is defined by the stochastic equation

$$X_{k+1} = \Phi_k X_k + U_k, \quad k = 1, 2, \ldots \tag{4.3}$$

where Φ_k is the state-transition matrix and U_k is the dynamics noise vector. The nonlinear measurements model is constituted by the set of equations (2.5) and takes the form

$$Z_k = h(X_k) + V_k, \quad k = 1, 2, \ldots \tag{4.4}$$

The extended Kalman filter (EKF) is updated recursively typically at the rate of 1 to 10 Hz according to the block diagram of fig. 4.3. In each iteration k the EKF updates the estimate of the state vector as $\widehat{X}(k|k) \rightarrow \widehat{X}(k+1|k) \rightarrow \widehat{X}(k+1|k+1)$ and the step (filtering or prediction) covariance matrix as $P(k|k) \rightarrow P(k+1|k) \rightarrow P(k+1|k+1)$. Initial estimates $\widehat{X}(1|0)$ and $P(1|0)$ are required to start the operation of the algorithm.

The positioning errors obtained by solving the navigation equation depend in part on the variance of the noisy pseudoranges. However, since Doppler frequency estimates are also available from the PLLs or Costas loops, they can be used to improve the estimated position. In fact, while an error of 5% of the chip duration in the code tracking corresponds to about 14.7 m for BPSK-R(1), BOCs(1,1) and CBOC

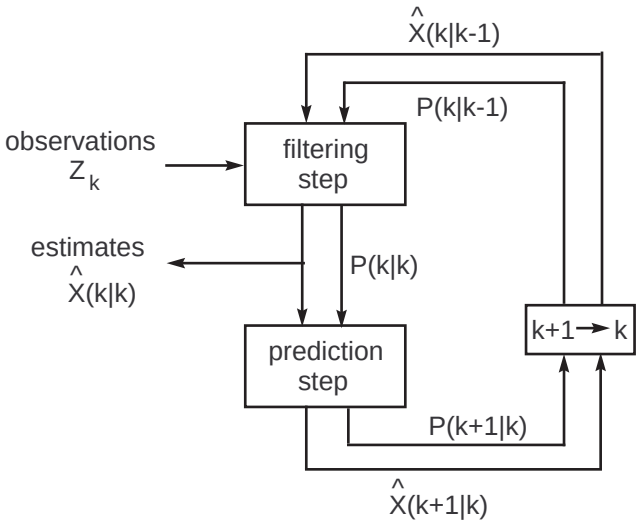

Figure 4.3: Block diagram of the EKF

modulations and to 1.47 m for AltBOC modulation, the same percentage of 5% in the wavelength error (phase error of 18 degrees) corresponds to less than 1.5 cm for carrier frequencies above 1 GHz. This fact is used in the Hatch filter by combining the carrier phase measurements (accurate but exhibiting multiple ambiguities of the wavelength) with code tracking measurements (non-ambiguous but showing poor accuracy) in order to exploit carrier phase accuracy with code tracking robustness to ambiguity.

4.2 Signal Acquisition

As described in [30], acquisition includes a search of the signal in the frequency domain and is responsible for identifying and separate all satellite signal existing in space. The quality of this search can greatly influence the quality and efficiency of the whole tracking and demodulation process. In case of slowly moving receivers, the acquisition process must search over $\pm$ 5 kHz of the expected Doppler frequency range resulting from the conjoint movement of the transmitter-receiver system. For receivers with large dynamics, such as aircraft or missile receivers, a frequency search over $\pm$ 10 kHz is often required [30]. The main problem of the acquisition search process is the balance between time efficiency and sensitivity since for a high sensitive process you need narrow frequency step increments which is time consuming.

One of the most common ways to start the acquisition is by calculating the visible satellites in a given point. By receiving Internet information or computing the satellite position with previously recorded almanac information based on current position and time, one can narrow the satellite search and so reducing the time spent on the initial acquisition. However, if the given time and position are wrongly supplied, the search can result in wrong satellite information.

Another method consists in searching all the satellites in space which is obviously a more time consuming and computing demanding effort that should be avoided (cold start condition).

Once the acquisition process captures a satellite signal, the signal information should be promptly sent

to the tracking hardware component of the receiver. Usually the receiver is working in real-time which means that the tracking system should receive on-time information to be functioning properly. Therefore, if the acquisition is slow, the tracking process may receive out-of-date information that can lead to loss of satellite tracking.

Consider that $s(t) = A[x(t) + jy(t)] \exp(j\omega_d t)$ is the baseband received signal with $x(t)$ and $y(t)$ denoting the inphase and quadrature spreading code signals multiplied by associated digital subcarriers and $f_d = \omega_d/(2\pi)$ is the Doppler frequency to be estimated.

In acquisition mode it is required to align the frequencies and code delays of $s(t)$ and a locally-generated version $\widetilde{s}(t) = [x(t-\tau_e)+jy(t-\tau_e)] \exp[j(\omega_d-\omega_e)t]$, where τ_e is the code synchronization error and $f_e = \omega_e/(2\pi)$ is the frequency synchronization error. Code and frequency alignment are achieved by maximizing the correlation of signals $\widetilde{s}(t)$ and $s(t)$ in the acquisition search plane corresponding to all allowed values of τ_e and f_e. An example of search plane is shown in fig. 4.4 for a spreading code with period equal to 10230 chips (as in the AltBOC signal) and a Doppler frequency range $[-5\,\mathrm{kHz},\ -5\,\mathrm{kHz}]$. Assuming that $x(t)$ and $y(t)$ are uncorrelated, the complex correlation of signals $s(t)$ and $\widetilde{s}(t)$ (also called Cross-Ambiguity Function (CAF)) is given by

$$\begin{aligned}
&\Xi(\tau_e,\, f_e) = \frac{1}{T}\int_0^T s(t)[\widetilde{s}(t)]^*\, dt \\
&\approx \frac{A}{T}\int_0^T [x(t)x(t-\tau_e) + y(t)y(t-\tau_e)] \cos(\omega_e t)\, dt \\
&+ j\frac{A}{T}\int_0^T [x(t)x(t-\tau_e) + y(t)y(t-\tau_e)] \sin(\omega_e t)\, dt
\end{aligned} \tag{4.5}$$

where T is the correlation interval (acquisition dwell time).

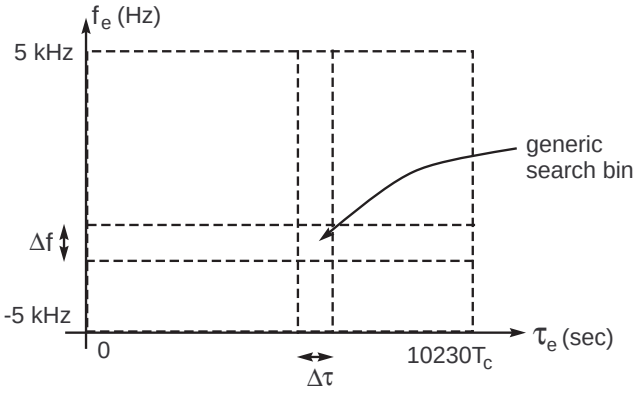

Figure 4.4: Example of synchronization search plane

A sufficient statistic for detecting the presence of a known signal with unknown amplitude and carrier phase, time delay, and frequency shift in white noise is the magnitude-squared of the CAF $|\Xi(\tau_e,\, f_e)|^2$ [24].

Two particular cases deserve special attention: (i) $\omega_e T \approx 0$, $|\tau_e| \gg 0$, and (ii) $|\omega_e T| \gg 0$, $\tau_e \approx 0$.

If $\omega_e T \approx 0$ the magnitude-squared of the CAF is simplified to

$$|\Xi(\tau_e,\, f_e)|^2 \approx A^2 |R_x(\tau_e) + R_y(\tau_e)|^2 \tag{4.6}$$

and will have a maximum at $\tau_e = 0$. The region of τ_e where the CAF is significantly different from zero depends on the autocorrelations $R_x(\tau_e)$ and $R_y(\tau_e)$. For instance, considering the AltBOC signal (where autocorrelations $R_x(\tau_e) = R_y(\tau_e)$ are depicted in fig. 3.7), the cross-ambiguity function for $\omega_e T \approx 0$ is sketched in fig. 4.5. The region of code delay errors where the correlation is much larger than zero is $-0.05\,T_c < \tau_e < 0.05\,T_c$. Therefore, the code bin width in the search plane should be typically $\Delta\tau \approx 0.1\,T_c$.

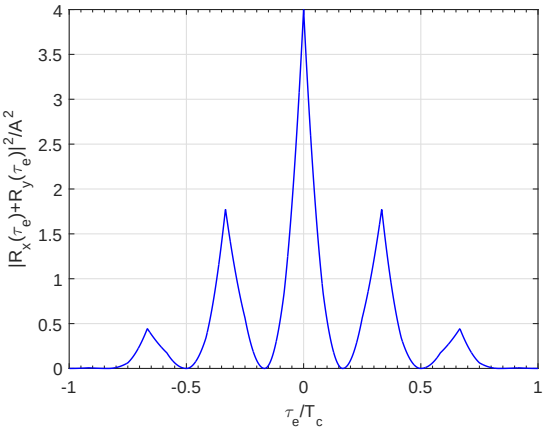

Figure 4.5: Normalized magnitude-squared CAF $|\Xi(\tau_e,\, f_e)|^2/A^2$ for $\omega_e T \approx 0$

Alternatively, if $\tau_e \approx 0$, and assuming for simplicity that $x^2(t) + y^2(t) = 1$, then

$$|\Xi(\tau_e,\, f_e)|^2 \approx A^2\,\mathrm{sinc}^2(f_e T) \tag{4.7}$$

In this case there will be a correlation maximum at $f_e = 0$. The region of frequency errors where the correlation is much larger than zero is $-1/(2T) < f_e < 1/(2T)$, as illustrated in fig. 4.6. Thus, the Doppler bin width of the search plane should be typically $\Delta f \approx 1/T$.

In short; results (4.6) and (4.7) mean that there will be a global correlation maximum when the locally-generated codes are perfectly aligned with the codes of the incoming signal and the frequency of $\widetilde{s}(t)$ coincides with the Doppler frequency of $s(t)$. As a consequence of the Doppler and code bin widths, the total number of search bins (cells) to be tested in the search plane amounts to

$$\frac{10230\,T_c}{\Delta\tau} \times \frac{10\,\mathrm{kHz}}{\Delta f} = 1.023 \times 10^9\,T\,\mathrm{cells} \tag{4.8}$$

Even for a small correlation interval T of 1 ms this result yields 1.023×10^6 cells, which makes the acquisition process for AltBOC signals an intolerable time-consuming task, especially if the search is made sequentially (serial search). When compared with a similar acquisition procedure for GPS C/A signals, the computational burden is aggravated by about sixty times as the number of chips of the primary code in AltBOC is ten times bigger and the main lobe of the magnitude-squared CAF for $\omega_e T \approx 0$

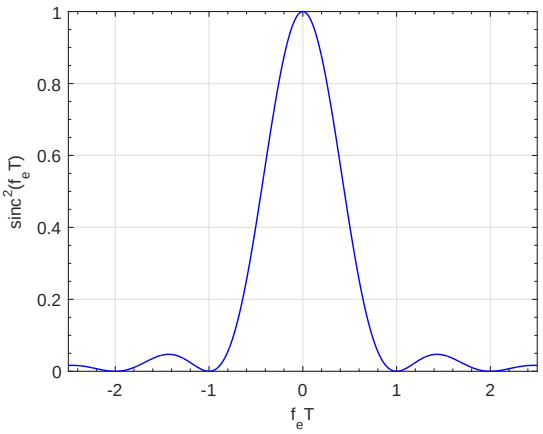

Figure 4.6: Normalized magnitude-squared CAF $|\Xi(\tau_e,\, f_e)|^2/A^2$ for $\tau_e \approx 0$

(see fig. 4.5) decays some six times faster than in the GPS signal. Modern receivers usually resort to different techniques to significantly accelerate the acquisition process, such as parallel time search often implemented using an Fast Fourier Transform (FFT) [24].

4.3 Signal Tracking

Signal tracking consists on following a satellite signal by constantly aligning a local signal replica with the received signal. The objective of the tracking process is finding the Doppler frequency associated with the receiver-transmitter relative movement and code delay resulting from the distance traveled by the signal. In order to synchronize the replicated signal code sequence (generated locally in the receiver) and the incoming satellite signal, a Phase Locked Loop (PLL) and a Delay Locked Loop (DLL) are used simultaneously to produce usable correction factors of Doppler frequency and code delay that are components of the resolution of the navigation equation system. In figure 4.7, one can visualize the superposition of the DLL and PLL for a conventional GPS receiver.

As shown in the figure, the tracking architecture is mainly composed by Inphase (I) and Quadrature (Q) correlators of Early (E), Late (L) and Prompt (P) versions of locally generated signal replicas combined with the received signal. In modern receivers the block diagram of fig. 4.7 is implemented using sampled signals, thus, the integrate-and-dump circuits are replaced by accumulators.

4.3.1 PLL

The chain of the PLL is composed by the inphase (I) and quadrature (Q) of the Prompt correlators (P) resulting in the in phase (I_P) and quadrature (Q_P) outputs given by:

$$\begin{aligned} I_P &= A_X d_X R_X(\tau_e)\cos(\phi_e) \\ Q_P &= -A_X d_X R_X(\tau_e)\sin(\phi_e) \end{aligned} \tag{4.9}$$

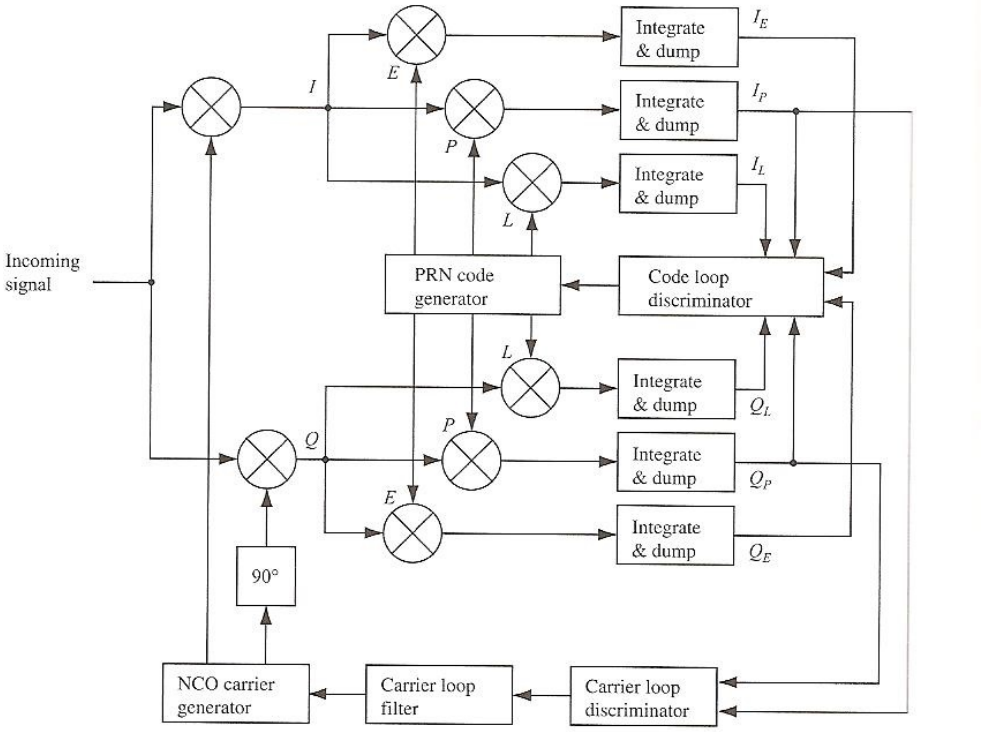

Figure 4.7: The block diagram of a complete tracking channel on the GPS receiver [31]

where:

- R_X is the autocorrelation of the X PRN code
- τ_e is the error of the code delay estimated at the receiver
- ϕ_e is the error of the carrier phase estimated at the receiver
- $d = \pm 1$ is the navigation message
- A_X is the amplitude

The most used PLL discriminators are [31], [32]:

- Sensitive to data bits:

$$D(\phi_e) = \text{atan2}(Q_P, I_P) \tag{4.10}$$

which is optimal, but presents a high computational burden. In (4.10), atan2 is the four-quadrant arctangent function defined in terms of the two-quadrant arctangent as

$$\text{atan2}(y,x) = \begin{cases} \text{atan}(y/x), & x > 0 \\ \text{atan}(y/x) + \pi, & y \geq 0, x < 0 \\ \text{atan}(y/x) - \pi, & y < 0, x < 0 \\ \pi/2, & y > 0, x = 0 \\ -\pi/2, & y < 0, x = 0 \\ \text{undefined}, & x = y = 0 \end{cases} \tag{4.11}$$

In order to use such discriminator, the receiver must ensure that the inputs do not include unknown data bits as in the case of the pilot channels of modern GNSS modulations.

- Insensitive to data bits, also called Costas loop:

$$\begin{aligned} D(\phi_e) &= \text{atan}\left(\frac{Q_P}{I_P}\right) \\ D(\phi_e) &= \text{sign}(I_P).Q_P \\ D(\phi_e) &= I_P.Q_P \end{aligned} \tag{4.12}$$

The choice of the discriminator is a trade-off between performance of the closed loop and required hardware resources, as well as complexity.

Exact characterization of the PLL or the Costas loop performance is complicated even in the absence of noise. However, when errors are small relative to the linear region of the discriminator response (S-curve), the mean-squared loop error can be expressed by [32], [24]:

$$\sigma^2 = \sigma^2_{\text{noise+interf}} + \sigma^2_{phasenoise} + (\Delta\theta)^2, \, (rad^2) \tag{4.13}$$

where $\sigma^2_{\text{noise+interf}}$ is the variance due to noise and interference, $\sigma^2_{phasenoise}$ is the variance due to phase noise in the receiver oscillator and $(\Delta\theta)$ is the change in carrier phase during a loop update due to the receiver dynamics along the line of sight relative to the satellite transmitting signal.
The variance of the loop jitter due to noise and interference in rad^2 is approximately [23]:

$$\sigma^2_{\text{noise+interf}} \approx \begin{cases} \frac{B_L}{\xi(\frac{C}{N_0})_{\text{eff}}} & \text{PLL} \\ \frac{B_L}{\xi(\frac{C}{N_0})_{\text{eff}}}[1 + \frac{1}{2T\xi(\frac{C}{N_0})_{\text{eff}}}] & \text{Costas Loop} \end{cases} \tag{4.14}$$

where B_L is the closed loop bandwidth in Hz, ξ is the fraction of total signal power in the component being tracked, $(C/N_0)_{\text{eff}}$ is the effective carrier power to noise PSD ratio for the entire signal and T is the correlation integration time and loop update time. When the correlator output SNR is large enough, the Costas loop and the PLL exhibit approximately the same variance due to noise and interference. In that case, the value of T becomes irrelevant for both types of loop.
A rule of thumb for the PLL to stay in lock is $\sigma < \pi/6$. The same rule applied to the Costas loop implies that $\sigma < \pi/12$ [32]

4.3.2 DLL

The chain of the DLL is composed by four or six correlators that process the in phase (I) and quadrature (Q) components of the received signal. The outputs of the Early (E) and Late (L) correlators are delayed or advanced replicas of the Prompt (P) correlator output, resulting in the in phase (I_E and I_L) and quadrature (Q_E and Q_P) outputs given by:

$$\begin{aligned} I_E &= Ad_X R_X\left(\tau_e - \frac{\Delta}{2}\right)\cos(\phi_e) \\ Q_E &= -Ad_X R_X\left(\tau_e - \frac{\Delta}{2}\right)\sin(\phi_e) \\ I_L &= Ad_X R_X\left(\tau_e + \frac{\Delta}{2}\right)\cos(\phi_e) \\ Q_L &= -Ad_X R_X\left(\tau_e + \frac{\Delta}{2}\right)\sin(\phi_e) \end{aligned} \tag{4.15}$$

where the variables are the same as described in the PLL with some differences:

- E,L stands for *Early* and *Late* replica respectively
- Δ is the Early-Late spacing

The most used DLL discriminators are:

- Non-coherent Early minus Late Power (NELP):

$$\begin{aligned} D(\tau_e) &= (I_E^2 + Q_E^2) - (I_L^2 + Q_L^2) \\ &= A^2\left[R_X^2\left(\tau_e - \frac{\Delta}{2}\right) - R_X^2(\tau_e + \frac{\Delta}{2})\right] \end{aligned} \tag{4.16}$$

  where is assumed that $d_X = \pm 1$.

- Dot Product:

$$\begin{aligned} D(\tau_e) &= (I_E - I_L)I_P + (Q_E - Q_L)Q_P \\ &= A^2\left[R_X\left(\tau_e - \frac{\Delta}{2}\right) - R_X(\tau_e + \frac{\Delta}{2})\right]R_X(\tau_e) \end{aligned} \tag{4.17}$$

  is a quasi-coherent dot product power discriminator. Whenever the PLL is locked ($\phi_e \approx 0$), the following coherent dot product can be used, with lower computational burden:

$$D(\tau_e) = (I_E - I_L)I_P \tag{4.18}$$

Figure 4.8 displays the non normalized response $D(\tau_e)/A^2$ of the NELP and the dot product discriminators for the AltBOC(15,10) signal with early-late spacing $\Delta = 0.2T_c$.

The figure shows that the equilibrium points of the discriminator ($D(\tau_e) = 0$ and positive slope) are $\tau_e = 0$ (desirable solution), $\tau_e = \pm 0.325T_c$ and $\tau_e = \pm 0.65T_c$. These last four solutions are undesirable

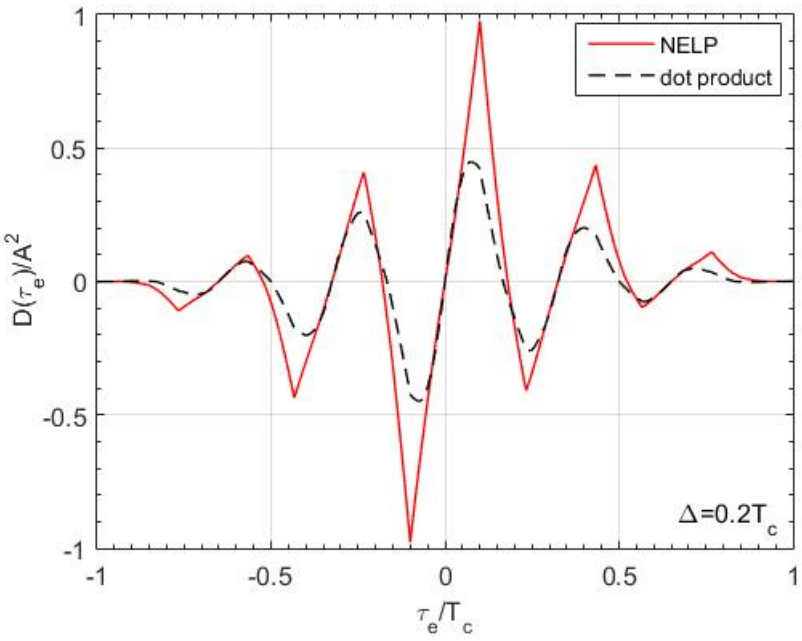

Figure 4.8: Non normalized response of the NELP and dot product code discriminators for the Alt-BOC(15,10) signal with $\Delta = 0.2T_c$

as they produce false code-locks. Algorithms, like the bump-jumping, may be used to minimize this problem [33].

4.3.3 Data Demodulation

Once the PLL or Costas Loop is locked, the navigation bits can be recovered from the I_P correlator output in (4.9). In that case

$$\begin{aligned} I_P &\approx A_X d_X \\ Q_P &\approx 0 \end{aligned} \tag{4.19}$$

and the detected bit is $d_X = 1$, if $I_P > 0$ and $d_X = -1$ otherwise. For uncoded data bits modulated onto the signal using coherent binary phase-shift keying (BPSK), the bit error probability is given by [24]

$$P_b = Q\left(\sqrt{2\left(\frac{E_b}{N_o}\right)_{\text{eff}}}\right) \tag{4.20}$$

where E_b is the bit energy,

$$\left(\frac{E_b}{N_0}\right)_{\text{eff}} = \xi T_b \left(\frac{C}{N_0}\right)_{\text{eff}} \tag{4.21}$$

with T_b denoting the bit duration and

$$Q(x) = \frac{1}{\sqrt{2\pi}} \int_x^\infty \exp\left(-\frac{t^2}{2}\right) dt \tag{4.22}$$

is the complementary error function. Formula (4.20) assumes that no forward error correction (FEC) scheme is available. Current GNSS apply some form of FEC to minimize the probability of bit error. For instance, GPS C/A signal uses a (32,26) Hamming code [32].
The GALILEO system uses convolutional encoding for all data pages on all signal components with coding rate 1/2 and constraint length equal to 7 [13].

4.4 Noise Performance

Code tracking errors caused by additive white Gaussian noise (AWGN) can be predicted analytically as long as the errors are small enough to stay in the linear portion of the S-curve (code discriminator response). By modeling the pre-correlation filter as an ideal rectangular bandpass filter with bandwidth B yields the following variance of the code tracking error for the coherent early-late power (CELP) discriminator [34]

$$\sigma^2_{\mathrm{CELP}} = \frac{c^2 B_L \int_{-B/2}^{B/2} G_s(f) \sin^2(\pi f \Delta)\, df}{(2\pi)^2 \xi \left(\frac{C}{N_0}\right) \left[\int_{-B/2}^{B/2} f G_s(f) \sin(\pi f \Delta)\, df\right]^2} \tag{4.23}$$

where c is the speed of light, B_L is the bandwidth of the code tracking loop (DLL), ξ is the fraction of the total power in the component being tracked, $G_s(f)$ is the normalized PSD (unit area) of the component being tracked, Δ is the early-late spacing, and (C/N_0) is the carrier to noise power spectral density ratio.

For NELP discriminators, the corresponding expression is a scaled version of the variance for the CELP [34]

$$\sigma^2_{\mathrm{NELP}} = \sigma^2_{\mathrm{CELP}} \left[1 + \frac{\int_{-B/2}^{B/2} G_s(f) \cos^2(\pi f \Delta)\, df}{T\xi \left(\frac{C}{N_0}\right) \left[\int_{-B/2}^{B/2} G_s(f) \cos(\pi f \Delta)\, df\right]^2}\right] \tag{4.24}$$

with T denoting the correlation interval.

In general, the linear region of the S-curve corresponds to code tracking errors with time magnitude less than $\Delta/2$. A simple approximate rule of thumb for a code tracking loop-lock criterion is [24]

$$\sigma_{\mathrm{code}} < \frac{c\Delta}{12} \tag{4.25}$$

where σ_{code} is the standard deviation of the code tracking error from all sources root-squared together, including dynamic stress as well as jitter induced by noise and interference.

Next the performances of the following modulations are compared: $\mathrm{BPSK-R}(1)$, which is used in the GPS legacy signal C/A, $\mathrm{BOCs}(1,1)$, which is approximately the modulation that results from filtering the CBOC signals in low-cost receivers, the CBOCpilot modulation, and finally, the AltBOC(15,10) modulation.

The normalized PSD of the BPSK-R(n) signals is given by [24]

$$G_{\mathrm{BPSK-R(n)}}(f) = T_c \,\mathrm{sinc}^2(fT_c) \tag{4.26}$$

The normalized PSD of the BOCs(p,1) signals is given by [26]

$$G_{\mathrm{BOCs(p,1)}}(f) = T_c \,\mathrm{sinc}^2(fT_c) \tan^2\left(\frac{\pi f T_c}{2p}\right), \quad p = 1, 2, \ldots \tag{4.27}$$

The normalized PSD of the CBOCpilot signal is given by [26]

$$G_{\mathrm{CBOCpilot}}(f) = \frac{10}{11} G_{\mathrm{BOCs(1,1)}}(f) + \frac{1}{11} G_{\mathrm{BOCs(6,1)}}(f) - 2\frac{\sqrt{10}}{11} G_{12}(f) \tag{4.28}$$

with

$$G_{12}(f) = \frac{T_c}{36} \,\mathrm{sinc}^2\left(\frac{fT_c}{12}\right) \frac{\sin^2(\pi f T_c/2)\sin(\pi f T_c)}{\sin(\pi f T_c/6)} \tag{4.29}$$

Finally, the normalized PSD of the AltBOC(15,10) signal is given by [26]

$$G_{\mathrm{AltBOC(s)}}(f) = \frac{T_c \cos^2(\pi f T_c)}{72\cos(\pi f T_c/3)} \left[\frac{4\,\mathrm{sinc}^2(fT_c/6)}{\cos(\pi f T_c/3)} - \mathrm{sinc}^2(fT_c/12)\cos(\pi f T_c/6)\right] \tag{4.30}$$

Figure 4.9 shows NELP code tracking errors for different spreading modulations with tracking loop bandwidth $B_L = 1$ Hz, early-late spacing $\Delta = 0.1T_c$ and correlation interval equal to $T = 5$ ms. The error curves present infinite slope at the point where the loop-lock criterion (4.25) stops being satisfied. Two different RF bandwidths were used: $B = 50$ MHz and $B = 30$ MHz. Note that the smaller bandwidth is enough for BPSK-R(1), BOCs(1,1) and CBOCpilot but is clearly insufficient for the AltBOC modulation. This agrees with the conclusion obtained in Chapter III which says that a pre-detection bandwidth of approximately 50 MHz is required for correct operation of the AltBOC receiver.

4.5 Multipath

Multipath is interference from delayed versions of a signal that are received in addition to the same signal arriving directly from the transmitter. The delayed versions are caused by reflections or diffractions in the propagation channel. Multipath-induced errors can often be the largest source of error in the solution of the navigation equation and are typically the dominant errors in differential satellite navigation [24].

Assume that the incoming signal consists of a Line-Of-Sight (LOS) or direct signal with amplitude A and a reflected signal with amplitude αA, delay τ and phase ϕ relative to the LOS. The receiver's input (neglecting the contribution of noise) is given by

$$r(t) = AX(t)\cos(\omega_0 t + \theta) + \alpha A X(t-\tau)\cos(\omega_0 t + \theta + \phi) \tag{4.31}$$

where $X(t)$ is a baseband process that includes spreading code, digital sub-carrier and navigation bits, and $0 < \alpha < 1$ stands for the relative amplitude of the reflected ray. Consider that inphase/quadrature, early/late correlators are $I_E(\epsilon)$, $Q_E(\epsilon)$, $I_L(\epsilon)$ and $Q_L(\epsilon)$, with ϵ denoting the DLL code delay error, such

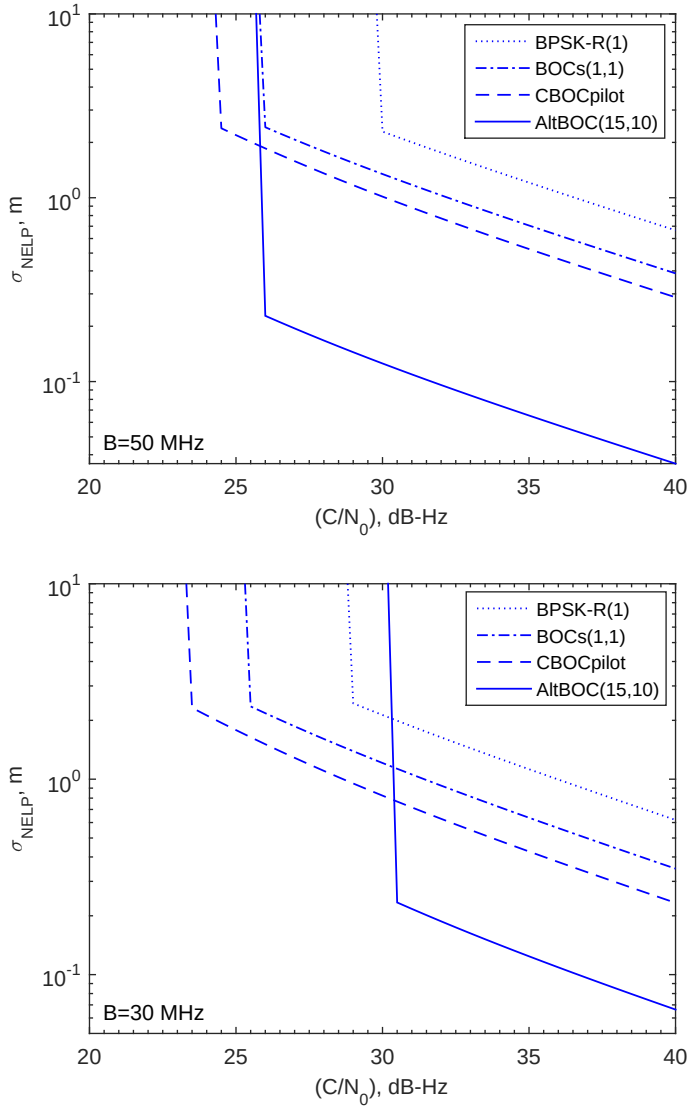

Figure 4.9: NELP code tracking errors due to noise for RF bandwidths of 50 and 30 MHz

that

$$\begin{bmatrix} I_E(\epsilon) \\ Q_E(\epsilon) \end{bmatrix} = A\,R_X\left(\epsilon - \frac{\Delta}{2}\right)\begin{bmatrix} \cos\theta \\ \sin\theta \end{bmatrix} + \alpha A\,R_X\left(\epsilon - \tau - \frac{\Delta}{2}\right)\begin{bmatrix} \cos(\theta+\phi) \\ \sin(\theta+\phi) \end{bmatrix} \tag{4.32}$$

and

$$\begin{bmatrix} I_L(\epsilon) \\ Q_L(\epsilon) \end{bmatrix} = A\,R_X\left(\epsilon + \frac{\Delta}{2}\right)\begin{bmatrix} \cos\theta \\ \sin\theta \end{bmatrix} + \alpha A\,R_X\left(\epsilon - \tau + \frac{\Delta}{2}\right)\begin{bmatrix} \cos(\theta+\phi) \\ \sin(\theta+\phi) \end{bmatrix} \tag{4.33}$$

The NELP discriminator response is

$$
\begin{aligned}
D(\epsilon,\tau,\phi) \;=\; & A^2R_X^2(\epsilon-\Delta/2)+A^2\alpha^2R_X^2(\epsilon-\tau-\Delta/2) \\
+\; & 2A^2\alpha R_X(\epsilon-\Delta/2)R_X(\epsilon-\tau-\Delta/2)\cos\phi \\
-\; & A^2R_X^2(\epsilon+\Delta/2)-A^2\alpha^2R_X^2(\epsilon-\tau+\Delta/2) \\
-\; & 2A^2\alpha R_X(\epsilon+\Delta/2)R_X(\epsilon-\tau+\Delta/2)\cos\phi
\end{aligned}
\tag{4.34}
$$

The multipath error envelopes result from solving the following equations for ϵ

$$
\text{(i)}\quad D(\epsilon,\tau,0)=0; \qquad \text{(ii)}\quad D(\epsilon,\tau,\pi)=0 \tag{4.35}
$$

which corresponds to the reflected ray being in phase ($\phi=0$) or in phase opposition ($\phi=\pi$) relative to the LOS. Equation (i) leads to

$$
R_X(\epsilon-\Delta/2)+\alpha R_X(\epsilon-\tau-\Delta/2)=\pm\left[R_X(\epsilon+\Delta/2)+\alpha R_X(\epsilon-\tau+\Delta/2)\right] \tag{4.36}
$$

and equation (ii) yields

$$
R_X(\epsilon-\Delta/2)-\alpha R_X(\epsilon-\tau-\Delta/2)=\pm\left[R_X(\epsilon+\Delta/2)-\alpha R_X(\epsilon-\tau+\Delta/2)\right] \tag{4.37}
$$

In the two previous equations, only the sign "+" in the right member is valid. In fact, doing $\alpha=0$, we obtain $R_X(\epsilon-\Delta/2)=\pm R_X(\epsilon+\Delta/2)$ whose solution is $\epsilon=0$; thus, only sign "+" is valid.

Merging the two equations leads to the solution for the multipath error envelopes

$$
R_X\left(\epsilon-\frac{\Delta}{2}\right)-R_X\left(\epsilon+\frac{\Delta}{2}\right)=\pm\alpha\left[R_X\left(\epsilon-\tau-\frac{\Delta}{2}\right)-R_X\left(\epsilon-\tau+\frac{\Delta}{2}\right)\right] \tag{4.38}
$$

Figure 4.10 sketches the multipath error envelopes (in meters) for $\alpha=0.5$, $\Delta=0.1T_c$ and several modulations whose autocorrelation functions are indicated in Appendix A. Note that, in general, the DLL is immune to relative delays of the secondary ray above approximately T_c, which corresponds to extra distances of 293.26 m, except for the AltBOC signal, which is 29.33 m. The figure shows that the tracking errors of the DLL are large for GPS C/A signals and decrease for BOC(1,1), CBOC pilot and especially for the AltBOC(15,10). The good performance in the presence of multipath, namely the small tracking errors and the reduced range of delays that lead to multipath errors, constitutes one of the major advantages of AltBOC regarding the other modulations.

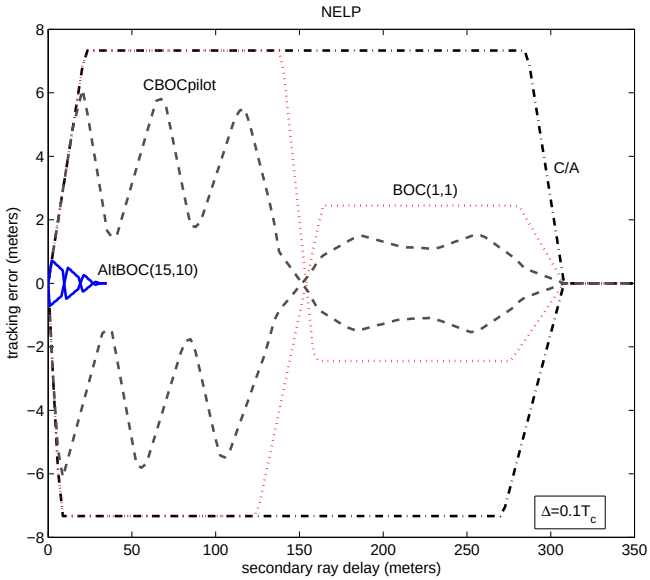

Figure 4.10: Multipath error envelopes for several signals using the NELP code discriminator with infinite bandwidth and α =0.5

Chapter 5

Receiver architectures for AltBOC signals

This chapter presents and analyzes two architectures for baseband tracking of AltBOC signals using one sub-band of E5 (single sideband processing) or the whole signal (double sideband processing). Section 1 discusses the advantages/drawbacks of the different architectures. Section 2 determines the simplifications that can be obtained by filtering the AltBOC signals. This aspect is important as the receiver front-end uses some type of passband filtering to minimize the effect of noise. Section 3 analyzes a structure for single sideband processing (sub-bands A or B). Finally, Section 4 analyzes a structure for double sideband processing (sub-bands A plus B).

5.1 Introduction

Due to the complexity of the AltBOC signal the receiver may use one of the following four options for processing the signal [10], [24]:

- Process the entire E5 signal as a wideband 8-phase signal;
- Process both E5a and E5b separately;
- Process only the E5a component;
- Process only the E5b component.

All these options present advantages and drawbacks. The typical front-end filter bandwidth for a receiver that processes the whole signal is 51.15 MHz [13]. Using the entire E5 signal provides benefits of accessing all the signal power including use of the GNSS signal with the widest bandwidth with opportunities to minimize the multipath effect and reduce the code tracking errors. However, the use of a large fractional bandwidth, typically defined as the null-to-null bandwidth divided by the center frequency, implies the risk of having significant different Doppler effects over the signal bandwidth, potentially limiting integration times if significant satellite-to-receiver dynamics is expected. Dispersive effects due to

the ionosphere may be also a limiting factor and dispersion due to the receiver front-end hardware must be taken into account, possibly requiring more expensive hardware. The wide bandwidth receiver and associated high sampling rate tend to increase the power consumption of the front-end and the digital processing blocks.

Initial synchronization (code and Doppler acquisition) of the entire wideband signal would be complicated. Thus, initial synchronization could be performed using sideband processing because of the narrow correlation function with wideband processing [24]. The topic of acquisition with AltBOC signals is complex (see, for instance, the analysis performed in [10]) and is outside the scope of this work. The rest of the thesis will address only the problem of code and carrier tracking.

Coherent processing the signals E5a and E5b separately and combining the measurements is a compromise in terms of benefits and implementation complexity, but still makes use of the entire signal. Processing only the E5a or E5b signal reduces implementation to that of a BPSK-R(10) signal but neglects more than half the signal power.

5.2 Filtered AltBOC signals

The baseband AltBOC signal was defined in (3.2) and is repeated here for convenience

$$\begin{aligned} s_{E5}(t) &= \frac{1}{2\sqrt{2}}[e_{E5a-I}(t)+je_{E5a-Q}(t)][sc_{E5-S}(t)-jsc_{E5-S}(t-T_s/4)] \\ &+ \frac{1}{2\sqrt{2}}[e_{E5b-I}(t)+je_{E5b-Q}(t)][sc_{E5-S}(t)+jsc_{E5-S}(t-T_s/4)] \\ &+ \frac{1}{2\sqrt{2}}[\overline{e}_{E5a-I}(t)+j\overline{e}_{E5a-Q}(t)][sc_{E5-P}(t)-jsc_{E5-P}(t-T_s/4)] \\ &+ \frac{1}{2\sqrt{2}}[\overline{e}_{E5b-I}(t)+j\overline{e}_{E5b-Q}(t)][sc_{E5-P}(t)+jsc_{E5-P}(t-T_s/4)] \end{aligned} \tag{5.1}$$

with T_s denoting the period of subcarrier $sc_{E5-S}(t)$. The dashed signal components take the values ± 1 being given by

$$\overline{e}_{E5a-I} = e_{E5a-Q}\cdot e_{E5b-I}\cdot e_{E5b-Q} \tag{5.2}$$

$$\overline{e}_{E5b-I} = e_{E5b-Q}\cdot e_{E5a-I}\cdot e_{E5a-Q} \tag{5.3}$$

$$\overline{e}_{E5a-Q} = e_{E5a-I}\cdot e_{E5b-I}\cdot e_{E5b-Q} \tag{5.4}$$

$$\overline{e}_{E5b-Q} = e_{E5b-I}\cdot e_{E5a-I}\cdot e_{E5a-Q} \tag{5.5}$$

These terms, contained in the last two lines of (5.1), can be neglected because they correspond to the so-called product signals and do not carry useful information [9].

Define now the following signals

$$\alpha(t) \equiv e_{E5a-I}(t) + e_{E5b-I}(t) \tag{5.6}$$

$$\beta(t) \equiv e_{E5a-Q}(t) - e_{E5b-Q}(t) \tag{5.7}$$

$$\gamma(t) \equiv e_{E5a-Q}(t) + e_{E5b-Q}(t) \tag{5.8}$$

$$\mu(t) \equiv e_{E5b-I}(t) - e_{E5a-I}(t) \tag{5.9}$$

The real and imaginary parts of $s_{E5}(t)$ are well approximated by

$$\mathrm{Re}\{s_{E5}(t)\} \approx \frac{1}{2\sqrt{2}}\Big[\alpha(t)\, sc_{E5-S}(t) + \beta(t)\, sc_{E5-S}(t - T_s/4)\Big] \tag{5.10}$$

and

$$\mathrm{Im}\{s_{E5}(t)\} \approx \frac{1}{2\sqrt{2}}\Big[\gamma(t)\, sc_{E5-S}(t) + \mu(t)\, sc_{E5-S}(t - T_s/4)\Big] \tag{5.11}$$

The autocorrelation function of signal $s_{E5}(t) = \mathrm{Re}\{s_{E5}(t)\} + j\mathrm{Im}\{s_{E5}(t)\}$, with the real and imaginary parts given by (5.10) and (5.11), is equal to

$$\begin{aligned} R_{E5}(\tau) &= \frac{1}{T_s}\int_0^{T_s} E\{s_{E5}(t)s^*_{E5}(t-\tau)\}\, dt \\ &= R_c(\tau)R_{sc}(\tau) \end{aligned} \tag{5.12}$$

where $R_c(\tau)$ is the code autocorrelation given by

$$R_c(\tau) = \Lambda\left(\frac{\tau}{T_c}\right) \equiv \begin{cases} 1 - \frac{|\tau|}{T_c}, & |\tau| < T_c \\ 0, & \text{otherwise} \end{cases} \tag{5.13}$$

and the autocorrelation of subcarrier $sc_{E5-S}(t)$ is periodic with

$$R_{sc}(\tau) = \frac{1}{T_s}\int_0^{T_s} sc_{E5-S}(t)sc_{E5-S}(t-\tau)\, dt \tag{5.14}$$

which is displayed in fig. 5.1.

The subcarrier $sc_{E5-S}(t)$ is approximately a cosine function, as discussed in Appendix B. Besides the spectral line at frequency $f_s = 15.3545$ MHz the second line occurs only at frequency $7f_s = 107.415$ MHz. Thus, with a mild amount of filtering the inphase and quadrature subcarriers are well approximated by (see appendix B)

$$sc_{E5-S}(t) \approx \frac{4}{\pi}\cos(2\pi f_s t) \tag{5.15}$$

$$sc_{E5-S}(t - T_s/4) \approx \frac{4}{\pi}\sin(2\pi f_s t) \tag{5.16}$$

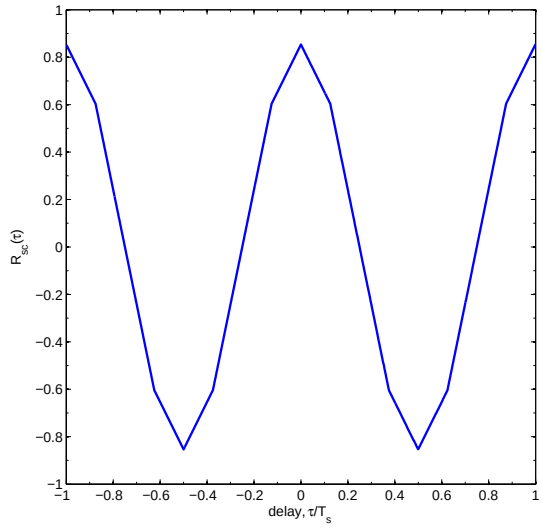

Figure 5.1: Subcarrier $sc_{E5-s}(t)$ autocorrelation function

Taking into account that the subcarrier $sc_{E5}(t)$ can be expanded in complex Fourier series with coefficients c_k determined in Appendix B, the autocorrelation (5.14) is given by

$$\begin{aligned} R_{sc}(\tau) &= \frac{4}{T_s}\sum_{n=1}^{\infty}\sum_{k=1}^{\infty} c_k c_n \int_0^{T_s} \cos(2\pi n f_s t)\cos(2\pi k f_s (t-\tau))\,dt \\ &= 2\sum_{n=1}^{\infty} c_n^2 \cos(2\pi n f_s \tau) \\ &= \frac{1}{2}\sum_{n=1}^{\infty} \operatorname{sinc}^2\left(\frac{n}{2}\right)\left(1+\sqrt{2}\cos\left(\frac{\pi n}{4}\right)\right)^2 \cos(2\pi n f_s \tau) \end{aligned} \tag{5.17}$$

If the RF signal $s_{E5}(t)$ is filtered in a bandwidth slightly above 50 MHz, the real and imaginary parts of $s_{E5}(t)$ are well approximated by [2]

$$\begin{bmatrix} \mathrm{Re}\{s_{E5}(t)\} \\ \mathrm{Im}\{s_{E5}(t)\} \end{bmatrix} \approx \frac{\sqrt{2}}{\pi} \begin{bmatrix} \alpha(t) & \beta(t) \\ \gamma(t) & \mu(t) \end{bmatrix} \begin{bmatrix} \cos(\omega_s t) \\ \sin(\omega_s t) \end{bmatrix} \tag{5.18}$$

The autocorrelation function of signal $s_{E5}(t)$ is then well approximated by

$$R_{E5}(\tau) = \frac{8}{\pi^2} R_c(\tau)\cos(2\pi f_s \tau) \tag{5.19}$$

The exact plot of the autocorrelation of signal $s_{E5}(t)$ (which assumes unlimited bandwidth), given in (3.11), and the approximations given by (5.12) and (5.19) are displayed in fig. 5.2.

In the receiver we can track the complete E5 AltBOC signal or any component of that signal. The baseband resulting signal is correlated with a local generated signal which depends on the method utilized. To process the information contained in the whole band the receiver may use a 8-PSK-like processing which allows only the complete E5 signal correlation by the use of a look-up table. To process

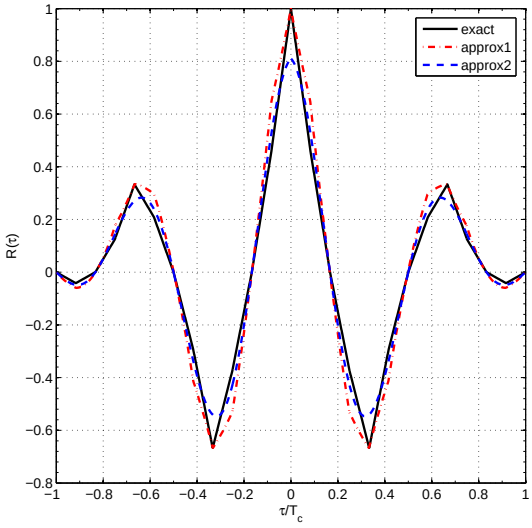

Figure 5.2: Exact and approximated plots of the autocorrelation function of signal $s_{E5}(t)$: approx1=eq. (5.12), approx2=eq. (5.19)

only the information of one of the sub-bands two methods may be devised. The first method in which E5a and E5b signals are translated from their center frequencies to the baseband is called the Side-Band Translation (SBT) method. The local signal is then generated free of subcarriers. The second method is the Full-Band Independent Correlation (FIC) in which the local signal is generated for the required signal component mapped onto the appropriate phase of the subcarrier. With both methods, several combinations are possible with the combination variables being coherent and non-coherent, data and pilot, E5a and E5b [35].

The effect of homodyning on the power spectra of the AltBOC signals using the methods 8-PSK, FIC and SBT is sketched in fig. 5.3.

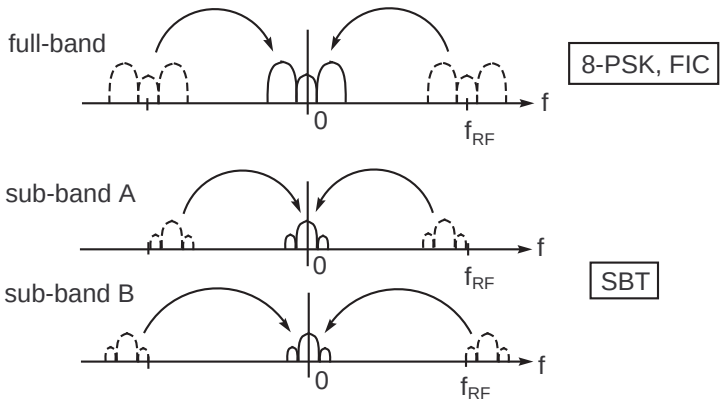

Figure 5.3: Power spectra translation due to homodyning using methods 8-PSK, FIC and SBT

5.3 Single-sideband AltBOC receiver (with baseband processing)

This method corresponds to translate the E5a and E5b signals from their center frequencies to the baseband and is known as Sideband Translation (SBT) [35]. Consider the RF AltBOC signal given by

$$r(t) = A[\mathrm{Re}\{s_{E5}(t)\}\cos(\omega_0 t + \phi) - \mathrm{Im}\{s_{E5}(t)\}\sin(\omega_0 t + \phi)] \tag{5.20}$$

where $\omega_0 = \omega_{RF} + \omega_d$ and ω_{RF} is the nominal carrier frequency. Assume for simplicity that the receiver tracks the sub-band E5a. The RF signal is heterodyned to baseband (homodyning) using the circuit of fig. 5.4.

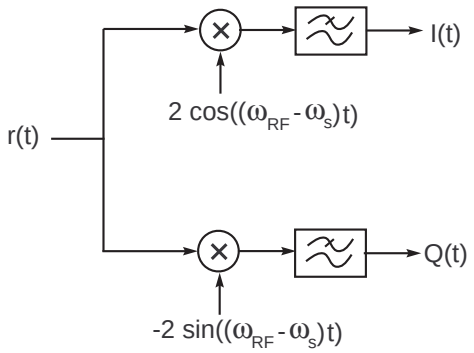

Figure 5.4: Block diagram for homodyning using the SBT method

The baseband components obtained after lowpass filtering, are given by

$$I(t) = \frac{A\sqrt{2}}{\pi}\Big[e_{E5a-I}(t)\cos(\omega_d t + \phi) - e_{E5a-Q}(t)\sin(\omega_d t + \phi)\Big] \tag{5.21}$$

$$Q(t) = \frac{A\sqrt{2}}{\pi}\Big[e_{E5a-I}(t)\sin(\omega_d t + \phi) + e_{E5a-Q}(t)\cos(\omega_d t + \phi)\Big] \tag{5.22}$$

5.3.1 PLL

The PLL multiplies the inphase and quadrature components $I(t)$ and $Q(t)$ by the locally-generated code (prompt) sequence $e_{E5a-Q}(t-\epsilon)$ to produce

$$IC_P(t) \equiv I(t)e_{E5a-Q}(t-\epsilon) \approx -\frac{A\sqrt{2}}{\pi}e_{E5a-Q}(t)e_{E5a-Q}(t-\epsilon)\sin(\omega_d t + \phi) \tag{5.23}$$

$$QC_P(t) \equiv Q(t)e_{E5a-Q}(t-\epsilon) \approx \frac{A\sqrt{2}}{\pi}e_{E5a-Q}(t)e_{E5a-Q}(t-\epsilon)\cos(\omega_d t + \phi) \tag{5.24}$$

Considering now the products

$$U_P(t) = IC_P(t)\sin(\widehat{\omega_d}t + \widehat{\phi}) \quad (5.25)$$

$$V_P(t) = QC_P(t)\cos(\widehat{\omega_d}t + \widehat{\phi}) \quad (5.26)$$

$$X_P(t) = IC_P(t)\cos(\widehat{\omega_d}t + \widehat{\phi}) \quad (5.27)$$

$$Y_P(t) = QC_P(t)\sin(\widehat{\omega_d}t + \widehat{\phi}) \quad (5.28)$$

we obtain

$$V_P(t) - U_P(t) = \frac{A\sqrt{2}}{\pi} e_{E5a-Q}(t) e_{E5a-Q}(t-\epsilon)\cos\phi_e \quad (5.29)$$

$$X_P(t) + Y_P(t) = \frac{A\sqrt{2}}{\pi} e_{E5a-Q}(t) e_{E5a-Q}(t-\epsilon)\sin\phi_e \quad (5.30)$$

By integrating leads to

$$\frac{1}{T}\int_0^T [V_P(t) - U_P(t)]\,dt = \frac{A\sqrt{2}}{\pi} R_c(\epsilon)\cos\phi_e \quad (5.31)$$

and

$$\frac{1}{T}\int_0^T [X_P(t) + Y_P(t)]\,dt = \frac{A\sqrt{2}}{\pi} R_c(\epsilon)\sin\phi_e \quad (5.32)$$

Thus, the response of the PLL discriminator is

$$\phi_e = \arctan 2\left(\frac{1}{T}\int_0^T [X_P(t) + Y_P(t)]\,dt,\ \frac{1}{T}\int_0^T [V_P(t) - U_P(t)]\,dt\right) \quad (5.33)$$

5.3.2 DLL

Consider the quantities

$$IC_E(t) \equiv I(t) e_{E5a-Q}(t - \epsilon + \Delta/2) \approx -\frac{A\sqrt{2}}{\pi} e_{E5a-Q}(t) e_{E5a-Q}(t - \epsilon + \Delta/2)\sin(\omega_d t + \phi) \quad (5.34)$$

$$QC_E(t) \equiv Q(t) e_{E5a-Q}(t - \epsilon + \Delta/2) \approx \frac{A\sqrt{2}}{\pi} e_{E5a-Q}(t) e_{E5a-Q}(t - \epsilon + \Delta/2)\cos(\omega_d t + \phi) \quad (5.35)$$

and

$$IC_L(t) \equiv I(t) e_{E5a-Q}(t - \epsilon - \Delta/2) \approx -\frac{A\sqrt{2}}{\pi} e_{E5a-Q}(t) e_{E5a-Q}(t - \epsilon - \Delta/2)\sin(\omega_d t + \phi) \quad (5.36)$$

$$QC_L(t) \equiv Q(t) e_{E5a-Q}(t - \epsilon - \Delta/2) \approx \frac{A\sqrt{2}}{\pi} e_{E5a-Q}(t) e_{E5a-Q}(t - \epsilon - \Delta/2)\cos(\omega_d t + \phi) \quad (5.37)$$

Consider now the products

$$U_E(t) = IC_E(t)\sin(\widehat{\omega_d}t + \widehat{\phi}) \tag{5.38}$$

$$V_E(t) = QC_E(t)\cos(\widehat{\omega_d}t + \widehat{\phi}) \tag{5.39}$$

$$X_E(t) = IC_E(t)\cos(\widehat{\omega_d}t + \widehat{\phi}) \tag{5.40}$$

$$Y_E(t) = QC_E(t)\sin(\widehat{\omega_d}t + \widehat{\phi}) \tag{5.41}$$

$$U_L(t) = IC_L(t)\sin(\widehat{\omega_d}t + \widehat{\phi}) \tag{5.42}$$

$$V_L(t) = QC_L(t)\cos(\widehat{\omega_d}t + \widehat{\phi}) \tag{5.43}$$

$$X_L(t) = IC_L(t)\cos(\widehat{\omega_d}t + \widehat{\phi}) \tag{5.44}$$

$$Y_L(t) = QC_L(t)\sin(\widehat{\omega_d}t + \widehat{\phi}) \tag{5.45}$$

By integrating leads to

$$I_E \equiv \frac{1}{T}\int_0^T [V_E(t) - U_E(t)]\,dt = \frac{A\sqrt{2}}{\pi}R_c(\epsilon - \Delta/2)\cos\phi_e \tag{5.46}$$

$$Q_E \equiv \frac{1}{T}\int_0^T [X_E(t) + Y_E(t)]\,dt = \frac{A\sqrt{2}}{\pi}R_c(\epsilon - \Delta/2)\sin\phi_e \tag{5.47}$$

$$I_L \equiv \frac{1}{T}\int_0^T [V_L(t) - U_L(t)]\,dt = \frac{A\sqrt{2}}{\pi}R_c(\epsilon + \Delta/2)\cos\phi_e \tag{5.48}$$

$$Q_L \equiv \frac{1}{T}\int_0^T [X_L(t) + Y_L(t)]\,dt = \frac{A\sqrt{2}}{\pi}R_c(\epsilon + \Delta/2)\sin\phi_e \tag{5.49}$$

The response of the NELP discriminator is then given by

$$\begin{aligned} D_{NELP}(\epsilon) &= (I_E^2 + Q_E^2) - (I_L^2 + Q_L^2) \\ &= \frac{2A^2}{\pi^2}\left[\Lambda^2\left(\frac{\epsilon - \Delta/2}{T_c}\right) - \Lambda^2\left(\frac{\epsilon + \Delta/2}{T_c}\right)\right] \end{aligned} \tag{5.50}$$

Notice that for this receiver architecture tracks signals with BPSK(10) modulation.

5.4 Double-sideband AltBOC receiver

The coherent reception and processing of the entire Galileo E5 band utilizes the 8-PSK method with the homodyning operation being performed by the block diagram of fig. 5.5. In [9], an AltBOC receiver based on the 8-PSK method was proposed (see fig. 5.6). This receiver will be herein analyzed.

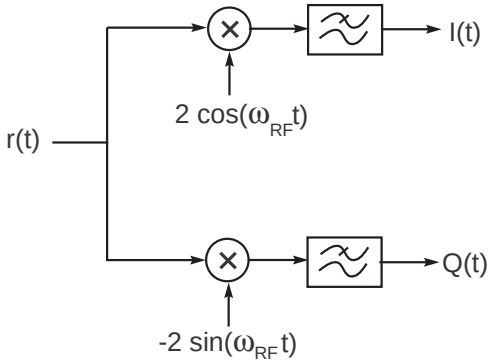

Figure 5.5: Block diagram for homodyning using the 8-PSK or FIC methods

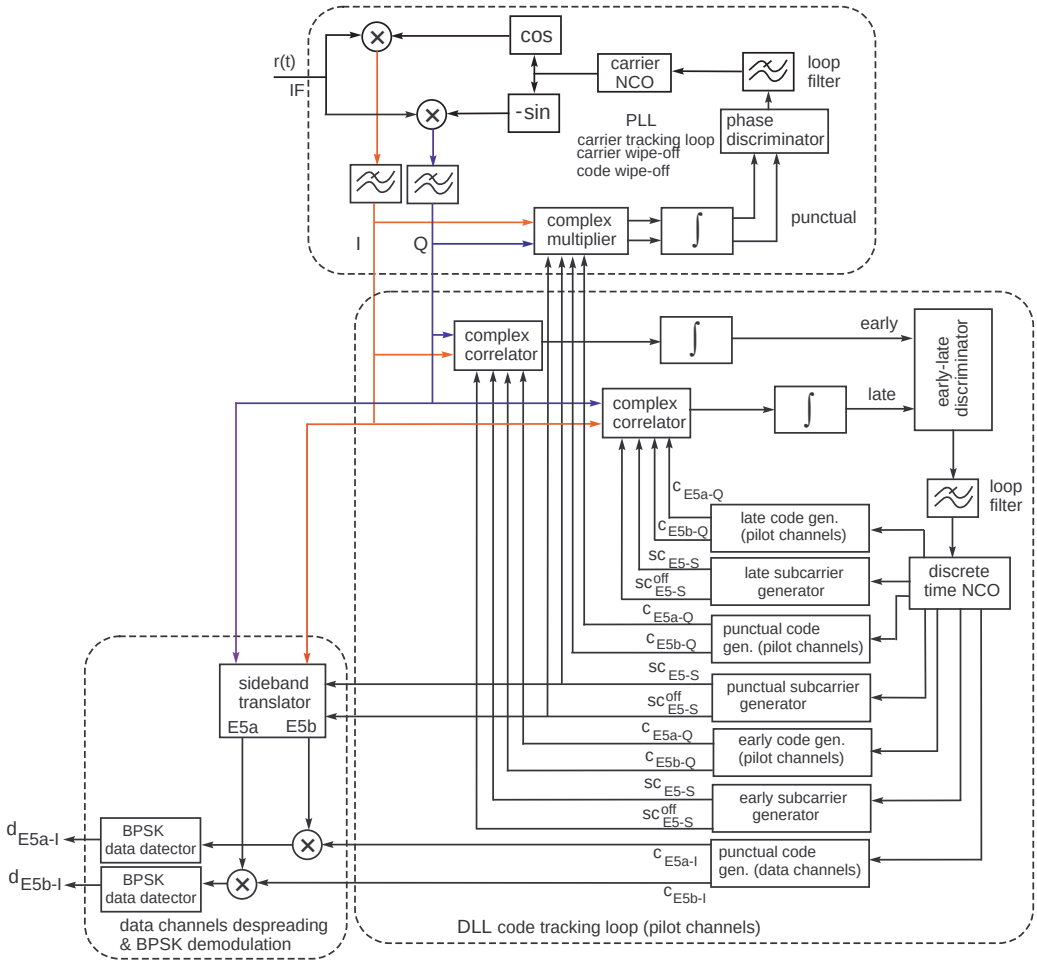

Figure 5.6: Block diagram of the dual band receiver architecture for Galileo AltBOC signals [9]

5.4.1 PLL

The PLL multiplies $r(t)$ by the inphase and quadrature components of the carrier NCO to produce

$$I_r(t) = 2r(t)\cos(2\pi f_c t + \phi) \tag{5.51}$$

$$Q_r(t) = -2r(t)\sin(2\pi f_c t + \phi) \tag{5.52}$$

with f_c denoting the estimated carrier frequency of the incoming signal (including Doppler frequency) and ϕ as the NCO phase error. Applying low-pass filtering yields

$$\begin{aligned}\begin{bmatrix} I(t) \\ Q(t) \end{bmatrix} &= A \begin{bmatrix} \cos\phi & \sin\phi \\ -\sin\phi & \cos\phi \end{bmatrix} \begin{bmatrix} \mathrm{Re}\{s_{E5}(t)\} \\ \mathrm{Im}\{s_{E5}(t)\} \end{bmatrix} \\ &= A \begin{bmatrix} \mathrm{Re}\{s_{E5}(t)\}\cos\phi + \mathrm{Im}\{s_{E5}(t)\}\sin\phi \\ -\mathrm{Re}\{s_{E5}(t)\}\sin\phi + \mathrm{Im}\{s_{E5}(t)\}\cos\phi \end{bmatrix}\end{aligned} \tag{5.53}$$

We perform next the complex correlation between signals

$$X(t) = I(t) + jQ(t) \tag{5.54}$$

$$\widetilde{X}(t) = \widetilde{I}(t) + j\widetilde{Q}(t) \tag{5.55}$$

where $\widetilde{X}(t)$ is the locally generated replica of $X(t)$. That is, $\widetilde{X}(t)$ is constituted by the parts of expressions (5.10) and (5.11) that do not depend on the navigation data, according to

$$\widetilde{I}(t) = \beta(t)\, sc_{E5-S}(t - T_s/4) \tag{5.56}$$

$$\widetilde{Q}(t) = \gamma(t)\, sc_{E5-S}(t) \tag{5.57}$$

The cross correlation of $X(t)$ and $\widetilde{X}(t)$ is defined as [36]

$$R_{X\widetilde{X}}(\tau) = \frac{1}{T_s}\int_0^{T_s} E\Big\{[I(t) + jQ(t)][\widetilde{I}(t-\tau) - j\widetilde{Q}(t-\tau)]\Big\}\, dt \tag{5.58}$$

Equation (5.58) leads to

$$R_{X\widetilde{X}}(\tau) = R_{I\widetilde{I}}(\tau) + R_{Q\widetilde{Q}}(\tau) + j[-R_{I\widetilde{Q}}(\tau) + R_{Q\widetilde{I}}(\tau)] \tag{5.59}$$

where generically

$$R_{uv}(\tau) = \frac{1}{T}\int_0^{T} E\Big\{u(t)v(t-\tau)\Big\}\, dt \tag{5.60}$$

with $R_{uv}(\tau) = R_{vu}(-\tau)$. Thus

$$
\begin{aligned}
R_{I\widetilde{I}}(\tau) &= \frac{1}{T_s}\int_0^{T_s} E\Big\{I(t)\widetilde{I}(t-\tau)\Big\}\,dt \\
&= \frac{1}{T_s}\int_0^{T_s} E\Big\{[\mathrm{Re}\{s_{E5}(t)\}\cos\phi + \mathrm{Im}\{s_{E5}(t)\}\sin\phi]\widetilde{I}(t-\tau)\Big\}\,dt \\
&= \frac{A\cos\phi}{2\sqrt{2}} E\{\beta(t)\beta(t-\tau)\}R_{sc}(\tau) \\
&= \frac{A\cos\phi}{\sqrt{2}} R_c(\tau)R_{sc}(\tau) \qquad (5.61)
\end{aligned}
$$

The other correlation functions in (5.59) are

$$
\begin{aligned}
R_{Q\widetilde{Q}}(\tau) &= \frac{1}{T_s}\int_0^{T_s} E\Big\{Q(t)\widetilde{Q}(t-\tau)\Big\}\,dt \\
&= \frac{1}{T_s}\int_0^{T_s} E\Big\{[-\mathrm{Re}\{s_{E5}(t)\}\sin\phi + \mathrm{Im}\{s_{E5}(t)\}\cos\phi]\widetilde{Q}(t-\tau)\Big\}\,dt \\
&= \frac{A\cos\phi}{2\sqrt{2}} E\{\gamma(t)\gamma(t-\tau)\}R_{sc}(\tau) \\
&= \frac{A\cos\phi}{\sqrt{2}} R_c(\tau)R_{sc}(\tau) \qquad (5.62)
\end{aligned}
$$

and

$$
\begin{aligned}
R_{I\widetilde{Q}}(\tau) &= \frac{1}{T_s}\int_0^{T_s} E\Big\{I(t)\widetilde{Q}(t-\tau)\Big\}\,dt \\
&= \frac{1}{T_s}\int_0^{T_s} E\Big\{[\mathrm{Re}\{s_{E5}(t)\}\cos\phi + \mathrm{Im}\{s_{E5}(t)\}\sin\phi]\widetilde{Q}(t-\tau)\Big\}\,dt \\
&= \frac{A\sin\phi}{2\sqrt{2}} E\{\gamma(t)\gamma(t-\tau)\}R_{sc}(\tau) \\
&= \frac{A\sin\phi}{\sqrt{2}} R_c(\tau)R_{sc}(\tau) \qquad (5.63)
\end{aligned}
$$

and

$$
\begin{aligned}
R_{Q\widetilde{I}}(\tau) &= \frac{1}{T_s}\int_0^{T_s} E\Big\{Q(t)\widetilde{I}(t-\tau)\Big\}\,dt \\
&= \frac{1}{T_s}\int_0^{T_s} E\Big\{[-\mathrm{Re}\{s_{E5}(t)\}\sin\phi + \mathrm{Im}\{s_{E5}(t)\}\cos\phi]\widetilde{I}(t-\tau)\Big\}\,dt \\
&= -\frac{A\sin\phi}{2\sqrt{2}} E\{\beta(t)\beta(t-\tau)\}R_{sc}(\tau) \\
&= -\frac{A\sin\phi}{\sqrt{2}} R_c(\tau)R_{sc}(\tau) \qquad (5.64)
\end{aligned}
$$

leading finally to

$$
R_{X\widetilde{X}}(\tau) = \sqrt{2}A\,R_c(\tau)R_{sc}(\tau)(\cos\phi - j\sin\phi) \qquad (5.65)
$$

Taking into account (5.59) and (5.65), the output of the 4-quadrant arctangent phase discriminator is

$$\widehat{\phi} = -\arctan 2\left(V(\epsilon),\, U(\epsilon)\right) \tag{5.66}$$

with

$$U(\epsilon) = \frac{1}{T}\int_0^T \left[I(t)\widetilde{I}(t-\epsilon) + Q(t)\widetilde{Q}(t-\epsilon)\right] dt \tag{5.67}$$

$$V(\epsilon) = \frac{1}{T}\int_0^T \left[Q(t)\widetilde{I}(t-\epsilon) - I(t)\widetilde{Q}(t-\epsilon)\right] dt \tag{5.68}$$

where ϵ is delay error of the local code generator.

5.4.2 DLL

The early and late arms of the DLL perform the complex correlations between the signals $X(t)$ and $\widetilde{X}(t)$ according to (5.59), with $\tau = -\Delta/2 + \epsilon$ and $\tau = \Delta/2 + \epsilon$, respectively.

The output of the early complex correlator is

$$R^E_{X\widetilde{X}} = R_{X\widetilde{X}}\left(\epsilon - \frac{\Delta}{2}\right) = \sqrt{2}AR_c\left(\epsilon - \frac{\Delta}{2}\right) R_{sc}\left(\epsilon - \frac{\Delta}{2}\right)\exp(-j\phi) \tag{5.69}$$

and the output of the late complex correlator is

$$R^L_{X\widetilde{X}} = R_{X\widetilde{X}}\left(\epsilon + \frac{\Delta}{2}\right) = \sqrt{2}AR_c\left(\epsilon + \frac{\Delta}{2}\right) R_{sc}\left(\epsilon + \frac{\Delta}{2}\right)\exp(-j\phi) \tag{5.70}$$

Different types of DLLs may be devised. For instance, the early-late (EL) discriminator is given by

$$\begin{aligned} D_{EL}(\epsilon) &= \mathrm{Re}\{R^E_{X\widetilde{X}}\} - \mathrm{Re}\{R^L_{X\widetilde{X}}\} \\ &= \sqrt{2}A\left[\Lambda\left(\frac{\epsilon - \Delta/2}{T_c}\right) R_{sc}(\epsilon - \Delta/2) - \Lambda\left(\frac{\epsilon + \Delta/2}{T_c}\right) R_{sc}(\epsilon + \Delta/2)\right]\cos\phi \end{aligned} \tag{5.71}$$

This discriminator requires small values of the phase error ϕ (quasi-coherent scenario). The discriminator may be affected by false code-locks which lead to delay errors around $\pm 0.62T_c$. The (coherent) code discriminator response is displayed in fig. 5.7 for different early-late spacings with $\sqrt{2}A = 1$ and $\phi = 0$.

If, instead, a NELP discriminator is used, the response of the discriminator is given by

$$\begin{aligned} D_{NELP}(\epsilon) &= |R^E_{X\widetilde{X}}|^2 - |R^L_{X\widetilde{X}}|^2 \\ &= 2A^2\left[\Lambda^2\left(\frac{\epsilon - \Delta/2}{T_c}\right) R^2_{sc}(\epsilon - \Delta/2) - \Lambda^2\left(\frac{\epsilon + \Delta/2}{T_c}\right) R^2_{sc}(\epsilon + \Delta/2)\right] \end{aligned} \tag{5.72}$$

Unlike the EL discriminator, the NELP discriminator is immune to carrier phase errors. The main

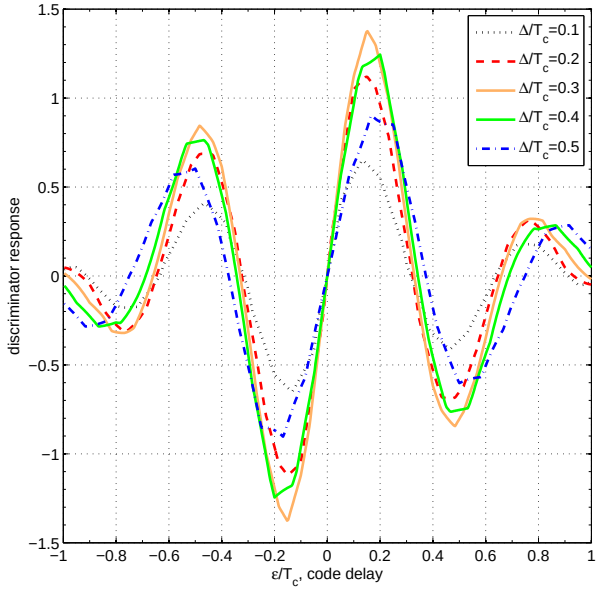

Figure 5.7: EL discriminator response for different values of the early-late spacing

drawback is the possibility of false code-locks around $\pm 0.32T_c$ and $\pm 0.62T_c$. The non-coherent code discriminator response is displayed in fig. 5.8 for different early-late spacings with $2A^2 = 1$.

Inspection of (5.72) reveals that the NELP response depends on the amplitude A of the received signal which an undesirable feature of the discriminator. One possible solution consists of adjusting A to an approximately constant value by means of an automatic gain control (AGC). Alternatively, a power normalized version of the NELP discriminator may be used with response

$$\begin{aligned} D_{NELP}(\epsilon) &= \frac{|R^E_{X\tilde{X}}|^2 - |R^L_{X\tilde{X}}|^2}{|R^E_{X\tilde{X}}|^2 + |R^L_{X\tilde{X}}|^2} \\ &= \frac{\Lambda^2\left(\frac{\epsilon-\Delta/2}{T_c}\right) R^2_{sc}(\epsilon-\Delta/2) - \Lambda^2\left(\frac{\epsilon+\Delta/2}{T_c}\right) R^2_{sc}(\epsilon+\Delta/2)}{\Lambda^2\left(\frac{\epsilon-\Delta/2}{T_c}\right) R^2_{sc}(\epsilon-\Delta/2) + \Lambda^2\left(\frac{\epsilon+\Delta/2}{T_c}\right) R^2_{sc}(\epsilon+\Delta/2)} \end{aligned} \tag{5.73}$$

which does not depend on A. This solution was adopted in the simulations carried out in the next chapter.

Figure 5.9 displays the response of the normalized NELP discriminator for different E-L spacing.

5.4.3 Sideband translator

The data bits can be recovered by using the sideband translator sketched in fig. 5.10.

Multiplying $\mathrm{Re}\{s_{E5}(t)\}$ in (5.18) by $\cos(2\pi f_s t)$ and filtering lowpass the result yields

$$z_I(t) = \frac{1}{\pi\sqrt{2}}\,\alpha(t) \tag{5.74}$$

Similarly, multiplying $\mathrm{Im}\{s_{E5}(t)\}$ in (5.18) by $\sin(2\pi f_s t)$ and filtering lowpass the result leads to

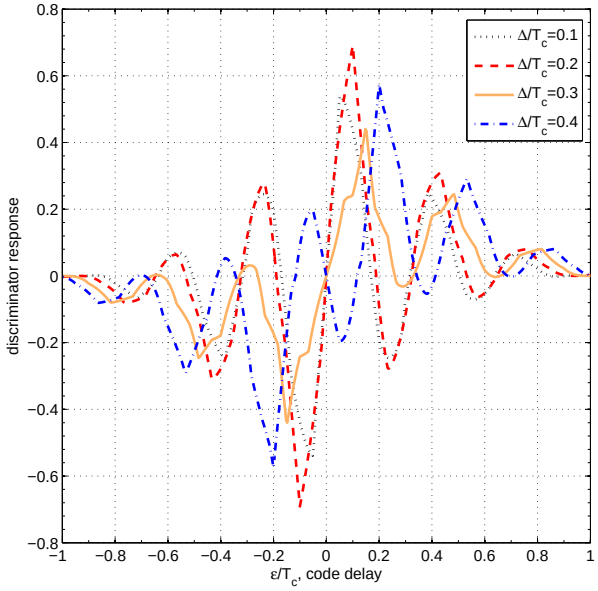

Figure 5.8: NELP discriminator response for different values of the early-late spacing

$$z_Q(t) = \frac{1}{\pi\sqrt{2}}\,\mu(t) \tag{5.75}$$

Finally, summing or subtracting the previous quantities, we obtain the desired data sequences

$$z_I(t) - z_Q(t) = \frac{\sqrt{2}}{\pi} e_{E5a-I}(t) \tag{5.76}$$

$$z_I(t) + z_Q(t) = \frac{\sqrt{2}}{\pi} e_{E5b-I}(t) \tag{5.77}$$

A thorough discussion of other receiver architectures for AltBOC signals, both single- and double-sideband, is found in [10].

The architecture analyzed in this section can be simplified in case sub-band processing is performed. For instance, if we consider that only sub-band E5a signal is received (by filtering out the sub-band E5b signal) the front-end signal is

$$r(t) = \frac{A}{2\sqrt{2}}\Big[e_{E5a-I}(t)\cos((\omega_0 t + \omega_d t - \omega_s)t) - e_{E5a-I}(t)\cos((\omega_0 t + \omega_d t - \omega_s)t)\Big] \tag{5.78}$$

Then $e_{E5b-I}(t) = e_{E5b-Q}(t) = 0$, leading to

$$\alpha(t) = -\mu(t) = e_{E5a-I}(t) \tag{5.79}$$

$$\beta(t) = \gamma(t) = e_{E5a-Q}(t) \tag{5.80}$$

In this case, the equations and the architecture of the current section are still valid and we ob-

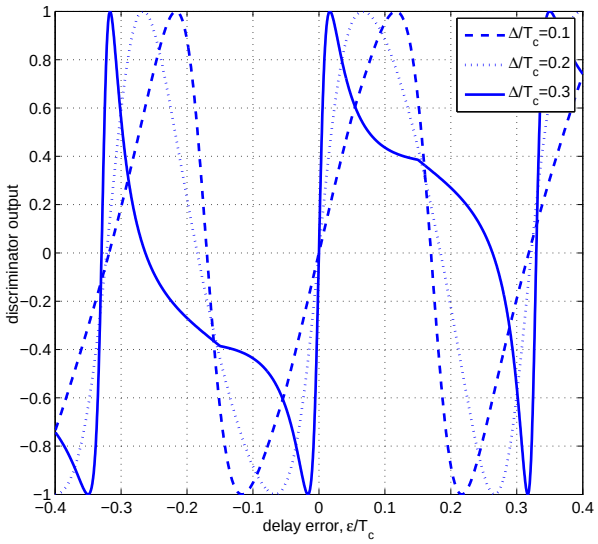

Figure 5.9: NELP normalized discriminator response for different values of the early-late spacing

tain a single sideband AltBOC receiver which uses the FIC method. The implementation details and performance achieved with this simplified receiver and the full-band (double sideband) receiver will be discussed in the next chapter. The analysis carried out in this chapter omitted the effect of channel noise in order to simplify the results and conclusions. In the next chapter the Monte Carlo simulations will evaluate the degradation introduced by the presence of noise on the carrier and code loops.

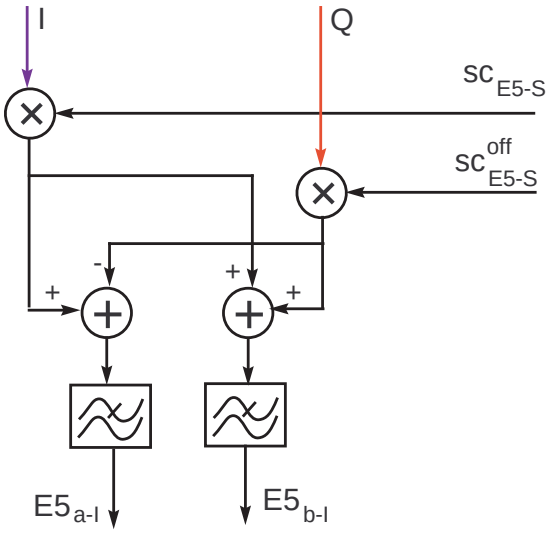

Figure 5.10: Block diagram of the sideband translator [9]

Chapter 6

Implementation and Results

This chapter analyzes Monte Carlo simulation aspects in Section 1 and the implementation process in section 2 is subdivided in parametrization (where the most important parameters are presented and discussed) and plots where a typical output of the simulation is presented. In section 3 the testing results with varying C/N_0 are presented and commented. Section 4 shows the results obtained when interference is added to the algorithm.

This chapter is a practical application of the theoretical research made in chapter 5. In particular the architecture presented in fig. 5.6 is considered with Double Sideband and Single Sideband approaches. The simulated receiver is fully implemented in Matlab.

6.1 Monte Carlo Simulation Aspects

An important question to be answered within the context of the Monte Carlo simulation is how many runs are necessary to evaluate the receiver performance variable X (for instance, the DLL rms code error) with regard to a certain parameter S, such as $S = C/N_0$. The immediate solution is: the larger the number of runs the better. However, the user is faced with a tradeoff between run time and statistical variability [37]. In fact, simulation is computationally expensive because the required sampling rate of the AltBOC signals to meet the Nyquist criterion is very high, typically > 50 Msamples/s and the brute force solution is, in general, prohibitive.

Consider that the quantity X is to be estimated from noisy observations z_k through the observation model $z_k = X + n_k$, where n_k is the observation noise. Often the noise sequence is assumed to be white (independent noise variables), stationary, zero-mean, and Gaussian. The variance of n_k is σ_n^2. The optimum maximum likelihood estimator is

$$\widehat{X} = \frac{1}{N} \sum_{i=1}^{N} z_k \tag{6.1}$$

with N denoting the number of independent observations. This estimator is unbiased and has variance $\sigma_X^2 = \sigma_n^2/N^2$. Let L be the confidence interval with confidence level $1 - \alpha$, that is

$$\text{Prob}\{X - L/2 \leq \widehat{X} \leq X + L/2\} = 1 - \alpha \tag{6.2}$$

leading to

$$\frac{1}{\sqrt{2\pi\sigma_X^2}} \int_{-L/2}^{L/2} \exp\left(-\frac{x^2}{2\sigma_X^2}\right) dx = 1 - \alpha \tag{6.3}$$

or $\alpha = 2Q(L/(2\sigma_X))$, where $Q(\cdot)$ is the complementary error function

$$Q(x) = \frac{1}{\sqrt{2\pi}} \int_x^\infty \exp(-y^2/2)\, dy \tag{6.4}$$

Finally, one obtains

$$N > \frac{2\sigma_n}{L} Q^{-1}\left(\frac{\alpha}{2}\right) \tag{6.5}$$

which shows that the minimum number of observations (or Monte Carlo runs) grows with the standard deviation of the observations. It increases also with the inverse of the confidence interval and the inverse of α. For instance, if $\alpha = 0.05$ (95% confidence level) the rule is $N > 3.94(\sigma_n/L)$. In practical cases the observations variance may not be known but may be estimated from the observations.

Due to the scarcity of the available simulation time I proceeded as follows. Consider that the receiver performance variable X is to be evaluated with regard to the input parameter S which takes values in the interval $[S_l,\, S_u]$. In each run k, a new value of S is generated using the formula

$$S_k = (1 - u_k)S_l + u_k S_u, \quad k = 1, 2, \ldots, K \tag{6.6}$$

where each $u_k \in [0,\, 1]$ is an independent uniformly-distributed random variable. Thus, S_k is uniformly distributed in the interval [S_l,S_u]

The interval $[S_l,\, S_u]$ is then divided into a pre-defined number M of sub-intervals (with $M \ll K$). In each sub-interval I_m, $m = 1, \ldots, M$, the corresponding estimate $\widehat{X}(m)$ is computed by averaging the estimates $\widehat{X}_k$ that fall within I_m. The advantage of this procedure is that the simulation program can be stopped at any time (to be possibly resumed later) with the user being able to estimate the behavior of the receiver performance variable X along the whole interval $[S_l,\, S_u]$. Obviously, as more observations become available the accuracy of the estimates $\widehat{X}(m)$ is improved according to (6.5). This procedure is quite convenient for simulation parallelization where different PCs operate in parallel with the same program but using distinct noise ”seeds”. The merge of the partial results permits to build a plot of $X(S)$ with the desired accuracy.

6.2 Simulation Process

The simulation process is divided in this section into two important steps:

- **Parametrization and simulation**: where the parameters to be tested are defined

Variable	F=fixed, T=tested	Value	Units
$\mathrm{Time_{simulation}}$	T	[0,+∞[	s
$\mathrm{Frequency_{sampling}}$	F	58.5813	MHz
$\mathrm{C/N_0}$	T	[20:50]	dB-Hz
$\mathrm{Time_{integration}}$	T	[1,2]	ms
Early Late Spacing	T	[0.1,0.2]	$\mathrm{T_C}$
$\mathrm{B_{PLL}}$	F	20	Hz
ξ_{PLL}	F	0.707	adimensional
$\mathrm{B_{DLL}}$	F	0.15	Hz
$\mathrm{Frequency_{Doppler}}$	F	5000	Hz
$\mathrm{Frequency_{Doppler+error}}$	F	5020	Hz
$\mathrm{T_C}$	F	$\approx$ 65.168	ns
$\mathrm{Frequency_{carrier}}$	F	1.191795	GHz
$\mathrm{Frequency_{subcarrier}}$	F	15.345	MHz
Chip Rate	F	10.23	MHz

Table 6.1: Table of used parameters

- **Image Generation**: where the results for the given parameters are obtained.

6.2.1 Parametrization

In this step a definition of the variable values to be tested in the signal processing phase is needed. These parameters are extensive and are summarized in table 6.1.

A brief explanation is presented regarding the importance and influence of each variable in the simulation process:

- **Time of Simulation**: Parameter that controls the processed signal length by extending the number of integrations made. Depending on the device, an average ratio of 1:400 (1 second of simulated signal = 400 seconds of processing real time) for each processing core is obtained.

- **Sampling Frequency**: This parameter influences the signal discretization process. The chosen value of 58.5813 MHz depends on various factors like minimum (Nyquist) sampling frequency and noise bandwidth. In our case, the combined frequencies of the subcarrier and the chipping rate result in an equivalent baseband bandwidth of $f_{BB} = f_{subc} + f_{chip} = 25.575$ MHz which dictates a Nyquist minimum sampling frequency of $2 \times 25.575 = 51.15$ MHz. Regarding the sampling frequency a detailed analytical description is given in appendix C.

- **C/N$_0$**: The input GNSS signal is controlled by C/N$_0$ as it modifies the signal amplitude relatively to the noise amplitude (assumed constant in the simulation).

- **Time of Integration**: This parameter defines the time interval where the receiver accumulates

data and influences the response speed of the receiver and robustness to noise (higher integration times permit a lower sensibility to noise but makes the receiver response to variations slower).

- **Early Late Spacing**: EL spacing controls the interval between the early and late replicas when correlating the local generated and received signals. A higher value of EL spacing will result in higher early late replicas power discrepancy and influence the discriminator output.

- **$\mathbf{B_{PLL}}$ and $\mathbf{B_{DLL}}$**: These parameters define the equivalent noise bandwidth of the PLL and DLL respectively which influence the response time of each loop to code delay and frequency variations (higher bandwidths results in better response but exhibit higher sensibility to noise). The value of the DLL equivalent noise bandwidth may be low because the tracking algorithm is aided by the PLL (rate aided DLL). In fact, rate-aiding allows the noise bandwidth to be significant smaller. A smaller bandwidth is tolerable because any system dynamics is captured by the rate estimates from the PLL. Thus, the bandwidth of rate aided DLLs can be as low as 0.005 Hz [14]. Smaller bandwidths are prone to raise problems because the ionosphere eventually causes the receiver code delay to diverge from the carrier phase. The characterization of the second-order PLL used in the simulations is done in appendix D.
  The first-order DLL used in the simulations is characterized by the gain

$$G_{\mathrm{DLL}} = \gamma_c g_c \tag{6.7}$$

  where γ_c is an adimensional factor and g_c is the slope of the normalized discriminator response $D_{\mathrm{NELP}}(\epsilon)$ at $\epsilon = 0$ (NELP discriminator gain), with $D_{\mathrm{NELP}}(\epsilon)$ given by (5.73). The NELP discriminator gain g_c versus the E-L spacing is shown in fig. 6.1. For (non-rate aided) first-order DLL the noise equivalent bandwidth becomes [14]

$$B_{\mathrm{DLL}} = \frac{G_{\mathrm{DLL}}}{4} = \frac{\gamma_c g_c}{4} \tag{6.8}$$

- **Doppler Frequency**: Doppler frequency is related to the relative speed satellite-receiver as

$$f_D = -\frac{V f_c}{c} \tag{6.9}$$

  where V is the relative speed satellite-receiver, c is the speed of light, and f_c is the carrier frequency.
  With a Doppler frequency of 5000 Hz we are simulating a speed of $\approx$ 1250 m/s which translate into a constant phase and code delay decrease.

- **E5 Signal constants**: The carrier and subcarrier frequency and chip rate are all characteristics of the simulated E5 AltBOC signal.

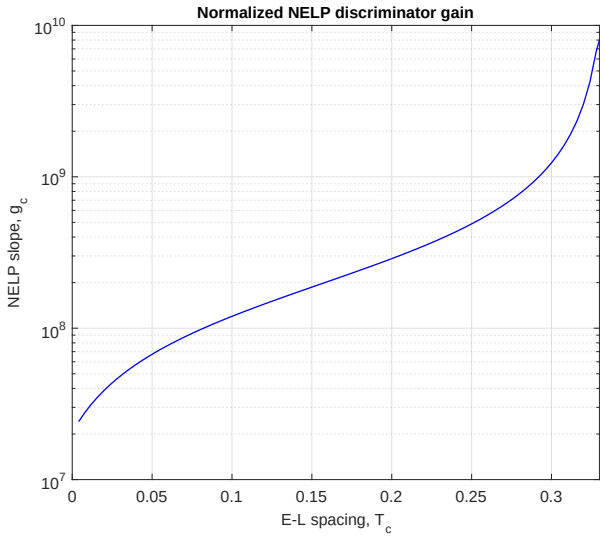

Figure 6.1: Normalized NELP discriminator gain versus E-L spacing

EL	0.2 T_C
CN_0	50 dB-Hz
Time of simulation	1 s
Time of Integration	2 ms

Table 6.2: Parameter set

6.2.2 Plots

After the simulation process in concluded, the final step is to generate the corresponding results in the form of visual information. Specifically, the generated plots show the discriminators outputs of both the PLL and DLL and the phase and code errors along the time of simulation. The typical plots that are generated in the end are alike the ones presented in fig. 6.2, 6.3, 6.4 and 6.5 (these figures are the result of the parameter set in table 6.2 along with the fixed parameters displayed in table 6.1). These figures represent a situation where both the PLL and DLL are functioning properly with a C/N_0 of 50 dB-Hz.

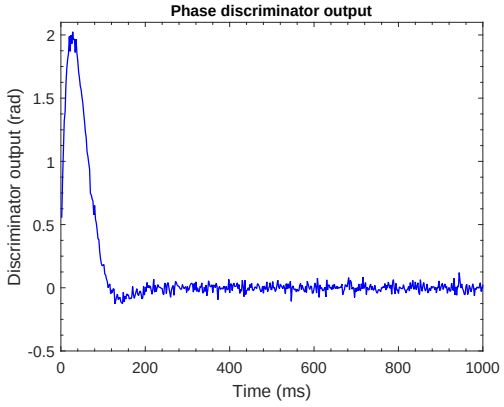

Figure 6.2: PLL discriminator output

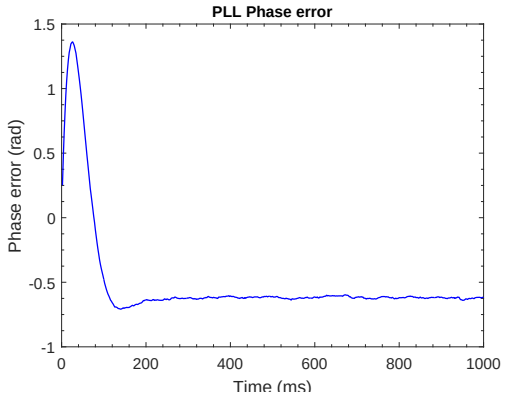

Figure 6.3: Phase error

Figure 6.2 represents the Phase discriminator output and shows the convergence of the response to 0 after a period of transition and figure 6.3 shows the error of the phase along the simulation around -0.625 rad or -37 degrees.

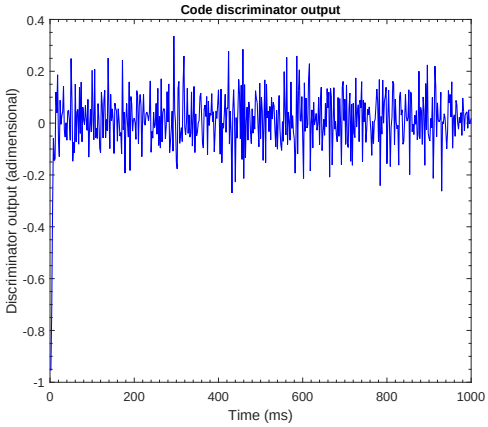

Figure 6.4: DLL discriminator output

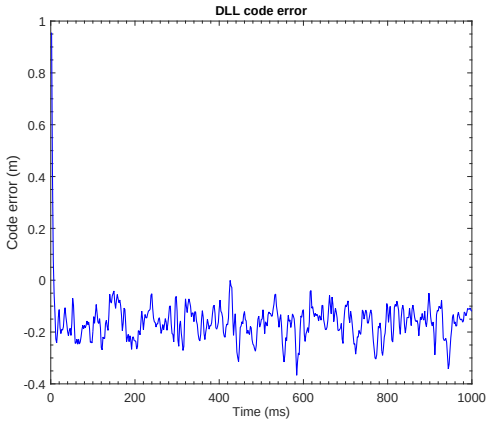

Figure 6.5: Code error

Figure 6.4 represents the code discriminator output and also shows the convergence of the response to 0 after a transient and figure 6.5 shows the error of the code along the simulation stabilizing around 0.2 m.

Figures 6.6, 6.7, 6.8 and 6.9 represent the results obtained for a C/N_0 of 50 dB-Hz where we purposely input an error to the Doppler frequency at t=600 ms and where we can observe the phase and code errors diverging. The Doppler frequency was increased by a value of 25 Hz per ms during the interval of 8 ms corresponding to a total of 200 Hz. This situation caused the PLL to lose track and induces an error to the DLL code error output. In the simulation process, the lock was considered to be lost when a phase larger than 1 rad was observed in the phase discriminator output at any time.

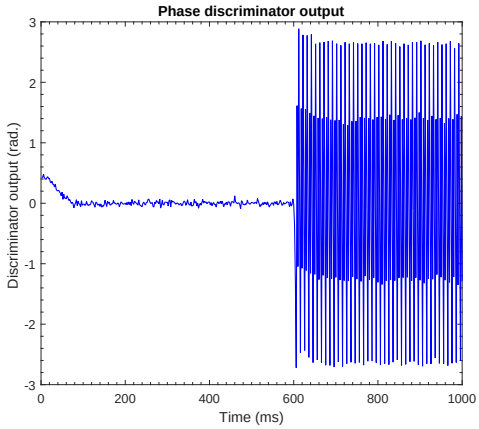

Figure 6.6: Phase discriminator of failed lock

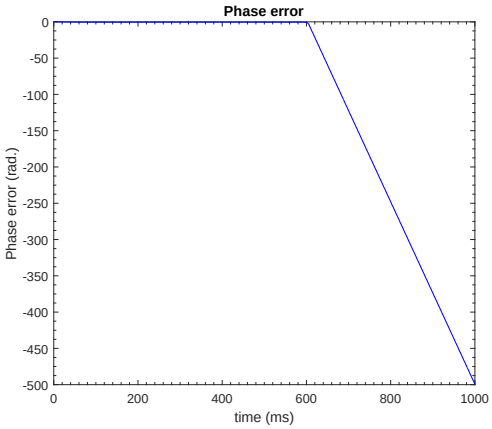

Figure 6.7: Phase error of failed lock

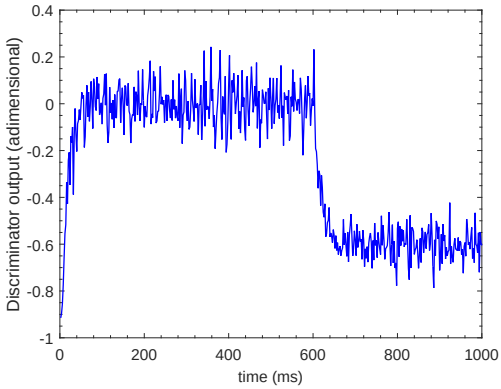

Figure 6.8: Code discriminator of failed lock

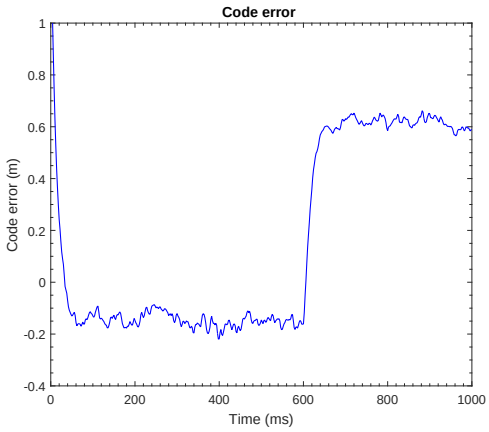

Figure 6.9: Code error of failed lock

6.3 Results

The test step is composed by an iterating optimization process (where each parameter is optimized while all others are fixed) and a robustness test where the carrier-to-noise value is decreased resulting in a GNSS signal amplitude decrease. Since the receiver is simulated with random noise, the results varies in a small interval of tested parameters. To avoid this problem, in a given graph, the results are grouped by fixed length intervals and averaged in order to mitigate spiked looking graph lines. To avoid engaging in periodic phenomenon biased solutions, all parameter values are randomly chosen by a uniform distribution in a given interval, as mentioned in section 6.1.

The optimization process consists in optimizing individually each parameter. The optimized parameters are the signal sampling frequency (f_{sample}), PLL equivalent noise bandwidth (B_{PLL}) and DLL equivalent noise bandwidth (B_{DLL}). The tests were made for both the SSB and DSB to check the consistency of the chosen parameter values. The resulting optimized parameters were already shown in table 6.1.

The following section displays the results regarding the tests with varying C/N_0. The criterion used to detect lock failure consists in declaring loss of lock whenever the phase error exceeds 1 radian.

6.3.1 C/N_0 Variation

In this section, we present the results of testing the simulated receiver to noise for two distinct parameters: early-late spacing (EL) and integration time (T_{int}) for both SSB and DSB. Figure 6.10 indicates the percentage of loss of lock versus C/N_0 and fig. 6.11 indicates the RMS errors versus C/N_0. In both cases different values of T_{int} were considered. Keep in mind that the error values in fig. 6.11 correspond to the part of simulations where there was not loss of tracking.

Analyzing fig. 6.10 and 6.11, we conclude that:

- the percentage of loss of tracking is essentially independent of the bandwidth considered, SSB or DSB;

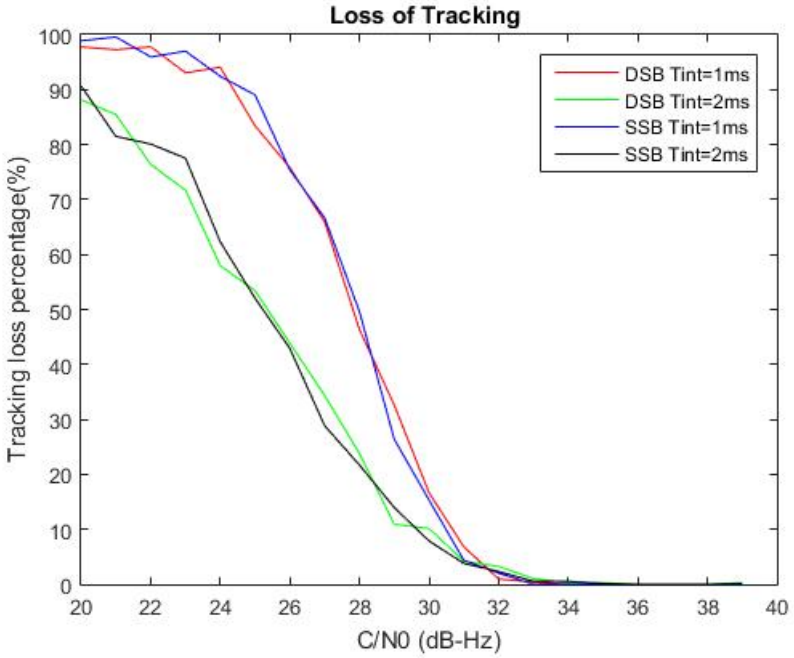

Figure 6.10: Loss of tracking of SSB and DSB for T_{int}=[1,2] ms

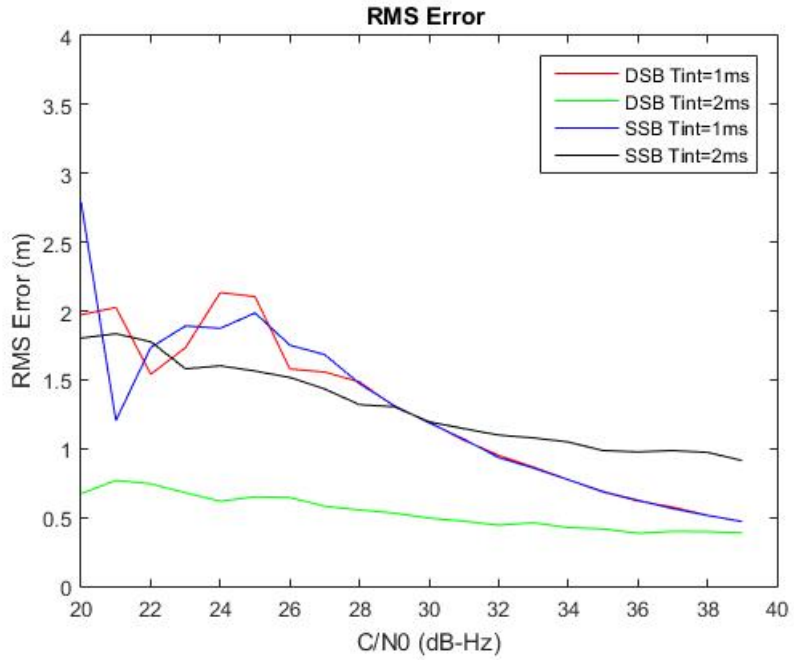

Figure 6.11: RMS error of successful trackings for SSB and DSB for T_{int}=[1,2] ms

- generally, at lower C/N_0, T_{int}=2 ms presents better results for both SSB and DSB than T_{int}=1 ms with respect to loss of tracking;
- the DSB simulation presents better code error values;
- for C/N_0 <25 dB-Hz, the variance of the error is high because in this interval the tracking loss is almost certain (100%) which permits to recover only a few valid error values;

- for higher values of C/N_0 a time of integration of 1 ms is better than 2 ms when comparing the average error;
- for $C/N_0 > 31$ dB-Hz approximately, the probability of track loss is $< 10\%$ for both bands and integration time tested.

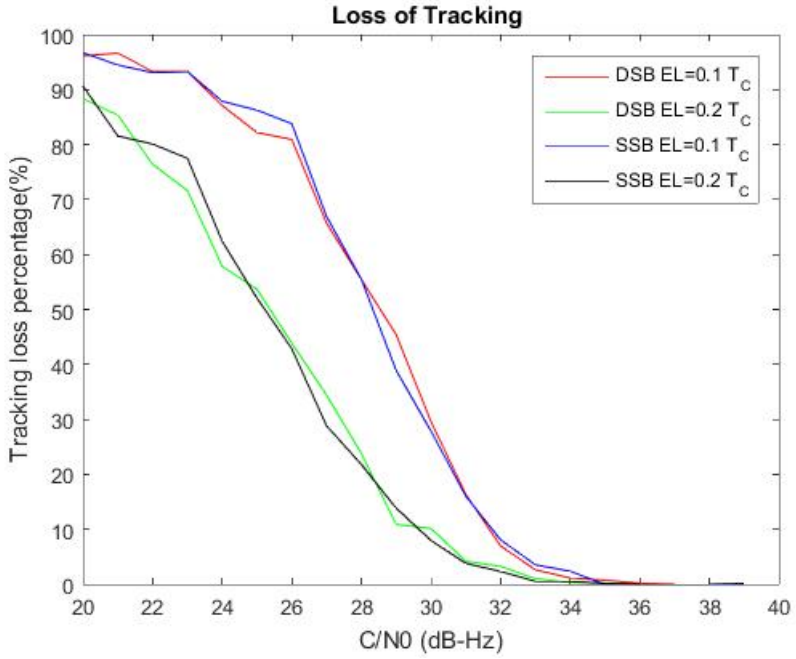

Figure 6.12: Loss of tracking of SSB and DSB for EL=[0.1,0.2] T_C

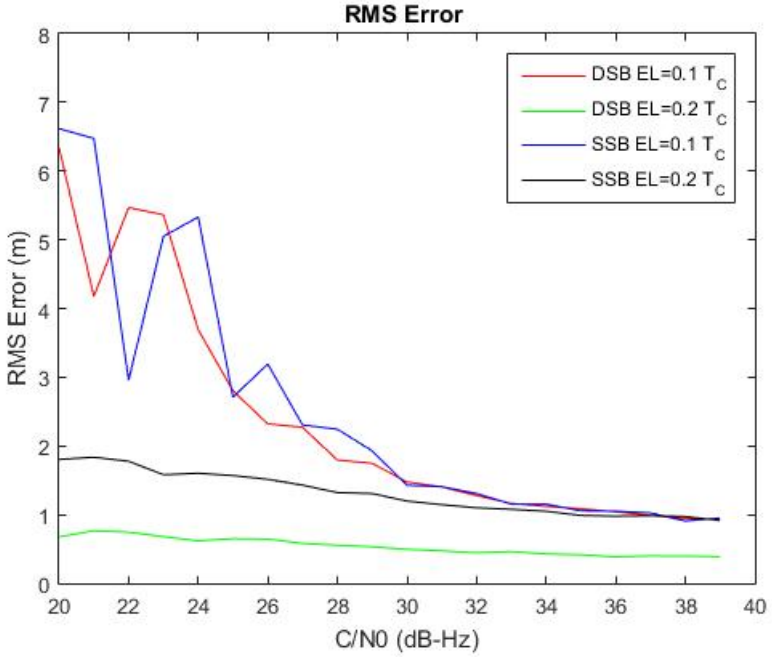

Figure 6.13: RMS error of successful trackings for SSB and DSB for EL=[0.1,0.2] T_C

Figures 6.12 and 6.13 indicate, respectively, the percentage of loss of tracking and RMS errors

versus C/N_0 obtained with different values of early-late spacing. The early-late spacing parameter has influence when correlating the local signal replica and the receiver signal. By analyzing figures 6.12 and 6.13 we can conclude that:

- generally EL=0.2 T_C presents better results for both SSB and DSB than EL=0.1 T_C at all C/N_0 except for SSB at high C/N_0 which seemed independent;
- the DSB simulation presents better code error values;
- for C/N_0 <25 dB-Hz, the variance of the error is high because in this interval the tracking loss is almost certain (100%) which permits to recover only a few valid error values.

6.4 Interference Test

This section is part of the paper accepted for presentation in the ICL-GNSS2016 conference [38].

Current Global Navigation Satellite Systems use spread-spectrum modulation schemes but, due to the weak power of the received signals at the earth surface, they can be easily disturbed or even destroyed in the presence of certain types of RFI (radio frequency interference) which are intentionally provoked (jamming) or are due to the proximity of authorized radio sources, such as TV/FM, radar, navigation and mobile systems [23]. In general, non-intentional RFI is provoked by narrowband continuous or pulsed signals whereas jamming is caused by wideband transmitters using frequency modulated chirp signals. We assume that the received signal $r(t)$ is disturbed by the additive RFI waveform

$$s(t) = A_J \cos(\varphi_J(t)) \tag{6.10}$$

with the interference-to-noise power being $C_I/N_0 = A_J^2/(2N_0)$. Two types of continuous interferers are considered: a sinusoidal waveform of frequency $f_0 + f_J$, with f_J accounting for the jammer's frequency offset regarding the GNSS carrier frequency, and a chirp waveform, with period of repetition T_J, described by

$$\varphi_J(t) = 2\pi(f_0 - W/2)\tau(t) + \pi\gamma_J\tau^2(t) + \varphi_0. \tag{6.11}$$

W stands for the frequency sweep range, $\gamma_J = W/T_J$ and $\tau(t) = \mathrm{mod}(t, T_J)$ is the remaining part after division of t by T_J with $0 \leq \tau(t) < T_J$. The instantaneous frequency $(2\pi)^{-1}(d\varphi_J(t)/dt)$, centered at the carrier frequency f_0, is sketched in fig. 6.14.

Figures 6.15 and 6.16 illustrate the mechanism of loss of phase and code tracking due to the introduction of a sinusoidal signal of interference with frequency $f_J = 1$ MHz at time $t = 0.15$ s. The carrier-to-noise density ratio due to thermal noise is $(C/N_0) = 50$ dB-Hz and the interference-to-noise density ratio is $(C_I/N_0) = 95$ dB-Hz. The correlation interval is $T = 2$ millisecond and the adopted sampling rate is 58.52 Msamples/s which corresponds to 5.72 samples per chip. The PLL filter parameters are $a = 1348$ and $b = 52$, which corresponds to a loop bandwidth $B_n = 20$ Hz and damping factor $\xi = 0.71$. The early-late spacing of the normalized NELP discriminator is made equal to $0.2T_c$ yielding

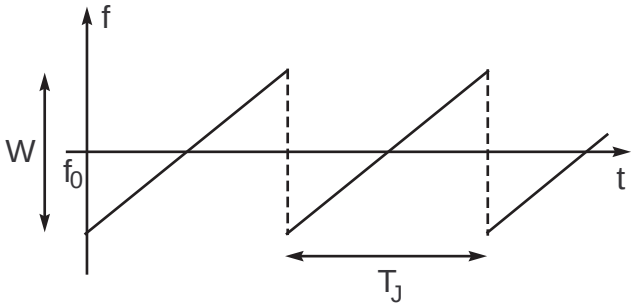

Figure 6.14: Frequency sweep of the chirp jamming signal.

a gain $g_c = 3 \times 10^8/\mathrm{s}$. The loop gain γ_c is 2×10^{-9} producing a DLL bandwidth of 0.15 Hz. In all the simulations we considered a Doppler frequency of 5 kHz.

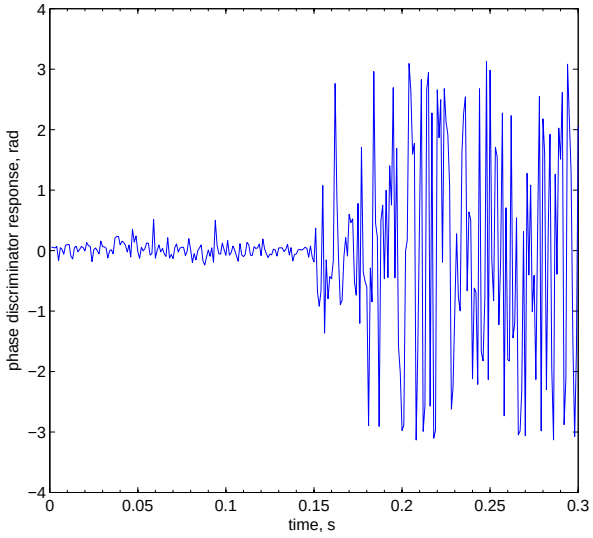

Figure 6.15: Example of PLL phase discriminator response in radians in the presence of sinusoidal interference

The effective signal carrier-to-noise density ratio [34]

$$\left(\frac{C}{N_0}\right)_{\text{eff}} = \left(\frac{C}{N_0}\right) \frac{\eta}{1 + \left(\frac{C_I}{N_0}\right) \frac{k_{\text{ssc}}}{\eta}} \tag{6.12}$$

is a useful way to quantify the effect of the interference on the quality of the received signal. In (6.12),

$$\eta = \int_{-B}^{B} G_s(f)\, df < 1 \tag{6.13}$$

is the fraction of signal power passed by the precorrelation bandwidth. Parameter k_{ssc} is the spectral separation coefficient (SSC) defined by

$$k_{\text{ssc}} = \int_{-B}^{B} G_I(f) G_s(f)\, df \tag{6.14}$$

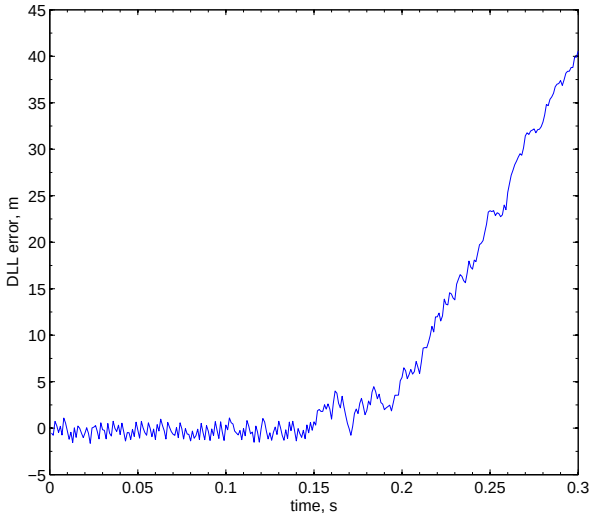

Figure 6.16: Example of DLL code error in meters in the presence of sinusoidal interference

where $2B$ is the RF bandwidth, $G_I(f)$ is the normalized interference power spectrum and $G_s(f)$ is the AltBOC signal normalized power given in equation (4.30).

Equations (6.12) and (6.14) show that the reduction of $(C/N_0)_{\text{eff}}$ for a given value of $C_I/N_0)$ depends on the SSC. For narrowband (sinusoidal) interference with frequency f_J the interference power spectrum is $G_I(f) = (1/2)[\delta(f + f_J) + \delta(f - f_J)]$ and the SSC is given by $k_{\text{ssc}} = G_s(f_J)$. Therefore, the receiver's resistance to RFI depends on the frequency f_J with maximum robustness being expected when f_J is close to a null of $G_s(f)$ (the first positive minima of $G_s(f)$ occur at 5.115 MHz and 25.57 MHz). This behavior is corroborated by Monte Carlo simulations carried out with full band and with upper sub-band signal processing, as shown in fig. 6.17. The figure presents the smallest values of (C_I/N_0) (averaged over 25 independent runs) which lead to the loss of lock of the DLL/PLL. We adopted the PLL discriminator output exceeding 1 radian as the criterion for the loss of lock. Near the spectrum nulls we note an increase of the receiver robustness to interference. On the other hand, the minimum of robustness to RFI is obtained at the frequency corresponding to the maximum of the power spectrum which is approximately 15 MHz.

The upper sub-band signal processing still uses the structure of fig. 5.6 but now the reference signals $\widetilde{I}(t)$ and $\widetilde{Q}(t)$ are simplified to

$$\widetilde{I}(t) = -e_{E5b-Q}(t)\text{sc}_{E5-S}(t - T_s/4) \tag{6.15}$$

$$\widetilde{Q}(t) = e_{E5b-Q}(t)\text{sc}_{E5-S}(t) \tag{6.16}$$

Since the power contained in the upper sub-band is only half the full-band power, the receiver exhibits a smaller immunity against interference, as shown in the figure (dashed line). The degradation is around 6 dB.

Consider now wideband RFI. It can be shown [39] that the line power spectral density of the chirp in-

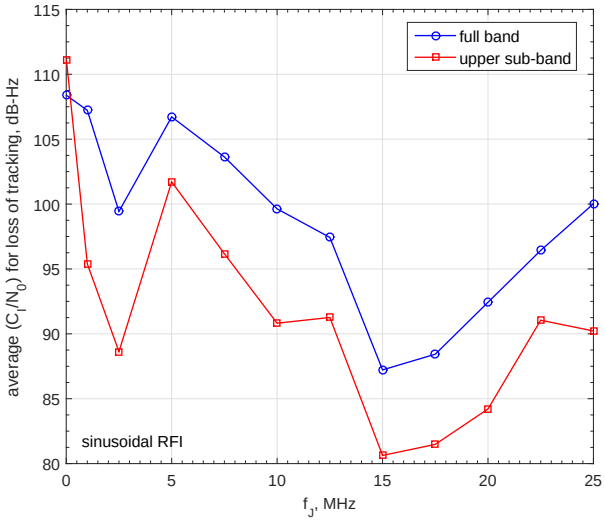

Figure 6.17: Average (C_I/N_0) for loss of tracking with full band and upper sub-band processing for sinusoidal interference

terference is approximately rectangular with bandwidth W, provided that $WT_J \gg 1$. Taking into account the rectangular approximation to the RFI power spectrum, the SSC is well approximated by

$$k_{\text{SSC}} \approx \frac{1}{W} \int_{-W/2}^{W/2} G_s(f)\, df \tag{6.17}$$

with the plot being displayed in fig. 6.18.

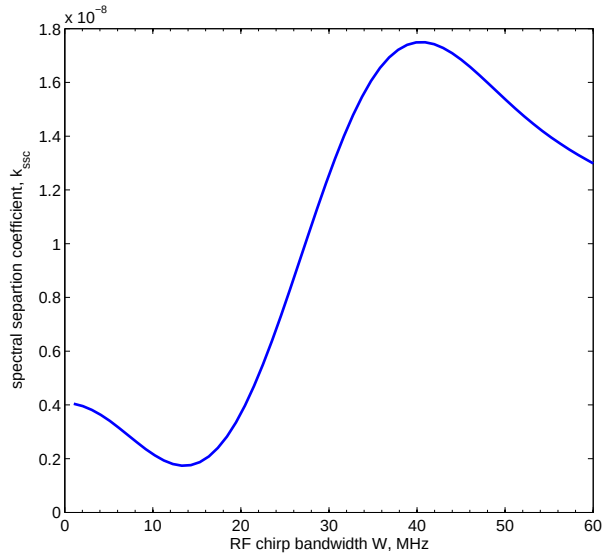

Figure 6.18: Spectral separation coefficient versus the RF chirp signal bandwidth

The simulation results of Fig. 6.19 were plotted using two different chirp repetition periods: $T_J = 20\,\mu$s and $200\,\mu$s. The figure shows that the robustness to interference is maximum in the region with $W < 20$ MHz, which corresponds to the SSC minimum both for full-band and upper sub-band processing.

In Fig. 6.19 we found a loss of robustness of about 6 dB when half-band processing replaces the full-band processing because the power of the incoming signal is decreased by half. Also, there is no clear difference in the receiver's performance between the two chirp repetition periods, T_J, for $W < 25$ MHz, but above that value the receiver becomes less robust to the interference with smaller value of T_J.

In general, the pattern of robustness for the chirp RFI follows relatively well the evolution of the SSC parameter plotted in Fig. 6.18. In fact, the maximum of robustness is achieved at low values of W and starts to diminish for $W > 15$ MHz which corresponds to the positive slope of the SSC plot. The minimum of robustness is achieved at $W \approx 35$ MHz which corresponds approximately to the maximum of the SSC curve.

Simulations have shown that the performance degradation due to radio frequency interference is well predicted by SSC both for the narrowband and the wideband interference signals under test. In the case of the chirp interference, the SSC value depends both on the power spectral density of the modulated signal and the frequency range of the interfering signal. However, the dependency on the rate of frequency variation is not clearly identified in the SSC parameter. Simulations have shown that, for large chirp bandwidths, the rate of frequency variation is also important with the receiver being more robust to large repetition periods of the chirp interference.

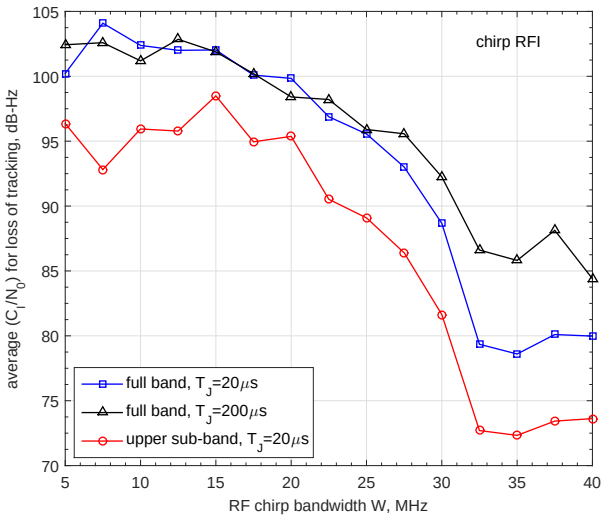

Figure 6.19: Average (C_I/N_0) for the loss of tracking with full band and upper sub-band processing for chirp interference

Chapter 7

Final Remarks

This chapter presents in section 1 the final conclusions regarding this document and proposes the future work recommendations in section 2.

7.1 Conclusions

AltBOC is the most sophisticated of all the signals broadcast by the current GNSSs. It conveys four components and can be treated as a wideband single signal or as two independent narrowband signals. Therefore multiple solutions for the receiver architecture are possible, and the receiver implementation is still today a challenging task.

The implementation of this thesis corresponded to a period of intense learning of the technical aspects by the candidate, concerning the AltBOC modulation. With this thesis the candidate had several objectives in mind: (i) gain insight into the nature of the AltBOC modulation, (ii) analyze the different aspects in the implementation of AltBOC receivers, (iii) implement and test distinct receiver architectures, namely Single Sideband and Double Sideband processing, and compare their results. From the resulting work, the final remarks are summarized:

- Given the differences of the AltBOC modulation relative to other less sophisticated modulations, like BPSK, an extensive theoretical study regarding the DSB and SSB E5 AltBOC signal receiver architectures was presented;
- A functional receiver was implemented for both SSB and DSB processing;
- The DSB processing presents better results in terms of average positioning error for all C/N_0;
- Several receiver parameters were discussed and optimized. Namely the Early-Late spacing and time of integration were tested and results were shown.
- It was concluded that higher values of time of integration result in better results of robustness to noise for lower C/N_0;

- For the E-L spacing the value of 0.2 T_{C} presents better results both for the average error and robustness than 0.1 T_{C}. Higher values of E-L spacing are not advised since the linear region of the NELP discriminator response is reduced which could increase the probability of false-lock synchronization;
- Interference tests were proposed and simulation results were presented in chapter 6. A conference paper was produced and accepted for presentation with the results obtained in this topic [38];
- A simulation paralelization procedure was developed where the tested variable was chosen randomly in an uniformly distributed interval. The results were grouped in a pre-defined number of sub-intervals and averaged. This procedure permitted to accelerate the simulation process by resorting to multiple computers.

7.2 Future work

Although falling outside the scope of the present work, the following points are interesting topics to reveal the potentialities of the AltBOC receiver architectures:

- Test the algorithms with real satellite data;
- Compare the Dual Sideband and Single Sideband results with the BPSK-R(10) approach;
- Test the AltBOC receiver architectures in multipath scenarios;
- Analyze the effects and test the implemented receivers using a finite number of quantization levels;
- Implement the acquisition algorithm which due to its complexity, was not addressed in this work.

Bibliography

[1] J. Ávila Rodríguez. *On Generalized Signal Waveforms for Satellite Navigation*. PhD thesis, Universitat der Bundeswehr, Munich, June 2008.

[2] L. Lestarquit, G. Artaud, and J.-L. Issler. AltBOC for dummies or everything you always wanted to know about AltBOC. In *Proceedings of ION 2008 GNSS*, pages 961–970, September 2008.

[3] M. Soellner. Comparison of awgn code tracking accuracy for alternative-BOC, complex-LOC and complex-BOC modulation options in Galileo E5-band. In *Proceedings of the European Navigation Conference ENC-GNSS 2003*, April 2003.

[4] N. Gerein. Hardware architecture for processing Galileo alternate binary offset carrier (AltBOC) signals. patent US2005/0012664 A1, January 2005.

[5] W. D. Wilde, J.-M. Sleewaegen, and G. Seco-Granados. A method and device for demodulating Galileo alternate binary offset carrier (AltBOC) signals. patent 2006027004 A1, March 2006.

[6] J.-M. Sleewaegen, W. D. Wilde, and M. Hollreiser. Galileo AltBOC receiver. In *Proceedings of European Navigation Conference 2004*, pages 1–9, May 2004.

[7] G. X. Gao et al. Ionosphere effects for wideband GNSS signals. In *Proceedings of ION Annual Meeting 2007*, pages 147–155, April 2007.

[8] D. Margaria. *Galileo AltBOC Receivers*. PhD thesis, Politecnico di Torino, Italy, July 2007.

[9] D. Margaria et al. An innovative data demodulation technique for Galileo AltBOC receivers. *Journal of Global Positioning Systems*, 6(1):89–96, 2007.

[10] N. C. Shivaramaiah. *Enhanced Receiver Techniques for Galileo E5 AltBOC Signal Processing*. PhD thesis, University of South Wales, Sydney, Australia, June 2011.

[11] I. Colomina et al. The accuracy potential of Galileo E5/E1 pseudoranges for surveying and mapping. In *Proceedings of ION GNSS 2011*, pages 2332–2340, September 2011.

[12] H. Tokura et al. The possibility of precise automobile navigation using GPS/QZSS L5 and Galileo E5 pseudoranges. In *Proceedings of ION ITM 2013*, pages 194–202, January 2013.

[13] European GNSS (Galileo) Open Service. *Signal In Space Interface Control Document*, 2015.

[14] P. Misra and P. Enge. *Global Positioning System: Signals, Measurements and Performance*. Ganga-Jamuna Press, 2006.

[15] How technology work. How technology work: How does a gps work. http://www.howtechnologywork.com/how-does-a-gps-work/, accessed on June 6, 2016.

[16] US government. Official u.s. government information about the global positioning system (GPS) and related topics. http://www.gps.gov, accessed on February 3, 2016.

[17] ESA. Galileo navigation system. http://www.esa.int/Our_Activities/Navigation/The_future_-_galileo/What_is_galileo, accessed on January 28, 2016.

[18] China Satellite Office. Beidou navigation satellite system. http://en.beidou.gov.cn/, accessed on March 15, 2016.

[19] Rohde-Schwarz. Receiving Beidou, Galileo and GPS signals with matlab and r&s iqr, r&s tsmw. https://cdn.rohde-schwarz.com/pws/dl_downloads/dl_application/application_notes/1ma203/1MA203_0e_beidouSWReceiver.pdf, accessed on December 16, 2015.

[20] J. . Ávila Rodríguez et al. The MBOC modulation. *Inside GNSS*, 2(6):43–58, September 2007.

[21] J. S. Subirana, J. M. Zornoza, and M. Hern. *"GNSS Data Processing: Fundamentals and Algorithms", volume I*. European Space Agency, 2013.

[22] R. S. Conker, M. B. El-Arini, C. J. Hegarty, and T. Hsiao. Modeling the effects of ionospheric scintillation on GPS/satellite-based augmentation system availability. *Radio Science*, 38(1):1–23, 2003.

[23] F. Dovis, editor. *GNSS Interference Threats and Countermeasures*. Artech House, 2015.

[24] J. W. Betz. *Engineering Satellite-Based Navigation and Timing: Global Navigation Satellite Systems, Signals, and Receivers*. Wiley, 2016.

[25] GMV. Navipedia: Generic GPS receiver. http://www.navipedia.net/index.php/Main_Page, accessed on February 18, 2016.

[26] F. M. G. Sousa and F. D. Nunes. New expressions for the autocorrelation function of BOC GNSS signals. *NAVIGATION, Journal of The Institute of Navigation*, 60(1):1–9, Spring 2013.

[27] R. G. Brown and P. Y. C. Hwang. *Introduction to Random Signals and Applied Kalman Filtering*. Wiley, 1997.

[28] F. van Diggelen. *A-GPS: Assisted GPS, GNSS, and SBAS*. Artech House, 2009.

[29] A. Gelb, editor. *Applied Optimal Estimation*. M.I.T. Press, 1974.

[30] J. Tsui. *Fundamentals of Global Positioning System Receivers*. John Wiley and Sons, 2005.

[31] K. Borre et al. *A Software-Defined GPS and Galileo Receiver*. Birkauser, 2007.

[32] E. D. Kaplan and C. J. Hegarty. *Understanding GPS: Principles and Applications*. Artech House, 2006.

[33] P. Fine and W. Wilson. Tracking algorithm for GPS offset carrier signals. In *Proceedings of ION 1999 National Technical Meeting*, pages 671–676, January 1999.

[34] J. W. Betz and K. R. Kolodziejski. Generalized theory of code tracking with an early-late discriminator, part ii: Noncoherent processing and numerical results. *IEEE Transactions on Aerospace and Electronic Systems*, 45(4):1551–1564, October 2009.

[35] N. Shivaramaiah, A. G. Dempster, and C. Rizos. Hybrid tracking loop architectures for the Galileo E5 signal. In *European Navigation Conference ENC-GNSS*, 2009.

[36] J. Proakis. *Digital Communications*. McGraw-Hill, 1989.

[37] M. C. Jeruchim, P. Balaban, and K. S. Shanmugan, editors. *Simulation of Communication Systems. Modeling, Methodology and Techniques*. Kluwer, 2000.

[38] F. D. Nunes, R. F. D. Nunes, and F. M. G. Sousa. Performance evaluation in AltBOC receivers affected by interference. In *Proceedings of ICL-GNSS2016*, pages 1–6, June 2016.

[39] J. Klauder, A. Price, S. Darlington, and W. Albersheim. The theory and design of chirp radars. *The Bell System Technical Journal*, 34(4):745–808, July 1960.

[40] I. V. Oppenheim and R. W. Schafer, editors. *Digital Signal Processing*. Prentice-Hall, 1975.

Appendix A

Autocorrelation functions of GNSS signals

This appendix contains the expressions of the autocorrelation functions for the BPSK, BOCs and CBOC signals and is based on [26].

Consider a generic pulse amplitude modulation signal

$$x(t) = \sum_k c_k g(t - kT_c) \tag{A.1}$$

where c_k, $k = \ldots, -1, 0, 1, \ldots$ is a set of independent real or complex random variables, with $E\{c_k\} = 0$, $E\{|c_k|^2\} = P$, $E\{c_k c_m^*\} =$, $m \neq k$, and $g(t)$ is a signaling pulse defined in the interval $0 \leq t \leq T_c$ (T_c is the chip duration). It can be shown that the autocorrelation function of $x(t)$ is given by

$$R_x(\tau) = \frac{P}{T_c} \int_{|\tau|}^{T_c} g(t) g^*(t - |\tau|)\, dt, \quad |\tau| < T_c \tag{A.2}$$

Let the triangle function with support $2L$ be defined as

$$\Lambda_L(t) = \begin{cases} 1 - \frac{|t|}{L}, & |t| > L \\ 0, & \text{otherwise} \end{cases} \tag{A.3}$$

and let $T_{\mathrm{C/A}} \equiv 10^{-3}/1023$ s denote the chip duration of the GPS C/A code.

- **Binary phase shifted keyed signals: BPSK-R(n)**

For binary phase shifted keyed signals ($c_k = \pm 1$) the pulse $g(t)$ is rectangular, with $g(t) = 1$ for $0 \leq t \leq T_c$, with chip duration $T_c = T_{\mathrm{C/A}}/n$ s, $p = 1, 2, \ldots$ The autocorrelation function of the signal BPSK-R(p) is given by

$$R_{\mathrm{BPSK(p)}}(\tau) = \Lambda_{T_c}(\tau) \tag{A.4}$$

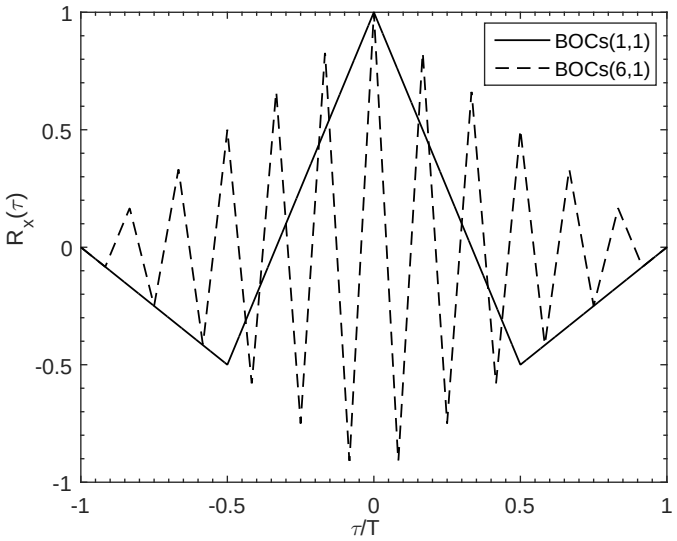

Figure A.1: Autocorrelation functions for BOCs(1,1) and BOCs(6,1)

• **Sine-phased binary offset carrier signals: BOCs(pn,n)**

The sine-shaped signaling pulse is defined by $g(t) = \text{sign}\{\sin(2\pi f_s t)\}$, for $0 \leq t \leq T_c$ and zero otherwise, with $f_s T_c = p$ and $T_c = T_{\text{C/A}}/n$. The autocorrelation function of the signal BOCs(pn,n), with k and n integer, is given by

$$R_{\text{BOCs(pn,n)}}(\tau) = \Lambda_{T_c/(2p)}(\tau) + \sum_{k=1}^{2p-1} (-1)^k \left(1 - \frac{k}{2p}\right) \Lambda_{T_c/(2p)}\left(|\tau| - \frac{kT_c}{2p}\right) \tag{A.5}$$

Figure A.1 exhibits the autocorrelation functions for BOCs(1,1) and BOCs(6,1).

• **Composite BOC signals: CBOC(6,1,1/11)**

For composite binary offset carrier signals (data or pilot) the signaling pulse $g(t)$ is

$$g(t) = a_1 g_1(t) + a_2 g_2(t) \tag{A.6}$$

with $a_1 = \sqrt{10/11}$ and $a_2 = \pm\sqrt{1/11}$ (the minus sign stands for the pilot signal and the plus sign for the data signal). Pulses $g_1(t)$ and $g_2(t)$ are defined by

$$g_1(t) = \begin{cases} \text{sign}(\sin(2\pi \text{t}/\text{T}_\text{c})), & 0 \leq t \leq T_c \\ 0, \text{otherwise} \end{cases} \tag{A.7}$$

with $T_c = T_{\text{C/A}}$ and

$$g_2(t) = \begin{cases} \text{sign}(\sin(12\pi \text{t}/\text{T}_\text{c})), & 0 \leq t \leq T_c \\ 0, \text{otherwise} \end{cases} \tag{A.8}$$

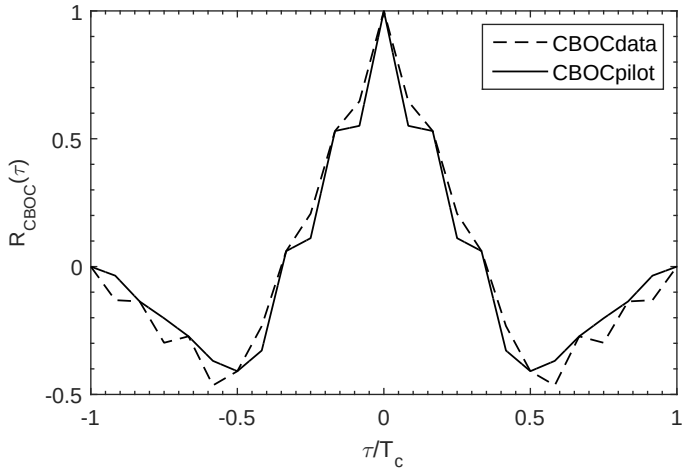

Figure A.2: Autocorrelation functions for CBOCdata and CBOCpilot

The autocorrelation functions of the signals CBOCdata and CBOCpilot are given by

$$R_{\mathrm{CBOC}}(\tau) = \frac{10}{11} R_{\mathrm{BOCs}(1,1)}(\tau) + \frac{1}{11} R_{\mathrm{BOCs}(6,1)}(\tau) \pm 2\frac{\sqrt{10}}{11} I_{1,2}(\tau) \tag{A.9}$$

where the plus sign stands for the data signal and the minus sign for the pilot signal. The cross-correlation term is defined as

$$I_{1,2}(\tau) = \frac{1}{12} \sum_{i=1}^{3} \Lambda_{T_c/12}\left(|\tau| - \frac{(2i-1)T_c}{12}\right) - \Lambda_{T_c/12}\left(|\tau| - \frac{(2i+5)T_c}{12}\right) \tag{A.10}$$

Figure A.2 displays the autocorrelation functions for CBOCdata and CBOCpilot. Note that the main peak of CBOCpilot autocorrelation is sharper allowing to produce better code tracking results than the CBOCdata.

Appendix B

Series expansion of the AltBOC(15,10) subcarriers

The complex Fourier series for subcarrier $sc_{E5-S}(t)$ is

$$sc_{E5-S}(t) = \sum_{n=-\infty}^{\infty} c_n \exp(j2\pi n f_s t) \tag{B.1}$$

where the Fourier coefficients are given by

$$c_n = \frac{1}{T_s} \int_0^{T_s} sc_{E5-S}(t) \cos(2\pi n f_s t)\, dt \tag{B.2}$$

with $f_s = 1/T_s$. Thus

$$c_n = \begin{cases} 0, & n = 0 \\ \frac{1}{2}\operatorname{sinc}\left(\frac{n}{2}\right)\left(1 + \sqrt{2}\cos\left(\frac{\pi n}{4}\right)\right), & n \neq 0 \end{cases} \tag{B.3}$$

The Fourier coefficients with positive index are given by

$$\begin{aligned} c_1 &= \frac{2}{\pi} \approx 0.6366 \\ c_2 &= c_3 = c_4 = c_5 = c_6 = 0 \\ c_7 &= -\frac{2}{7\pi} \approx -0.0909 \end{aligned} \tag{B.4}$$

Thus, the subcarrier is approximately sinusoidal with

$$sc_{E5-S}(t) = c_1[\exp(-j2\pi f_s t) + \exp(j2\pi f_s t)] = \frac{4}{\pi}\cos(2\pi f_s t) \tag{B.5}$$

provided that we apply ideal lowpass filtering with cutoff frequency smaller than $7f_s = 107.415$ MHz.

The complex Fourier expansion of subcarrier $sc_{E5-P}(t)$ is

$$sc_{E5-P}(t) = \sum_{n=-\infty}^{\infty} c'_n \exp(j2\pi n f_s t) \tag{B.6}$$

where the Fourier coefficients are given by

$$c'_n = \begin{cases} 0, & n = 0 \\ \frac{1}{2}\operatorname{sinc}\left(\frac{n}{2}\right)\left(1 - \sqrt{2}\cos\left(\frac{\pi n}{4}\right)\right), & n \neq 0 \end{cases} \tag{B.7}$$

Thus, we have

$$\begin{aligned} c'_1 = c'_2 = c'_4 = c'_5 = c'_6 = c'_7 = 0 \\ c'_3 = \operatorname{sinc}\left(\frac{3}{2}\right) = -\frac{2}{3\pi} \approx -0.2122 \end{aligned} \tag{B.8}$$

Therefore, using ideal lowpass filtering in the signal $sc_{E5-P}(t)$ with cutoff frequency smaller than $3f_s = 46.035$ MHz, permits to eliminate completely the subcarrier.

Appendix C

Sampling Frequency Analysis

In the presence of AWGN with power spectral density $N_0/2$ the received AltBOC signal at the output of the bandpass filter with bandwidth B is given by

$$r(t) = A\left[\mathrm{Re}\{S_{E5}(t)\}\cos(\omega_0 t+\phi) - \mathrm{Im}\{S_{E5}(t)\}\sin(\omega_0 t+\phi)\right] + n_i(t)\cos(\omega_0 t) - n_q(t)\sin(\omega_0 t) \quad \text{(C.1)}$$

where A is the amplitude and ω_0 includes the carrier frequency and Doppler frequency shift and $n_i(t)$ and $n_q(t)$ are, respectively, the inphase/quadrature components of the Gaussian noise. The power of the received AltBOC signal is

$$P_s = \frac{A^2}{2}\left[< \mathrm{Re}^2\{S_{E5}(t)\} > + < \mathrm{Im}^2\{S_{E5}(t)\} >\right] \quad \text{(C.2)}$$

with $< \cdot >$ denoting the time average operator. Taking into account equation (18), chapter V

$$P_s = \frac{A^2}{2\pi^2}\left[< \alpha^2(t) > + < \beta^2(t) > + < \gamma^2(t) > + < \mu^2(t) >\right] \quad \text{(C.3)}$$

where $< \cdot >$ denotes the time average operator. Now, using equations (6)-(9) of chapter V, we have $< \alpha^2(t) >=< \beta^2(t) >=< \gamma^2(t) >=< \mu^2(t) >= 2$, yielding $P_s = 4A^2/\pi^2$.

The received signal is characterized by the carrier-to-noise power spectral density ratio

$$\left(\frac{C}{N_0}\right) = \frac{P_s}{N_0} = \frac{4A^2}{\pi^2 N_0} \quad \text{(C.4)}$$

The baseband components of $r(t)$ are

$$r_i(t) = A\,\mathrm{Re}\{S_{E5}(t)\}\cos\phi - A\,\mathrm{Im}\{S_{E5}(t)\}\sin\phi + n_i(t) \quad \text{(C.5)}$$

$$r_q(t) = A\,\mathrm{Im}\{S_{E5}(t)\}\cos\phi + A\,\mathrm{Re}\{S_{E5}(t)\}\sin\phi + n_q(t) \quad \text{(C.6)}$$

with $n_i(t)$ and $n_q(t)$ being independent zero-mean Gaussian lowpass processes with bandwidth $B/2$

and equal power spectral densities given by

$$G_i(f) = G_q(f) = N_0 \Pi\left(\frac{f}{B}\right) \tag{C.7}$$

The corresponding autocorrelation functions are

$$R_{ni}(\tau) = R_{nq}(\tau) = N_0 B \,\mathrm{sinc}\,(B\tau) \tag{C.8}$$

Sampling the baseband signals in Monte Carlo simulation requires a rate $f_s = \Delta_s^{-1}$ such that $f_s > B$, according to the sampling theorem. The signals $r_i(t)$ and $r_q(t)$ are sampled at time $t = t_k$ to yield

$$r_i(t_k) = A\,\mathrm{Re}\{S_{E5}(t_k)\}\cos\phi - A\,\mathrm{Im}\{S_{E5}(t_k)\}\sin\phi + n_i(t_k) \tag{C.9}$$

$$r_q(t_k) = A\,\mathrm{Im}\{S_{E5}(t_k)\}\cos\phi + A\,\mathrm{Re}\{S_{E5}(t_k)\}\sin\phi + n_q(t_k) \tag{C.10}$$

with $\mathrm{Re}\{S_{E5}(t_k)\}$ and $\mathrm{Im}\{S_{E5}(t_k)\}$ given by (5.18).

Two Gaussian noise samples $n_i(t_k)$ and $n_i(t_{k+1})$, with $t_{k+1} - t_k = \Delta_s$, are independent if they are uncorrelated; that is, when

$$E\{n_i(t_k)n_i(t_{k+1})\} = R_{ni}(\Delta_s) = 0 \tag{C.11}$$

This corresponds to $\mathrm{sinc}(B\Delta_s) = 0$, or $f_s = B/n$, with $n = 1, 2, \ldots$. This result shows that, in Monte Carlo simulation, making the noise samples independent is equivalent to assume that the receiver's front-end bandwidth B is equal to the sampling rate (or to multiples of f_s). Put in another way: given a certain bandwidth B, the sampling rate cannot exceed that frequency ($f_s \leq B$) to guarantee that the noise samples are independent.

The variance of the noise samples is $\sigma_N^2 = R_{ni}(0) = N_0 B$. Considering that the noise samples are independent and $f_s = B$ we obtain $\sigma_N^2 = N_0/\Delta_s$. Using now (C.4) leads to

$$A = \sqrt{2N_0\left(\frac{C}{N_0}\right)} = \frac{\pi}{2}\sqrt{\Delta_s \sigma_N^2\left(\frac{C}{N_0}\right)} \tag{C.12}$$

In terms of efficient Monte Carlo simulation it is appropriate to consider $\sigma_N^2 = 1$ and make $A = (\pi/2)\sqrt{\Delta_s(C/N_0)}$.

Appendix D

Second-Order PLL

Consider the second-order PLL with arctangent discriminator. The linearized model of the PLL is shown in Fig. D.1 with $N_{QP}(k-1)$ denoting a noise component.

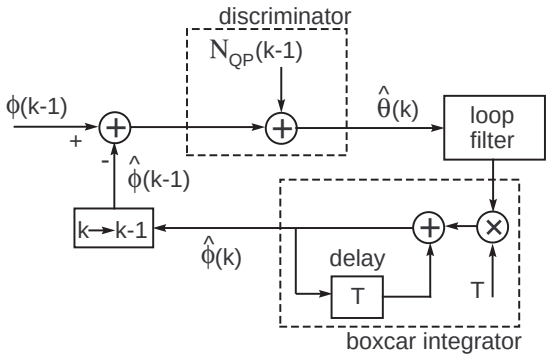

Figure D.1: Linearized model of the PLL

The transfer function of the PLL in the discrete-z domain is given by [30]

$$H(z) = \frac{F(z)N(z)z^{-1}}{1 + F(z)N(z)z^{-1}} = \frac{TF(z)z^{-1}}{1 + (TF(z) - 1)z^{-1}} \tag{D.1}$$

where T is the sampling interval and $F(z)$ and $N(z)$ are, respectively, the transfer functions of the loop filter and the boxcar integrator, which is

$$N(z) = \frac{T}{1 - z^{-1}} \tag{D.2}$$

Consider the second-order loop filter described in Fig. D.2.

The filter response in the time domain is

$$\begin{aligned} y(k) &= aT \sum_{i=1}^{k-1} x(i) + (aT/2 + b)x(k) \\ &= y(k-1) + \left(\frac{aT}{2} - b\right) x(k-1) + \left(\frac{aT}{2} + b\right) x(k) \end{aligned} \tag{D.3}$$

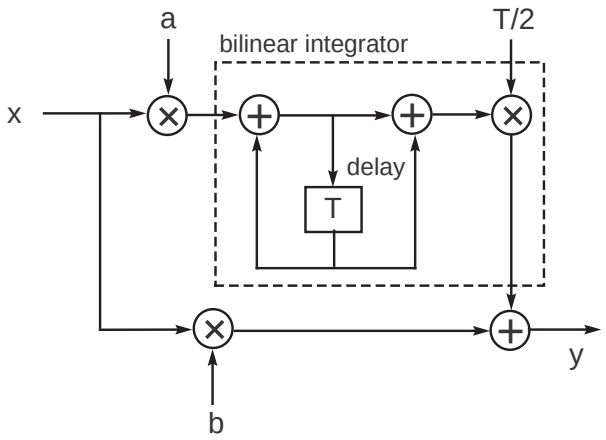

Figure D.2: Second-order loop filter

The difference equation relating input and output is of the form

$$y(k) = \sum_{i=1}^{N} a_i y(k-i) + \sum_{i=0}^{M} b_i x(k-i) \tag{D.4}$$

with $M = N = 1$ and

$$a_1 = 1, \quad b_0 = \frac{aT}{2} + b, \quad b_1 = \frac{aT}{2} - b \tag{D.5}$$

The transfer function is given by [40]

$$F(z) = \frac{Y(z)}{X(z)} = \frac{\sum_{i=0}^{M} b_i z^{-i}}{1 - \sum_{i=1}^{N} a_i z^{-i}} \tag{D.6}$$

leading to

$$F(z) = \frac{b_0 + b_1 z^{-1}}{1 - z^{-1}} \tag{D.7}$$

The transfer function of the closed loop is

$$H(z) = \frac{c_1 z^{-1} + c_2 z^{-2}}{1 + c_3 z^{-1} + c_4 z^{-2}} \tag{D.8}$$

where the constants are given by

$$c_1 = \left(\frac{aT}{2} + b\right) T \tag{D.9}$$

$$c_2 = \left(\frac{aT}{2} - b\right) T \tag{D.10}$$

$$c_3 = c_1 - 2 \tag{D.11}$$

$$c_4 = c_2 + 1 \tag{D.12}$$

The noise equivalent bandwidth in Hz is

$$B_n = \frac{1}{2\pi T}\int_0^{\pi} |H(e^{j\omega})|^2\, d\omega \tag{D.13}$$

with

$$|H(e^{j\omega})|^2 = \frac{(c_1^2 + c_2^2) + 2c_1c_2\cos(\omega)}{(1 + c_3^2 + c_4^2) + 2c_3(1 + c_4)\cos(\omega) + 2c_4\cos(2\omega)}, \quad |H(0)|^2 = 1 \tag{D.14}$$

The discussion of the closed loops is usually based on continuous systems [30], [32]. The transfer from the continuous s-domain to the discrete z-domain is made through the bilinear transform

$$s = \frac{2}{T}\frac{1 - z^{-1}}{1 + z^{-1}} \tag{D.15}$$

or equivalently

$$z^{-1} = \frac{1 - sT/2}{1 + sT/2} \tag{D.16}$$

This result can be replaced in (D.8) to obtain

$$H(s) = \frac{\nu^2(c_2 - c_1) - 2\nu c_2 + (c_1 + c_2)}{\nu^2(1 - c_3 + c_4) + 2\nu(1 - c_4) + (1 + c_3 + c_4)} \tag{D.17}$$

with $\nu \equiv sT/2$, or

$$H(s) = \frac{c_2 - c_1}{1 - c_3 + c_4}\frac{s^2 - \frac{4c_2}{(c_2 - c_1)T}s + \frac{4}{T^2}\frac{c_1 + c_2}{c_2 - c_1}}{s^2 + \frac{4(1 - c_4)}{T(1 - c_3 + c_4)}s + \frac{4}{T^2}\frac{1 + c_3 + c_4}{1 - c_3 + c_4}} \tag{D.18}$$

The denominator of the second fraction may be written as $s^2 + 2\xi\omega_n s + \omega_n^2$, where ω_n is the natural frequency and ξ is the damping factor with

$$\omega_n = \frac{2}{T}\sqrt{\frac{c_1 + c_2}{c_2 - c_1 + 4}} = \sqrt{\frac{a}{1 - bT/2}} \tag{D.19}$$

and

$$\xi = \frac{-c_2}{\sqrt{(c_1 + c_2)(4 + c_2 - c_1)}} \tag{D.20}$$

Given parameters ω_n and ξ, it is easy to determine approximately the loop noise bandwidth according to [30]

$$B_n = \frac{\omega_n}{2}\left(\xi + \frac{1}{4\xi}\right) \tag{D.21}$$

In general, this result is a tight approximation to the exact value computed using (D.13).